

Laser-driven sources of electrons and x-rays in underdense plasma: Theory and simulation

by Petr Valenta

Dissertation submitted to the
Faculty of Nuclear Sciences and Physical Engineering,
Czech Technical University in Prague,
in partial fulfillment of the requirements for the degree of
Doctor of Philosophy.

Prague, 2022

supervisor:

doc. Ing. Ondřej Klímo, Ph.D.
Department of Physical Electronics,
Faculty of Nuclear Sciences and Physical Engineering,
Czech Technical University in Prague,
Trojanova 13, 120 00 Praha,
Czech Republic

supervisor specialist:

Prof. Sergei Vladimirovich Bulanov
ELI Beamlines Centre,
Institute of Physics,
Czech Academy of Sciences,
Za Radnicí 835, 252 41 Dolní Břežany,
Czech Republic

Abstract

Keywords: laser-plasma interaction, laser-wakefield acceleration, relativistic mirrors, particle-in-cell simulation

Contents

Abstract	3
1 Introduction	7
1.1 Methods and state-of-the-art	7
1.2 Aims and motivation	8
1.3 Author's role and contributions	10
1.4 Outline of the thesis	12
2 Theoretical background	15
2.1 Interaction of laser and underdense plasma	15
2.1.1 Basic laser and plasma parameters	15
2.1.2 Finite-amplitude Langmuir waves	16
2.1.3 Breaking of Langmuir waves	19
2.2 Laser-wakefield acceleration of electrons	21
2.2.1 Electron interaction with Langmuir wave	21
2.2.2 Limits of acceleration	22
2.3 Relativistic mirrors in underdense plasmas	22
2.3.1 Relativistic flying flat mirror	23
2.3.2 Relativistic flying parabolic mirror	25
2.3.3 Reflection coefficient	27
2.3.4 Recoil effects	29
2.4 Particle-in-cell method	31
2.4.1 General description	31
2.4.2 Particle pusher	33
2.4.3 Field solver	34
2.4.4 Field and particle weighting	36
3 Author's original results	39
3.1 On the electromagnetic-electron rings	39
3.2 On the laser-wakefield polarity reversal	41
3.3 On the recoil effects of relativistic mirrors	42
3.4 On the relativistic flying forcibly oscillating mirror	43
4 Conclusion	45
4.1 Summary	45
4.2 Future research and perspectives	45
Acknowledgements	47

Bibliography	48
Appendices	65
A List of author's publications	65
A.1 Publications in peer-reviewed journals	65
A.2 Publications in conference proceedings	66
A.3 Book chapters	67
B Selected publications	69
B.1 On the electromagnetic-electron rings originating from the interaction of high-power short-pulse laser and underdense plasma	71
B.2 Polarity reversal of wakefields driven by ultrashort pulse laser	83
B.3 Recoil effects on reflection from relativistic mirrors in laser plasmas	91
B.4 Relativistic flying forcibly oscillating reflective diffraction grating	101

“Everything should be made as simple as possible, but no simpler.”

– Albert Einstein (1879 – 1955)



Introduction

In this chapter, we first introduce the reader with a very coarse review of historical milestones and some of the most important achievements of laser – our main instrument. Then, we define the objectives of our research and put them in the context of current worldwide efforts in the corresponding fields. Also, we specify what exactly has been accomplished by the author and how it advances the scientific knowledge. Finally, we outline how the structure of this doctoral thesis is organized.

1.1 Methods and state-of-the-art

The operation of the world’s first working laser was demonstrated in 1960 [Maiman, 1960]. Soon after, the introductions of Q-switching [McClung and Hellwarth, 1962] and mode-locking [Mocker and Collins, 1965] have enabled generation of laser pulses with GW peak powers and sub-ps durations. At the same time, most of the major effects in nonlinear optics were discovered or experimentally verified (e.g., generation of optical harmonics [Franken et al., 1961], optical rectification [Bass et al., 1962], optical Kerr effect [Armstrong et al., 1962; Maker et al., 1964], stimulated Raman scattering [Woodbury and Ng, 1962], stimulated Brillouin scattering [Chiao et al., 1964a; Chiao et al., 1964b], multiphoton absorption and ionization [Kaiser and Garrett, 1961; Voronov and Delone, 1966]).

Further amplification of laser pulses had been limited for relatively long time due to the development of nonlinear effects causing a detrimental pulse distortions or even a damage to the gain medium and optical components. This obstacle was overcome by applying the method of chirped pulse amplification [Strickland and Mourou, 1985; Maine and Mourou, 1988] to optical amplifiers. To avoid the nonlinear effects, the laser pulse is stretched out temporally by several orders of magnitude (the input pulse energy is unchanged, but the intensity is lowered to an acceptable level) before passing through the amplifier medium (there are usually several amplifier stages) and then compressed by the same ratio back to a duration similar to its initial value.

A rapid progress in laser technology over several past decades has stimulated the development of high-power lasers all over the world. By the end of the 20th century, the laser pulses exceeded the PW power threshold [Perry et al., 1999]. Currently, the highest laser

pulse peak power achieved is 10 PW [Tanaka et al., 2020]. Global efforts towards making the lasers even more powerful are continuing; historical perspective, current status, and future plans to attain the 100 PW level are summarized, e.g., in Refs. Danson et al., 2019 and Li et al., 2021.

Rather than power, however, it is often desired to reach the highest laser intensity (i.e., the power per unit area). The peak laser intensities can be increased either by further amplifying the laser beam energy or by reducing the size of the focal spot. While the former approach comes at great cost since it requires a higher level of complexity for the laser chain, the latter seems to be more effective due to the quadratic dependency of the laser intensity on the inverse of the focal spot radius. Therefore, a number of sophisticated focusing schemes have been under active investigation (e.g., multiple beam focusing [Bulanov et al., 2010], tight-focusing [Bahk et al., 2004; Jeong et al., 2015], 4π -spherical focusing [Gonoskov et al., 2012; Jeong et al., 2020]). Recent experimental implementations of the tight-focusing scheme have demonstrated an intensity approaching 10^{22} W/cm² by focusing a 45 TW laser into a spot of size $0.8 \mu\text{m}$ [Bahk et al., 2004], and a record intensity over 10^{23} W/cm² by focusing a 4 PW laser into a spot of size $1.1 \mu\text{m}$ [Yoon et al., 2021]. In this context, producing, manipulating, and controlling intense laser pulses present major difficulty for the conventional solid-state optics, encouraging the development of their plasma-based counterparts [Thaury et al., 2007; Nakatsutsumi et al., 2010; Tamburini et al., 2014; Peng et al., 2019].

Another very active research direction is to make the high-power laser pulses as short as possible. In the systems based on the chirped pulse amplification, the output pulse durations are inherently limited by the gain bandwidths of the amplifying media (e.g., the bandwidth of titanium-doped sapphire spans over ≈ 75 nm, the obtainable bandwidth is further reduced by gain narrowing associated with amplification over several orders of magnitude [Hotz, 1965], and thus restricting the pulse durations to ≈ 35 fs). Currently, there are two methods capable of tackling this issue: the optical parametric chirped pulse amplification [Dubietis et al., 1992], which extends the chirped pulse amplification technique by using the optical parametric amplifiers (i.e., amplifiers based on parametric nonlinear interactions [Giordmaine and Miller, 1965; Baumgartner and Byer, 1979]), and the post-compression of laser pulses via self-phase modulation in hollow-core fibers [Nisoli et al., 1996]. The former method has recently demonstrated the generation of 5 PW, 18.6 fs [Zeng et al., 2017] or 16 TW, 4.5 fs [Rivas et al., 2017] laser pulses, the latter one sub-4 fs pulses (corresponding to almost a single optical cycle) with a peak power exceeding 1 TW [Ouillé et al., 2020; Nagy et al., 2020].

Ultimately, in order to use the high peak power lasers for competitive real-world applications (some of them are discussed in Sec. 1.2), they essentially need to operate continuously with high efficiencies and deliver pulses with high average powers and repetition rates. In this context, the traditional flash lamps pumping the initial energy into lasers are being progressively replaced by laser diodes [Byer, 1988], which dramatically improve the wall-plug efficiency of the laser, stability, output beam quality, and lowers the requirements for cooling system. At the state-of-the-art, TW- and PW-class laser systems, respectively, are able to operate at 1 kHz [Budriūnas et al., 2017; Toth et al., 2020] and 10 Hz [Haefner et al., 2017; Osvay et al., 2019] repetition rates.

1.2 Aims and motivation

The research fields where the high-power lasers play a significant role can be divided into four main directions: (i) acceleration of charged particles, (ii) generation of radiation sources, (iii)

nuclear fusion, and (iv) investigation of yet unexplored physical processes (e.g., related to quantum electrodynamics, high-energy density physics, or laboratory astrophysics). Within the scope of this doctoral thesis, we have selected two research topics to be studied: the acceleration of electrons via the laser-wakefield mechanism and the generation of short-wavelength radiation based on the concept of relativistic flying mirrors. The investigated research topics are tightly connected to each other in the sense that they both strongly rely on the controlled laser-driven excitation of high-amplitude Langmuir waves in underdense plasmas.

The laser-wakefield acceleration, which was proposed in 1979 [Tajima and Dawson, 1979], is already a well-established technique for producing high-energy electron beams in a plasma medium. Within this concept, a relativistically intense laser pulse propagating in underdense plasma induces a strong longitudinal electric field which, in turn, accelerates duly injected electrons [Esarey et al., 1996; Esarey et al., 2009; Hooker, 2013; Bulanov et al., 2016a]. One of the primary advantages of this concept lies in the fact that ionized plasmas can sustain electric fields several orders of magnitude larger than conventional radio-frequency accelerators [Dawson, 1959], allowing one to substantially reduce the acceleration length (e.g., to generate the electron beam with the energy up to 10 GeV, the acceleration length of only 20 cm is required, whereas it would take about 500 m with a conventional accelerator).

Over the last few decades, the quality of accelerated electron beams has rapidly evolved mainly due to the advances in technology and better understanding of the underlying physical processes. First high-quality quasi-monoenergetic electron beams were produced in 2004 [Faure et al., 2004; Geddes et al., 2004; Mangles et al., 2004] operating the laser-wakefield acceleration experiments in the blowout (or bubble) regime [Pukhov and Meyer-ter Vehn, 2002; Lu et al., 2006; Lu et al., 2007], in which the wakefield takes the form of an ion cavity surrounded by thin electron walls. Today, the laser-wakefield acceleration has demonstrated (although not simultaneously) the capability of producing electron beams in the multi-GeV energy range with a relative energy spread of a few percent [Kim et al., 2013; Leemans et al., 2014; Gonsalves et al., 2019], a few fs duration [Van Tilborg et al., 2006; Ohkubo et al., 2007; Debus et al., 2010; Lundh et al., 2011], and hundreds of pC of charge [Couperus et al., 2017]. These achievements make the concept of laser-wakefield acceleration increasingly attractive for a wide range of multi-disciplinary experiments and applications (e.g. radiography [Glinec et al., 2005], radiotherapy [Malka et al., 2010; DesRosiers et al., 2000], radiolysis [Malka et al., 2010; Gauduel et al., 2010]).

The relativistic flying mirrors are objects that reflect incoming radiation while moving at relativistic velocity [Einstein, 1905]. An electromagnetic wave incident on a relativistic mirror undergoes energy and frequency changes due to the double Doppler effect. In a co-propagating configuration, the reflected wave is stretched, its amplitude is lowered, and its frequency is downshifted. In contrast, in a counter-propagating configuration, the reflected wave is compressed, amplified, and its frequency is upshifted. Relativistic mirrors can be physically realized, e.g., by irradiating plasma targets with intense laser pulses (see Ref. Bulanov et al., 2013 for a review and the literature cited therein). They appear in laser plasmas as thin dense electron (or electron-ion) shells accelerated to relativistic velocities.

A number of schemes that lead to the physical generation of relativistic mirrors in laser plasmas have been described in theoretical and experimental studies (e.g., double-sided mirrors [Kulagin et al., 2007b; Esirkepov et al., 2009; Wu et al., 2010; Kiefer et al., 2013; Ma et al., 2014], oscillating mirrors [Bulanov et al., 1994; Lichters et al., 1996; Naumova et al., 2004; Wheeler et al., 2012; Vincenti, 2019], sliding mirrors [Pirozhkov et al., 2006], flying mirrors realized with strongly nonlinear Langmuir waves [Bulanov et al., 2003; Kando et al., 2007; Pirozhkov et al., 2007; Kando et al., 2009]) and, hence, have already proven

the feasibility of this concept. Relativistic mirrors in plasmas are nowadays actively studied as a unique tool for fundamental research (e.g., light intensification toward the Schwinger limit [Bulanov et al., 2003], investigation of photon–photon and Delbrück scattering [Koga et al., 2012; Koga et al., 2018], analog black hole to investigate Hawking radiation and the information loss paradox [Chen and Mourou, 2017; Chen and Mourou, 2020]) and for many practical applications in diverse fields; depending on whether the configuration is co-propagating or counter-propagating, relativistic mirrors might be used either for the acceleration of ions (e.g., for hadron therapy [Bulanov et al., 2002]) or for producing coherent high-brightness radiation with wavelengths ranging from x-rays to gamma-rays (e.g., for molecular imaging [Neutzo et al., 2000] and attosecond spectroscopy [Krausz and Ivanov, 2009]).

The first goal of our work is to develop a theory for less explored regimes of the laser-wakefield acceleration of electrons. We focus on the evolution of high-power laser pulse in plasma and its effect on the resulting parameters of the accelerated electron beams in the regime of strong interaction between the driver pulse and the electron density spikes of the co-propagating Langmuir wave. Also, we investigate the peculiarities of the laser-wakefield acceleration in the regime of ultrashort laser pulses and near-critical density plasmas, which is of high interest for the acceleration driven by high-repetition-rate laser systems. Our second goal is to extend the theory for the interaction of laser and counter-propagating relativistic mirror in the regime of strong incident electromagnetic wave, where the recoil effects cannot be neglected, and to search for novel or innovative schemes for physical realization of relativistic flying mirrors in underdense plasmas.

The work presented in this doctoral thesis is conducted on an exclusively theoretical level. Each of the research topics is first approached by simple (but not trivial) analytical model, which is then confronted with large-scale numerical simulations. Being in a close contact with experimental teams, however, the initial formulations and specifications of the topics to be studied, as well as the achieved results, have always been a subject of long mutual discussions. All the conditions and parameters used in this work are thus tightly connected to capabilities of experimental devices (either existing or under construction). Overall, the aim of our theoretical work is not only to provide a general description of investigated physical processes, but also to explain and interpret the results of ongoing experiments, as well as to suggest and predict new experiments to be carried out in future.

1.3 Author's role and contributions

My doctoral training has been supervised jointly by Dr. O. Klímo and Prof. S. V. Bulanov; it took place at the Department of Physical Electronics, Faculty of Nuclear Sciences and Physical Engineering, Czech Technical University in Prague and at the ELI Beamlines Centre, Institute of Physics, Czech Academy of Sciences. Since the beginning of my postgraduate studies, I have been involved in the European Regional Development Fund project “High Field Initiative” (HiFI) led by Prof. S. V. Bulanov, which is oriented on research of new physical regimes accessible with the next generation high-power laser systems. My research responsibilities within this project partially overlap with those considered in this doctoral thesis.

During my postgraduate studies, I have had a chance to take part in all the aspects of scientific work. I have been involved in the process of formulation and specification of research topics, I have received a systematic high-level training in analytical and numerical modeling of wide range of linear and nonlinear phenomena, I have been trained in development and

optimization of various scientific software designed for large-scale numerical simulations, I have learned how to setup and execute the simulations on computer clusters, how to efficiently analyze and interpret TB-scale data generated by the simulation codes, and how to produce clear and at the same time visually appealing figures. Last but not least, I have learned how to write research manuscripts properly, and how to communicate with editors and referees until the final publication of the obtained results in a scientific journal.

I have also gained an experience with grant applications. First, I successfully applied for the computational resources of the IT4Innovations National Supercomputing Center in Ostrava, Czech Republic. I have been a principal investigator or co-investigator of 6 projects, which received in total more than 4 millions core-hours within the open access grant competitions. As it turned out, these resources were important not only for me, but also for the operation of the whole scientific team of HiFI. Second, I received a funding from the Czech Academy of Sciences intended for short-term cooperation activities with leading research institutions in South and East Asia. I used these funds for two short and intense research internships in 2018 and 2019.

My first internship took place at the Leung Center for Cosmology and Particle Astrophysics, National Taiwan University in Taipei, Taiwan. There, I was working under the supervision of Prof. P. Chen, director of the institute, on the research related to relativistic mirrors. I have been involved in an ongoing project called “Analog Black Hole Evaporation via Lasers” (AnaBHEL), which aims at resolving the question, whether Hawking evaporation violates unitarity, and therefore results in the loss of information. The laboratory investigation of the Hawking effect is planned to be in this case realized using relativistic mirrors in the form of Langmuir waves that can be accelerated drastically and stopped abruptly by impinging high-power laser pulses on plasma targets with a density gradient. This is analogous to the late time evolution of black hole Hawking evaporation. During this internship, I have made initial attempts to describe the recoil effects of relativistic mirrors.

My second internship took place at the Kansai Photon Science Institute, National Institutes for Quantum and Radiological Science and Technology in Kyoto, Japan. There, I was working under the supervision of Dr. T. Kawachi, director of the institute, and Dr. T. Z. Esirkepov, senior principal researcher, also on the research related to relativistic mirrors. On the contrary to my previous internship, however, now the main research topic changed to the development of a novel scheme for physical realization of relativistic flying mirrors based on the density singularities in laser plasmas.

I have also played an important role in many other activities related to my postgraduate education. To name a few, I organized short-term visits and seminars of Prof. P. Chen and Dr. T. Kawachi at the ELI Beamlines Centre, I was involved in preparation of Memorandum of Understanding between the Institute of Physics and the Kansai Photon Science Institute which was signed by directors of both institutes, Dr. M. Prouza and Dr. T. Kawachi, in 2020, I was giving tutorials for the undergraduate courses “Numerical methods” and “Principles of plasma physics” at the Czech Technical University in Prague, I have been a member of several academic communities, namely “SPIE CTU in Prague Student Chapter,” “Prague EPS Young Minds Section,” and “SIAM Student Chapter Prague,” where I was actively engaged in popularization of science and organization of regular meetings and seminars. All of these activities were extremely beneficial in terms of gaining new knowledge and experience, efficient sharing of research findings and ideas, tightening of collaborations, and networking with fellow students and scientists.

The systematic efforts and involvement in highly stimulating environment have naturally resulted in a number of original scientific results. Regarding the laser-driven sources of electrons, the most important results achieved are the description of coupled electromagnetic

and electron rings originating from the laser-wakefield acceleration and the discovery of polarity reversal of wakefields excited by ultrashort laser pulses in near-critical density plasmas. Regarding the laser-driven sources of short-wavelength radiation, the most important results I took considerable part in are the description of the recoil effects of relativistic mirrors and the invention of novel scheme for physical realization of relativistic mirrors based on the density singularities in laser plasmas.

The research projects I have been working on and the achieved results are to a large extent described in publications of mine and my co-authors. In total, I have authored or co-authored 20 publications (9 publications in peer-reviewed journals, 8 publications in conference proceedings, and 3 book chapters), in 7 of which I serve as a corresponding author. The core of this doctoral thesis is based on the following four selected publications:

- I. Valenta, P., Grittani, G. M., Lazzarini, C. M., Klímo, O., and Bulanov, S. V. (2021). [On the electromagnetic-electron rings originating from the interaction of high-power short-pulse laser and underdense plasma](#). *Physics of Plasmas*, **28**(12):122104.
- II. Valenta, P., Esirkepov, T. Z., Koga, J. K., Nečas, A., Grittani, G. M., Lazzarini, C. M., Klímo, O., Korn, G., and Bulanov, S. V. (2020). [Polarity reversal of wakefields driven by ultrashort pulse laser](#). *Physical Review E*, **102**(5):053216.
- III. Valenta, P., Esirkepov, T. Z., Koga, J. K., Pirozhkov, A. S., Kando, M., Kawachi, T., Liu, Y. K., Fang, P., Chen, P., Mu, J., Korn, G., Klímo, O., and Bulanov, S. V. (2020). [Recoil effects on reflection from relativistic mirrors in laser plasmas](#). *Physics of Plasmas*, **27**(3):032109.
- IV. Mu, J., Esirkepov, T. Z., Valenta, P., Gu, Y., Jeong, T. M., Pirozhkov, A. S., Koga, J. K., Kando, M., Korn, G., and Bulanov, S. V. (2020). [Relativistic flying forcibly oscillating reflective diffraction grating](#). *Physical Review E*, **102**(5):053202.

These publications will be referred to in text by their Roman numerals.

The results obtained have been also presented at a number of international scientific conferences, workshops, and seminars. Some of my most important oral and poster communications of research related to Refs. I. – IV. are mentioned in Chapter 3. The quality of the research and of the presentations themselves has been appreciated by the scientific community by awarding two prizes for the best poster presentation at the “45th EPS Conference on Plasma Physics,” and at the “ELI Summer School 2021.” It is important to note that since the beginning of 2020, the communications and promotions of our research results have been heavily affected by the COVID-19 pandemics. Some conferences were either postponed or completely canceled, the others went eventually remote.

1.4 Outline of the thesis

The structure of this doctoral thesis is organized as follows:

Chapter 2 presents the theory of physical process related to the research topics under consideration. We note that since this doctoral thesis is primarily oriented on the presentation of the author’s original work, the content of this chapter is limited to rather concise compendium of formulas, describing only the most essential features. It includes ...

Chapter 3 contains closer details about the four selected papers (Refs. I. – IV.), their main contributions to the corresponding scientific fields, as well as a thorough description of the author's role.

Chapter 4 summarizes the content of this doctoral thesis and outlines possible directions for future research.

Appendix A contains a complete list of the author's publications as of the day of submission of this doctoral thesis, including the publications in peer-reviewed journals, conference proceedings, and as book chapters.

Appendix B contains the full texts (reproduced with permission) of the four selected publications (Refs. I. – IV.).

“There is nothing more practical than a good theory.”

– Gustav Kirchhoff (1824 – 1887)

2

Theoretical background

Introducing paragraph.

2.1 Interaction of laser and underdense plasma

Langmuir waves are perhaps the most essential physical entities considered within this doctoral thesis. They play a key role in the concepts of laser-wakefield acceleration and relativistic flying mirrors, which are presented in the following sections (Secs. 2.2 and 2.3).

2.1.1 Basic laser and plasma parameters

Maxwell's equations,

$$\nabla \cdot \mathbf{E} = \frac{\rho}{\varepsilon_0}, \quad (2.1)$$

$$\nabla \cdot \mathbf{B} = 0, \quad (2.2)$$

$$\nabla \times \mathbf{E} = \frac{\partial \mathbf{B}}{\partial t}, \quad (2.3)$$

$$\nabla \times \mathbf{B} = \mu_0 \mathbf{J} + \mu_0 \varepsilon_0 \frac{\partial \mathbf{E}}{\partial t}. \quad (2.4)$$

Scalar and vector potentials,

$$\mathbf{E} = -\nabla \phi - \frac{\partial \mathbf{A}}{\partial t}, \quad (2.5)$$

$$\mathbf{B} = \nabla \times \mathbf{A}. \quad (2.6)$$

Coulomb gauge, $\nabla \cdot \mathbf{A} = 0$.

Strength parameter:

$$a_0 = \quad (2.7)$$

$$\frac{d\mathbf{p}}{dt} = -e(\mathbf{E} + \mathbf{v} \times \mathbf{B}) \quad (2.8)$$

$$\frac{\partial \mathbf{P}}{\partial t} + (\mathbf{v} \cdot \nabla) \mathbf{P} = e \nabla \phi + e \frac{\partial \mathbf{A}}{\partial t} - e [\mathbf{v} \times (\nabla \times \mathbf{A})] \quad (2.9)$$

perpendicular component of momentum,

$$\frac{\partial p_{\perp}}{\partial t} + v_{\parallel} \frac{\partial p_{\perp}}{\partial z} = e \frac{\partial A_{\perp}}{\partial t} + ev_{\parallel} \frac{\partial A_{\perp}}{\partial z}, \quad (2.10)$$

$$p_{\perp} - eA_{\perp} = \text{const.} \quad (2.11)$$

parallel component of momentum

$$\frac{\partial p_{\parallel}}{\partial t} + v_{\parallel} \frac{\partial p_{\parallel}}{\partial z} = e \frac{\partial \phi}{\partial z} - ev_{\perp} \frac{\partial A_{\perp}}{\partial z}, \quad (2.12)$$

2.1.2 Finite-amplitude Langmuir waves

Let us here describe the propagation of finite-amplitude (i.e., the frequency of the wave depends on the amplitude) electromagnetic and Langmuir (electrostatic) waves in cold collisionless plasma. The exact solution to this problem was first found in Ref. [Akheizer and Polovin, 1956](#).

Starting with the Maxwell's equations and the hydrodynamic equations for the electron and ion fluid components, we may obtain the system of partial differential equations for coupled electromagnetic and Langmuir waves in the following compact form [[Farina and Bulanov, 2001](#); [Bulanov et al., 2013](#); [Bulanov, 2021](#)],

$$\Delta \mathbf{a} - \frac{\partial^2 \mathbf{a}}{\partial t^2} - \frac{\partial}{\partial t} \nabla \varphi = n_e \boldsymbol{\beta}_e - n_i \boldsymbol{\beta}_i, \quad (2.13)$$

$$\Delta \varphi = n_e - n_i, \quad (2.14)$$

$$\frac{\partial n_{\alpha}}{\partial t} + \nabla \cdot (n_{\alpha} \boldsymbol{\beta}_{\alpha}) = 0, \quad (2.15)$$

$$\frac{\partial \mathbf{P}_{\alpha}}{\partial t} = -\nabla (\rho_{\alpha} \varphi + \gamma_{\alpha}) + \boldsymbol{\beta}_{\alpha} \times \nabla \times \mathbf{P}_{\alpha}, \quad (2.16)$$

where φ and \mathbf{a} are the scalar and vector potentials, respectively (the Coulomb gauge is assumed, i.e., $\nabla \cdot \mathbf{a} = 0$), $\boldsymbol{\beta}_{\alpha}$ is the velocity of the fluid component, and n_{α} is the number density of the fluid component; the electron and ion fluid components are denoted by subscripts e and i , respectively, the subscript α is either e or i . The canonical momentum \mathbf{P}_{α} and the Lorentz factor γ_{α} are related to the kinetic momentum $\mathbf{p}_{\alpha} = \gamma_{\alpha} \boldsymbol{\beta}_{\alpha}$ as $\mathbf{P}_{\alpha} = \mathbf{p}_{\alpha} + \rho_{\alpha} \mathbf{a}$ and $\gamma_{\alpha} = \sqrt{1 + \|\mathbf{p}_{\alpha}\|^2}$, respectively, where $\rho_{\alpha} = -(q_{\alpha}/e)(m_e/m_{\alpha})$. Here and below we use dimensionless quantities; quantities having the units of length and time are normalized by c/ω_{pe} and ω_{pe} , respectively, velocities are normalized by c , momenta by $m_{\alpha}c$, scalar and vector potentials by $m_e c^2/e$ and $m_e c/e$, respectively, and the number densities are normalized by n_0 , where n_0 is the density of plasma components at the equilibrium state.

In the one-dimensional geometry (i.e., $\partial/\partial x = \partial/\partial y = 0$) the dependence of all quantities in Eqs. (2.13) – (2.16) on the coordinate and time can be expressed via new variables $\zeta = z - \beta_w t$ and $\tau = t - \beta_w z$, where β_w is the phase velocity of the Langmuir wave (i.e., we search for the solution in the form of a plane wave traveling at constant velocity). Note that $\beta_w = \beta_g$, where β_g is the group velocity of the electromagnetic wave; the group velocity of the Langmuir wave is in cold plasma equal to zero. For the sake of simplicity, we further assume

that the electromagnetic wave is circularly polarized; the equations for the scalar, $\varphi = \varphi(\zeta)$, and vector, $a_x + ia_y = a(\zeta) \exp(i\omega\tau)$, potentials then read as [Farina and Bulanov, 2001; Bulanov et al., 2013; Bulanov, 2021]

$$\frac{d^2\varphi}{d\zeta^2} = \frac{\beta_w}{1 - \beta_w^2} \left(\frac{\psi_e}{R_e} - \frac{\psi_i}{R_i} \right), \quad (2.17)$$

$$\frac{d^2a}{d\zeta^2} + \omega^2 a = a \frac{\beta_w}{1 - \beta_w^2} \left(\frac{\rho_e}{R_e} - \frac{\rho_i}{R_i} \right), \quad (2.18)$$

where ω is the angular frequency of the electromagnetic wave, $\psi_\alpha = \Gamma_\alpha + \rho_\alpha \varphi$, and $R_\alpha = \sqrt{\psi_\alpha^2 - (1 - \beta_w^2)(1 + \rho_\alpha^2 a^2)}$. The value of Γ_α is determined by the boundary conditions; e.g., if the electromagnetic field amplitude vanishes (i.e., $a = 0$ and $\varphi = 0$) and the plasma is at rest (i.e., $\|\mathbf{p}_\alpha\| = 0$) at infinity, then $\Gamma_\alpha = 1$. The Lorentz factors and the number densities of the electron and ion components can be expressed as functions of scalar and vector potentials [Farina and Bulanov, 2001; Bulanov et al., 2013; Bulanov, 2021],

$$\gamma_\alpha = \frac{R_\alpha}{1 - \beta_w^2} \left(\frac{\psi_\alpha}{R_\alpha} - \beta_w \right), \quad (2.19)$$

$$n_\alpha = \frac{\beta_w}{1 - \beta_w^2} \left(\frac{\psi_\alpha}{R_\alpha} - \beta_w \right). \quad (2.20)$$

In what follows we neglect the motion of ions, i.e., $\rho_i = 0$ (note that the ion motion affects the value of scalar potential in the Langmuir wave [Bulanov, 2021]).

Let us consider a Langmuir wave generated by given non-evolving electromagnetic pulse with piece-wise constant profile, e.g., $a = \text{const.}$ for $\zeta \leq 0$ and $a = 0$ for $\zeta > 0$. In this case, Eq. (2.17) takes the following form [Bulanov et al., 2016a; Bulanov, 2021],

$$\frac{d^2\varphi}{d\zeta^2} = \frac{\beta_w}{1 - \beta_w^2} \left(\frac{1 + \varphi}{\sqrt{(1 + \varphi)^2 - (1 - \beta_w^2)(1 + a^2)}} - \frac{1}{\beta_w} \right). \quad (2.21)$$

In the limit $\beta_w = \beta_g \rightarrow 1$ (corresponding to the case of low-density plasma, when the front of the electromagnetic pulse propagates at velocity close to c), Eq. (2.21) simplifies to [Bulanov et al., 1989; Berezhiani and Murusidze, 1990; Esarey et al., 2009; Bulanov et al., 2016a; Bulanov, 2021]

$$\frac{d^2\varphi}{d\zeta^2} = \frac{1}{2} \left(\frac{1 + a^2}{(1 + \varphi)^2} - 1 \right). \quad (2.22)$$

Analytical solution to Eq. (2.22) can be found in the implicit form as [Bulanov et al., 1989; Berezhiani and Murusidze, 1990; Bulanov et al., 2016a; Bulanov, 2021]

$$\zeta = 2 \left[\sqrt{\frac{(a^2 - \varphi)(1 + \varphi)}{\varphi}} + E \left(\sin \frac{1}{\sqrt{\varphi}}, -a^2 \right) \right], \quad (2.23)$$

where $E(\cdot, \cdot)$ is the incomplete elliptic integral of the second kind [Gradshteyn and Ryzhik, 1980].

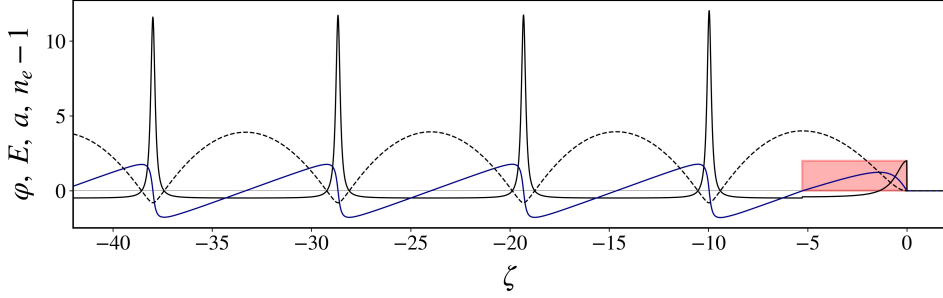


Figure 1: Dependence of the scalar potential (black dashed line), electric field (blue), and electron density perturbation (solid black line) on the coordinate ζ for the Langmuir wave generated by square electromagnetic pulse (red) with amplitude $a = 2$ and optimal length ($l_{opt} = 5.27$) given by Eq. (2.25). The values of scalar potential and electric field in the wake left behind the driving electromagnetic pulse vary from -0.8 to 4 and from ≈ -1.79 to ≈ 1.79 , respectively. The quantities are obtained numerically from Eq. (2.22).

By integrating Eq. (2.22) with the boundary conditions $\varphi(0) = d\varphi/d\zeta(0) = 0$ we get

$$\left(\frac{d\varphi}{d\zeta}\right)^2 = \frac{\varphi(a^2 - \varphi)}{1 + \varphi}. \quad (2.24)$$

From Eq. (2.24) one may find the optimal length of the driving electromagnetic pulse which maximizes the amplitude of the electric field, $E = -d\varphi/d\zeta$, within the Langmuir wave using the condition that $E = 0$ at the rear side of the pulse [Bulanov et al., 2016a; Bulanov, 2021],

$$l_{opt} = \int_0^{a^2} \sqrt{\frac{1 + \varphi}{\varphi(a^2 - \varphi)}} d\varphi = 2E(-a^2), \quad (2.25)$$

where $E(\cdot)$ is the complete elliptic integral of the second kind [Gradshteyn and Ryzhik, 1980]. In the limit of small-amplitude driving electromagnetic pulse (i.e., $a \ll 1$), we may approximate Eq. (2.25) as

$$l_{opt} = \pi + \frac{\pi}{4}a^2 - \frac{3\pi}{64}a^4 + \dots, \quad (2.26)$$

and the wavelength of the Langmuir wave is $\lambda_w = 4l_{opt}$ (i.e., $\lambda_w = 2\pi c/\omega_{pe}$ in dimensional units). In the opposite limit of large-amplitude electromagnetic pulse (i.e., $a \gg 1$), one gets

$$l_{opt} = 2a - \frac{1}{a} \ln a + \frac{1}{a} \left(\frac{1}{2} + 2 \ln 2 \right) - \dots, \quad (2.27)$$

and the Langmuir wave wavelength is $\lambda_w = 2l_{opt}$ (i.e., $\lambda_w = 4ac/\omega_{pe}$ in dimensional units). We see that λ_w is proportional to a .

The extrema of the scalar potential inside the electromagnetic pulse can be obtained from Eq. (2.24) using the condition $d\varphi/d\zeta = 0$. We find that the minimum and maximum values of φ are, respectively, $\varphi_{min} = 0$ and $\varphi_{max} = a^2$. The extrema of the electric field inside the electromagnetic pulse can be found from Eq. (2.22) using the condition $d^2\varphi/d\zeta^2 = 0$. The minimum and maximum values of E are thus $E_{min} = -\sqrt{1 + a^2} + 1$ and $E_{max} = \sqrt{1 + a^2} - 1$, respectively. In order to examine the extrema of scalar potential and electric field left behind the driving electromagnetic pulse of the optimal length given by Eq. (2.25), we integrate

Eq. (2.22) with $a = 0$ and use the boundary conditions $\varphi(-l_{opt}) = a^2$ and $d\varphi/d\zeta(-l_{opt}) = 0$,

$$\left(\frac{d\varphi}{d\zeta}\right)^2 = a^2 - \varphi - \frac{a^2 - \varphi}{(1 + a^2)(1 + \varphi)}. \quad (2.28)$$

Using the same approach as before, we find from Eq. (2.28) that $\varphi_{min} = -a^2/(1 + a^2)$, $\varphi_{max} = a^2$, $E_{min} = -a^2/\sqrt{1 + a^2}$, and $E_{max} = a^2/\sqrt{1 + a^2}$. Note that the amplitude of the electric field inside the driving electromagnetic pulse is smaller than the amplitude of the electric field in the wake left behind the driver.

Fig. 1 shows the dependence of scalar potential, electric field, and electron density perturbation on the coordinate ζ for the Langmuir wave generated by square electromagnetic pulse with amplitude $a = 2$ and optimal length given by Eq. (2.25). The quantities are obtained numerically from Eq. (2.22).

2.1.3 Breaking of Langmuir waves

The amplitude of the electric field in the Langmuir wave with a given value of β_w cannot be arbitrarily large. It has been found that if the electric field exceeds the Akhiezer-Polovin limit value of the field [Akhiezer and Polovin, 1956],

$$E_{AP} = \sqrt{2(\gamma_w - 1)}, \quad (2.29)$$

the Langmuir wave breaks. Here $\gamma_w = 1/\sqrt{1 - \beta_w^2}$ stands for the Lorentz factor of the Langmuir wave.

In this section we analyze the properties of Langmuir waves generated by a strong electromagnetic pulse as they approach the threshold of wave breaking. As closer discussed in Secs. ??, the breaking Langmuir waves are of high importance for the concept of laser-wakefield acceleration (they provide the electron self-injection into the accelerating regions of wakefield) as well as for the relativistic flying mirrors (they maximize the reflection coefficient of the mirrors realized with laser-driven Langmuir waves). Eqs. (2.14) - (2.16) can be rewritten in a single ordinary differential equation for the longitudinal component of the electron momentum p_e [Panchenko et al., 2008; Bulanov et al., 2013],

$$\frac{d^2}{d\zeta^2}(\gamma_e - \beta_w p_e) = \frac{p_e}{\beta_w \gamma_e - p_e}, \quad (2.30)$$

where we assume that $\gamma_e = \sqrt{1 + p_e^2 + a^2}$ (see also Sec. ??). One can immediately see that Eq. (2.30) becomes singular when the denominator on the right-hand side vanishes, i.e., when the electron velocity, p_e/γ_e , approaches the phase velocity of the Langmuir wave, β_w . This singularity, which is also known as the gradient or cusp catastrophe, corresponds to the breaking of Langmuir wave.

The structure of the breaking Langmuir wave can be revealed by expanding γ_e and p_e in the vicinity of the singularity, $\zeta = \zeta_{br} + \delta\zeta$, where ζ_{br} is the breaking coordinate and $\delta\zeta/\zeta_{br} \ll 1$. The electron momentum is expanded as $p_e = p_{br} + \delta p$, where $p_{br} = \beta_w \gamma_w \sqrt{1 + a_{br}^2}$, $\delta p/p_{br} \ll 1$, and $a_{br} = a(\zeta_{br})$. From Eq. (2.30) one gets [Panchenko et al., 2008; Bulanov et al., 2013]

$$\frac{d^2}{d\zeta^2} \delta p^2 = -2\beta_w \gamma_w^6 (1 + a_{br}^2) \delta p^{-1}. \quad (2.31)$$

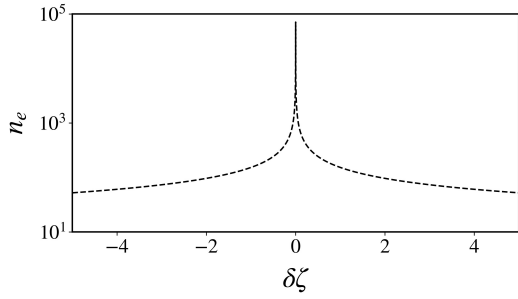


Figure 2: Distribution of electron density of the breaking Langmuir wave near the singularity according to Eq. (2.35).

After integrating Eq. (2.31) over ζ we obtain [Panchenko et al., 2008; Bulanov et al., 2013]

$$\left(\delta p \frac{d}{d\zeta} \delta p \right)^2 + 2\beta_w \gamma_w^6 (1 + a_{br}^2) \delta p = C, \quad (2.32)$$

where C is the integration constant (note that the value of C can be different in regions $\delta\zeta < 0$ and $\delta\zeta > 0$ since Eq. (2.31) is singular at $\delta\zeta \rightarrow 0$).

When the product $\delta p d\delta p/d\zeta \rightarrow 0$ at $\delta p \rightarrow 0$, which implies that $C = 0$, then [Panchenko et al., 2008; Bulanov et al., 2013]

$$\delta p = -\beta_w \gamma_w^2 \left(\sqrt{\frac{9}{2}} \sqrt{1 + a_{br}^2} \frac{\delta\zeta}{\beta_w} \right)^{2/3}. \quad (2.33)$$

The expression for the longitudinal electron velocity, β_e , then reads as [Panchenko et al., 2008; Bulanov et al., 2013]

$$\beta_e = \beta_w - \frac{\beta_w}{\gamma_w} \left(\sqrt{\frac{9}{2}} (1 + a_{br}^2)^{1/4} \frac{\delta\zeta}{\beta_w} \right)^{2/3}. \quad (2.34)$$

Finally, by plugging Eq. (2.34) into the solution to Eq. (2.15), we obtain the distribution of the electron density, n_e , of the breaking Langmuir wave in the vicinity of ζ_{br} as [Panchenko et al., 2008; Bulanov et al., 2013]

$$n_e = \frac{\beta_w}{\beta_w - \beta_e} \approx \gamma_w \left(\sqrt{\frac{2}{9}} (1 + a_{br}^2)^{1/4} \frac{\beta_w}{\delta\zeta} \right)^{2/3}. \quad (2.35)$$

Although for $\delta\zeta \rightarrow 0$ the electron density tends to infinity, the singularity is integrable. This means that in the breaking Langmuir wave there is a finite number of electrons [Panchenko et al., 2008; Bulanov et al., 2013]. The distribution of n_e given by Eq. (2.35) is shown in Fig. 2.

Singularities form naturally in the plasma flow with inhomogeneous velocity. There have been identified several kinds of singularities due to the breaking of finite-amplitude Langmuir waves depending on their closeness to the wave breaking threshold. It turned out that the dependence of the electron density on the coordinate can be in general expressed as

$n_e(\delta\zeta) \approx \delta\zeta^{-\alpha}$ with $1/2 \leq \alpha < 1$ [Panchenko et al., 2008].

2.2 Laser-wakefield acceleration of electrons

In this section, we briefly introduce the concept of electron acceleration by the laser-generated wakefield [Tajima and Dawson, 1979], i.e., the structure comprising the Langmuir wave and the associated longitudinal electric field. We first analyze the motion of electrons in the wakefield using the Hamiltonian formalism, ... An extensive study about the aspects of laser-wakefield accelerators can be found, e.g., in Refs. Esarey et al., 2009 and Bulanov et al., 2016a.

2.2.1 Electron interaction with Langmuir wave

The one-dimensional motion of an electron in the wakefield and the electromagnetic pulse can be described by means of a Hamiltonian [Esirkepov et al., 2006],

$$\mathcal{H} = \sqrt{m_e^2 c^4 + c^2 P_{\parallel}^2 + c^2 (P_{\perp} + eA_{\perp})^2} - e\phi, \quad (2.36)$$

where $P_{\parallel}(z, t)$ and $P_{\perp}(z, t)$ are the longitudinal and transverse components of the electron canonical momentum, respectively, $A_{\perp}(z, t)$ is the vector potential of the driving electromagnetic pulse, and $\phi(z, t)$ is the scalar potential of the wakefield. From here on, we use the normalizations of quantities introduced in Sec ?? and assume that A_{\perp} and ϕ depend only on variable ζ . To ensure this, we neglect the effect of dispersion on the driving pulse, and consider that the pulse is circularly polarized and the initial value of P_{\perp} is equal to zero.

The integral of motion of the Hamiltonian [Eq. (2.36)] can be written as

$$h(\zeta, P_{\parallel}) = \sqrt{1 + P_{\parallel}^2 + a^2} - \varphi - \beta_w P_{\parallel} = h_0, \quad (2.37)$$

where h_0 is a constant of the electron initial state. Eq. (2.37) states that the total energy (kinetic and potential) of the electron is conserved along its trajectory in phase space. For a given value of h_0 , we may express the electron trajectory as

$$P_{\parallel} = \beta_w \gamma_w^2 (h_0 + \varphi) \pm \gamma_w \sqrt{\gamma_w^2 (h_0 + \varphi)^2 - a^2 - 1}. \quad (2.38)$$

Fig. 3 (a) shows the phase plot of the system described by Eq. (2.37) in the case when the wakefield is generated by a Gaussian electromagnetic pulse with the envelope given by $a(\zeta) = a_0 \exp(-\zeta^2/l_p^2)$, where $a_0 = 2$ and $l_p^2 = 10$, in a plasma with $\beta_w = 0.99$. The dependence of the corresponding longitudinal electric field and the envelope of the driver pulse on the coordinate ζ is shown in Fig. 3 (b).

The possible electron trajectories in Fig. 3 (a) are obtained by varying the value of h_0 . We see that the phase space is divided into several domains, in which the electrons move either on closed or open orbits (depending on their initial state). These domains are separated from each other by special orbits, called separatrices. The separatrices join at singular points ζ_s (corresponding to the local minima of φ), which lie on the curve given by

$$P_{\parallel} = \beta_w \gamma_w \sqrt{1 + a^2}. \quad (2.39)$$

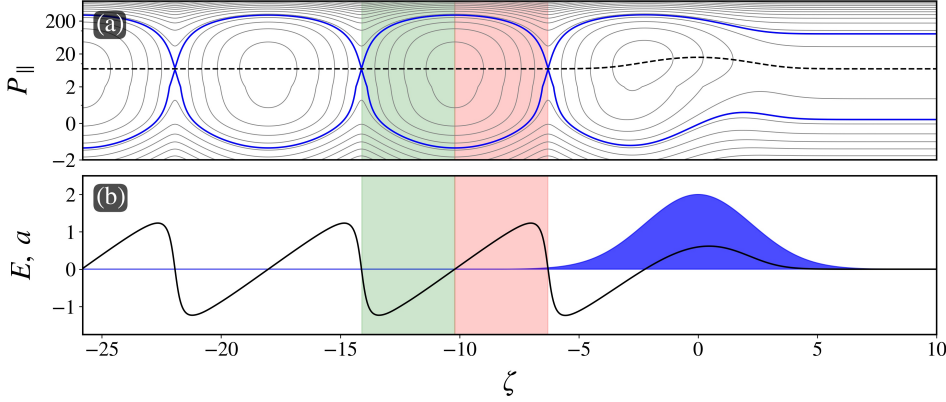


Figure 3: (a) Phase plot of the system described by Eq. (2.37) in the case when the wakefield is generated by a Gaussian electromagnetic pulse with the envelope given by $a(\zeta) = a_0 \exp(-\zeta^2/l_p^2)$, where $a_0 = 2$ and $l_p^2 = 10$, in a plasma with $\beta_w = 0.99$. The gray lines represent possible electron trajectories, the blue lines are for the separatrices [Eq. (2.40)], and the black dashed line is for the curve given by Eq. (2.39). (b) Dependence of the longitudinal electric field (black) and the envelope of the driving pulse (blue) on the coordinate ζ obtained numerically from Eq. (2.17). The green and red stripes in both plots mark, respectively, the regions in the second wakefield period where $E < 0$ and $E > 0$, i.e., where the injected electron is being accelerated and decelerated.

The separatrices themselves can be characterized by

$$h_s(\zeta, P_{\parallel}) = \frac{\sqrt{a^2(\zeta_s) + 1}}{\gamma_w} - \varphi(\zeta_s). \quad (2.40)$$

If the initial electron momentum is too low or too high, the electrons are untrapped by the wakefield potential and thus move on open orbits in phase space. In the former case, the electrons slip backward through the Langmuir wave, while in the latter case they eventually outrun the Langmuir wave. Only the electrons with the initial momentum within certain limits become trapped. Once trapped, they find themselves on closed orbits as they periodically gain and lose energy. The regions where the electrons gain and lose energy (i.e., the accelerating and decelerating regions) are displayed in Fig. 3 (a). Note that the threshold momentum required for trapping decreases for lower phase velocity and larger amplitude of the Langmuir wave [?].

There may exist also other separatrices that are not shown in Fig. 3 (a), e.g., the confining separatrix which encloses a domain of electron orbits trapped inside the potential well in the first period of the wakefield, or the ponderomotive separatrix [Esirkepov et al., 2006].

2.2.2 Limits of acceleration

2.3 Relativistic mirrors in underdense plasmas

In this section, we describe fundamental physical processes related to the interaction of electromagnetic waves with counter-propagating relativistic mirrors. We outline a possible physical realization as well as characteristics of the mirrors in underdense plasmas which are of great interest in the context of the development of coherent high-brightness radiation sources with wavelengths ranging from x-rays to gamma-rays. For a comprehensive study

about the relativistic mirrors in plasmas we refer the reader to Refs. [Bulanov et al., 2013](#) and [Bulanov et al., 2016b](#).

2.3.1 Relativistic flying flat mirror

First, we present a model of relativistic flying flat mirror which gives us a basic knowledge about the optical properties of reflected electromagnetic wave. The corresponding theory for the mirror propagating in vacuum at arbitrary (subluminal) velocity is known since 1905 [[Einstein, 1905](#)]. The theory is based on the application of the Lorentz transformation formalism, where the changes in the properties of reflected electromagnetic wave are explained by the double Doppler effect.

Let us consider an ideal relativistic flying flat mirror (i.e., the mirror reflection coefficient is equal to unity, no recoil effects on reflection) moving along the $+z$ -axis at a constant velocity $v_M = \beta_M c$. An electromagnetic wave packet linearly polarized along the x -axis is counter-propagating to the mirror (i.e., moving along the $-z$ -axis). The wave packet consists of a superposition of monochromatic waves, thus its electric field can be expressed in a stationary frame of reference, S_1 , using the Fourier transformation,

$$\begin{aligned} \mathbf{E}_i(x, y, z; t) &= \mathbf{e}_x \int_{-\infty}^{+\infty} \tilde{E}_0(x, y) \exp \left[-\frac{(\omega - \omega_0)^2}{2\Delta\omega^2} \right] \exp \left[i\omega \left(t + \frac{z}{c} \right) \right] d\omega \\ &= \mathbf{e}_x E_0(x, y) \exp \left[-\frac{1}{2\tau^2} \left(t + \frac{z}{c} \right)^2 \right] \exp \left[i\omega_0 \left(t + \frac{z}{c} \right) \right], \end{aligned} \quad (2.41)$$

where ω , ω_0 , and $\Delta\omega$ are, respectively, the angular frequency, center angular frequency, and the spectral bandwidth of the wave packet, $\tilde{E}_0(x, y)$ and $E_0(x, y) = \sqrt{2\pi}\Delta\omega\tilde{E}_0(x, y)$ are the electric field amplitudes in the spectral and time domains, respectively, and $\tau = 1/\Delta\omega$ is the wave packet duration (note that the full-width-at-half-maximum duration can be obtained as $\tau_{FWHM} = 2\sqrt{2\ln 2}\tau$).

Now we find the electric field of the incident wave packet, Eq. (2.41), in the frame of reference moving with the mirror, M , through the Lorentz transformation. The Lorentz transformation of coordinates is given by

$$x' = x, \quad y' = y, \quad z' = \frac{z - \beta_M ct}{\sqrt{1 - \beta_M^2}}, \quad t' = \frac{t - \frac{\beta_M}{c}z}{\sqrt{1 - \beta_M^2}}. \quad (2.42)$$

The components of electric field transform as

$$\mathbf{E}'_{i,\parallel} = \mathbf{E}_{i,\parallel}, \quad \mathbf{E}'_{i,\perp} = \frac{\mathbf{E}_{i,\perp} + \beta_M c \mathbf{e}_z \times \mathbf{B}_i}{\sqrt{1 - \beta_M^2}}, \quad (2.43)$$

where the subscripts \parallel and \perp denote the field polarization components parallel and perpendicular to the direction of mirror motion and $\mathbf{B}_i = -\mathbf{e}_z/c \times \mathbf{E}_i$ is the magnetic field of the incident wave packet in S_1 . Note that the origin of M is located at $(0, 0, z_0)$. In M , the electric field of the incident wave packet, Eq. (2.41) takes the following form,

$$\mathbf{E}'_i(x', y', z'; t') = \mathbf{e}'_x E'_0(x', y') \exp \left[-\frac{1}{2\tau'^2} \left(t' + \frac{z'}{c} \right)^2 \right] \exp \left[i\omega'_0 \left(t' + \frac{z'}{c} \right) \right], \quad (2.44)$$

where

$$E'_0(x', y') = \sqrt{\frac{1 + \beta_M}{1 - \beta_M}} E_0(x, y), \quad \tau' = \sqrt{\frac{1 - \beta_M}{1 + \beta_M}} \tau, \quad \omega'_0 = \sqrt{\frac{1 + \beta_M}{1 - \beta_M}} \omega_0. \quad (2.45)$$

As the incident wave packet experiences reflection from the mirror, its propagation direction reverses. The electric field of the reflected wave packet in M is thus given by

$$\mathbf{E}'_r(x', y', z'; t') = \mathbf{e}'_x E'_0(x', y') \exp \left[-\frac{1}{2\tau'^2} \left(t' - \frac{z'}{c} \right)^2 \right] \exp \left[i\omega'_0 \left(t' - \frac{z'}{c} \right) \right]. \quad (2.46)$$

Now we find the electric field of the reflected wave packet, Eq. (2.46), in another stationary reference frame, S_2 , the origin of which coincides with the origin of M , through the inverse Lorentz transformation. The inverse Lorentz transformation of coordinates is given by

$$x'' = x', \quad y'' = y', \quad z'' = \frac{z' + \beta_M c t'}{\sqrt{1 - \beta_M^2}}, \quad t'' = \frac{t' + \frac{\beta_M}{c} z'}{\sqrt{1 - \beta_M^2}}. \quad (2.47)$$

The components of electric field transform as

$$\mathbf{E}_{r,\parallel}'' = \mathbf{E}_{r,\parallel}', \quad \mathbf{E}_{r,\perp}'' = \frac{\mathbf{E}_{r,\perp}' - \beta_M c \mathbf{e}_z \times \mathbf{B}'_r}{\sqrt{1 - \beta_M^2}}, \quad (2.48)$$

where $\mathbf{B}'_r = \mathbf{e}_z/c \times \mathbf{E}'_r$ is the magnetic field of the reflected wave packet in M . In S_2 , the electric field of the reflected wave packet reads as

$$\mathbf{E}_r''(x'', y'', z''; t'') = \mathbf{e}_x'' E_0''(x'', y'') \exp \left[-\frac{1}{2\tau''^2} \left(t'' - \frac{z''}{c} \right)^2 \right] \exp \left[i\omega_0'' \left(t'' - \frac{z''}{c} \right) \right], \quad (2.49)$$

where

$$E_0''(x'', y'') = \sqrt{\frac{1 + \beta_M}{1 - \beta_M}} E'_0(x', y'), \quad \tau'' = \sqrt{\frac{1 - \beta_M}{1 + \beta_M}} \tau', \quad \omega_0'' = \sqrt{\frac{1 + \beta_M}{1 - \beta_M}} \omega'_0. \quad (2.50)$$

Finally, since $x'' = x$, $y'' = y$, $z'' = z - z_0$, and $t'' = t$, we may express the electric field of the reflected wave, Eq. (2.49), in the original stationary reference frame, S_1 , as

$$\begin{aligned} \mathbf{E}_r''(x, y, z; t) &= \mathbf{e}_x \frac{1 + \beta_M}{1 - \beta_M} E_0(x, y) \exp \left[-\left(\frac{1 + \beta_M}{1 - \beta_M} \right)^2 \frac{1}{2\tau^2} \left(t - \frac{z - z_0}{c} \right)^2 \right] \\ &\quad \times \exp \left[i \frac{1 + \beta_M}{1 - \beta_M} \omega_0 \left(t - \frac{z - z_0}{c} \right) \right]. \end{aligned} \quad (2.51)$$

For a Gaussian beam of width w_0 , $E_0(x, y) = E_0 \exp \left[-(x^2 + y^2)/2w_0^2 \right]$, and thus the total energy and peak intensity of the reflected pulse is given by

$$\mathcal{E}_r'' = \left(\frac{1 + \beta_M}{1 - \beta_M} \right) \sqrt{\frac{\pi^3}{4}} \varepsilon_0 c \tau w_0^2 E_0^2, \quad I_r'' = \left(\frac{1 + \beta_M}{1 - \beta_M} \right)^2 \frac{\varepsilon_0 c}{2} E_0^2. \quad (2.52)$$

Note that the factor $(1 + \beta_M)/(1 - \beta_M)$ can be rewritten in terms of the Lorentz factor of

the mirror, $\gamma_M = 1/\sqrt{1 - \beta_M^2}$, as follows,

$$\frac{1 + \beta_M}{1 - \beta_M} = \frac{\gamma_M + \sqrt{\gamma_M^2 - 1}}{\gamma_M - \sqrt{\gamma_M^2 - 1}} \approx 4\gamma_M^2, \quad (2.53)$$

where the last term is obtained using the identities $\gamma_M + \sqrt{\gamma_M^2 - 1} = (\gamma_M - \sqrt{\gamma_M^2 - 1})^{-1}$ and $\sqrt{\gamma_M^2 - 1} \approx \gamma_M$ and is valid in the relativistic limit, i.e., when $\gamma_M \gg 1$.

The above derivation shows that the reflected wave packet in the stationary frame of reference possesses several remarkable features: in the relativistic limit, its electric field is amplified by the factor $\approx 4\gamma_M^2$, its duration is compressed by $\approx 4\gamma_M^2$, and its angular frequency is upshifted by $\approx 4\gamma_M^2$. Furthermore, its energy and intensity are enhanced by $\approx 4\gamma_M^2$ and $\approx 16\gamma_M^4$, respectively. Assuming a laser pulse with parameters corresponding to a typical PW-class titanium-doped sapphire system, i.e., 0.8 μm wavelength, 30 fs duration, and 10^{18} W/cm^2 peak intensity, being reflected from ideal relativistic flying flat mirror with $\gamma_M = 10$, one obtains a pulse of wavelength 2 nm, duration 75 as, and the peak intensity $1.6 \times 10^{23} \text{ W/cm}^2$.

2.3.2 Relativistic flying parabolic mirror

Second, we present a model of relativistic flying parabolic mirror which, in addition to the flat mirror, describes the effect of focusing. The idea of using flying parabolic mirrors for the intensification of light has been first proposed in Ref. [Bulanov et al., 2003](#), where the mirror is realized by high-density electron shells of strongly nonlinear Langmuir wave driven by intense laser in underdense plasma (note that the surface where the electron density is maximal naturally takes a shape close to a paraboloid [[Bulanov and Sakharov, 1991](#); [Bulanov et al., 1995](#); [Matis et al., 2006](#); [Shadwick et al., 2002](#); [Maksimchuk et al., 2008](#)]).

Let us consider an ideal relativistic flying parabolic mirror (i.e., the reflection coefficient equal to unity, no recoil effects, no wavefront aberration) moving along the $+z$ -axis at a constant velocity $v_M = \beta_M c$. The spatiotemporal distribution of the electromagnetic wave packet reflected from the mirror can be again obtained by calculating first the distribution in the moving frame of reference and then performing the transformation back to the stationary frame. It is important to note that the focal length of the parabolic mirror in the moving frame is γ_M times shorter than in the stationary frame [[Bulanov et al., 2011](#); [Jeong et al., 2021](#)]; this alters the situation to the 4π -spherical focusing scheme [[Gonoskov et al., 2012](#); [Jeong et al., 2020](#)]. The distribution of the electromagnetic fields in the focal region of parabolic mirror in the moving frame has to be thus calculated under the conditions of 4π -spherical focusing.

The 4π -spherical focusing scheme corresponds to an extreme case of either tight-focusing (where the f -number approaches zero) or multiple beam focusing (where the number of beams approaches infinity). Therefore, it provides a theoretical limit to maximum attainable field strength at a given power [[Jeong et al., 2020](#)]. Under the conditions of 4π -spherical focusing, the field distributions are obtained by calculating the vector diffraction integrals. In what follows, we assume that the electromagnetic wave packet incident on the mirror is radially or azimuthally polarized (for this case the diffraction integrals can be calculated analytically). The electric field of the incident wave packet can be thus again described by Eq. (2.41), where $E_0(x, y)$ can be thought of as the Laguerre-Gaussian function, i.e., $E_0 \sim (\rho/\rho_0) \exp(-\rho^2/2\rho_0^2)$. Here we also introduce spherical coordinates $\rho = \sqrt{x^2 + y^2 + z^2}$ (the radial coordinate), $\theta = \arccos(z/\rho)$ (the polar coordinate), and $\phi = \arctan(y/x)$ (the azimuthal coordinate).

The mathematical expressions shown below cover only the case of radially polarized wave packet (the field distributions of the azimuthally polarized wave packet can be easily obtained by exchanging the expressions for the electric and magnetic fields of the radially polarized wave packet). Radial polarization is also interesting in the sense that the field distribution at focus forms a compact spot producing the maximum intensity (in contrast to, e.g., linear polarization which generates multiple intensity peaks instead).

In the moving frame of reference, the electric and magnetic fields of the 4π -spherical focused radially polarized wave packet are expressed in the frequency domain as [Jeong et al., 2020; Jeong et al., 2021]

$$\mathbf{E}'_f(\rho', \theta'; \omega) = \mathbf{e}'_\theta i E_{0,f}(\omega') S_a(\rho', \theta'; \omega') \exp(i\omega' t'), \quad (2.54a)$$

$$\mathbf{B}'_f(\rho', \theta'; \omega) = -\mathbf{e}'_\phi B_{0,f}(\omega') S_b(\rho', \theta'; \omega') \exp(i\omega' t'), \quad (2.54b)$$

where $E_{0,f}(\omega')$ and $B_{0,f}(\omega')$ are the peak amplitudes of the electric and magnetic fields at focus at a certain frequency ω' , and $S_a(\omega')$ and $S_b(\omega')$ are the spatial distribution functions defined as [Jeong et al., 2020; Jeong et al., 2021]

$$S_a(\omega') = j_0\left(\frac{\omega'}{c}\rho\right) + \frac{5}{2^3} j_2\left(\frac{\omega'}{c}\rho\right) P_2(\cos\theta') + \dots, \quad (2.55a)$$

$$S_b(\omega') = \frac{4}{\pi} j_1\left(\frac{\omega'}{c}\rho\right) P_1^1(\cos\theta'). \quad (2.55b)$$

Here $j_n(\cdot)$ is the n -th order spherical Bessel function of the first kind, and $P_n(\cdot)$ and $P_n^m(\cdot)$ are the Legendre and associated Legendre functions [Gradshteyn and Ryzhik, 1980].

The resultant expressions for the spatiotemporal distribution of electric and magnetic fields of the radially polarized wave packet in the focal region of the mirror in the stationary frame of reference are obtained through the inverse Lorentz transformation and a Fourier transformation in the frequency domain [Jeong et al., 2021],

$$\begin{aligned} \mathbf{E}''_f(\rho, \theta, \phi; t) &= \gamma_M \frac{1 + \beta_M}{1 - \beta_M} \sqrt{\frac{3\pi^5}{8}} \frac{w_e}{\lambda_0} E_0 \\ &\times \left[\begin{array}{l} \{-j_0(\omega'_0 R/c) \sin(\omega'_0 T) \Upsilon_1 + \beta_M j_1(\omega'_0 R/c) \cos(\omega'_0 T) \Upsilon_2\} \cos\phi \\ \{-j_0(\omega'_0 R/c) \sin(\omega'_0 T) \Upsilon_1 + \beta_M j_1(\omega'_0 R/c) \cos(\omega'_0 T) \Upsilon_2\} \sin\phi \\ (1/\gamma_M) j_0(\omega'_0 R/c) \sin(\omega'_0 T) \Upsilon_2 \end{array} \right], \end{aligned} \quad (2.56a)$$

$$\begin{aligned} \mathbf{B}''_f(\rho, \theta, \phi; t) &= \gamma_M \frac{1 + \beta_M}{1 - \beta_M} \sqrt{\frac{3\pi^5}{8}} \frac{w_e}{\lambda_0} \frac{E_0}{c} \\ &\times \left[\begin{array}{l} \{-j_1(\omega'_0 R/c) \cos(\omega'_0 T) \Upsilon_2 + \beta_M j_0(\omega'_0 R/c) \sin(\omega'_0 T) \Upsilon_1\} \sin\phi \\ \{j_1(\omega'_0 R/c) \cos(\omega'_0 T) \Upsilon_2 - \beta_M j_0(\omega'_0 R/c) \sin(\omega'_0 T) \Upsilon_1\} \cos\phi \\ 0 \end{array} \right]. \end{aligned} \quad (2.56b)$$

Here w_e is the effective radius of the wave packet ($w_e = w_0 \sqrt{2p + m + 1}$ for the p -th radial,

m -th azimuthal Laguerre-Gaussian beam), $\lambda_0 = 2\pi c/\omega_0$ is the wave packet wavelength,

$$\Upsilon_1(T, R) = \frac{1}{2} \left\{ \frac{\cos \theta + \beta_M}{1 + \beta_M \cos \theta} \exp \left[-\frac{\Delta\omega'^2}{4} \left(T + \frac{R}{c} \right)^2 \right] \right. \\ \left. + \frac{\cos \theta - \beta_M}{1 - \beta_M \cos \theta} \exp \left[-\frac{\Delta\omega'^2}{4} \left(T - \frac{R}{c} \right)^2 \right] \right\}, \quad (2.57a)$$

$$\Upsilon_2(T, R) = \frac{1}{2} \left\{ \frac{\sin \theta}{\gamma_M (1 - \beta_M \cos \theta)} \exp \left[-\frac{\Delta\omega'^2}{4} \left(T - \frac{R}{c} \right)^2 \right] \right. \\ \left. + \frac{\sin \theta}{\gamma_M (1 + \beta_M \cos \theta)} \exp \left[-\frac{\Delta\omega'^2}{4} \left(T + \frac{R}{c} \right)^2 \right] \right\} \quad (2.57b)$$

are the envelope functions, and

$$T(t, \rho) = \frac{t - (\rho/c) \beta_M \cos \theta}{\gamma_M (1 - \beta_M^2 \cos^2 \theta)}, \quad R(\rho, t) = \frac{\rho - ct \beta_M \cos \theta}{\gamma_M (1 - \beta_M^2 \cos^2 \theta)}. \quad (2.58)$$

The phase of the outgoing wave packet in the stationary frame of reference can be obtained by decomposing the spherical Bessel function in Eqs. (2.56a) or (2.56b) as $\omega'_0(T - R/c) = [(1 + \beta_M)/(1 - \beta_M \cos \theta)] \omega_0(t - \rho/c)$, thus the angular frequency is given by

$$\omega''_0 = \frac{1 + \beta_M}{1 - \beta_M \cos \theta} \omega_0. \quad (2.59)$$

In the relativistic limit ($\gamma_M \gg 1$) and in the forward direction ($\theta = 0$), the angular frequency is upshifted by the factor $\approx 4\gamma_M^2$, which is consistent to the case of relativistic flying flat mirror.

The spectral bandwidth of the outgoing wave packet in the stationary frame of reference is determined by the term $\Delta\omega'^2 (T - R/c)^2 / 4 = [(1 + \beta_M)/(1 - \beta_M \cos \theta)]^2 \Delta\omega^2 (t - \rho/c)^2 / 4$ in Eqs. (2.57a) or (2.57b), thus the duration is given by

$$\tau'' = \frac{1 - \beta_M \cos \theta}{1 + \beta_M} \tau. \quad (2.60)$$

Again, in the relativistic limit and the forward direction, the duration is compressed by the factor $\approx 4\gamma_M^2$, consistently to the case of relativistic flying flat mirror.

From Eqs. (2.56a) and (2.56b) it is also clear that the field strength and intensity of the reflected wave packet at focus of the relativistic flying parabolic mirror are in the relativistic limit enhanced by factors of $\approx 4\gamma_M^3 \sqrt{3\pi^5/8} (w_e/\lambda_0)$ and $\approx 16\gamma_M^6 (3\pi^5/8) (w_e/\lambda_0)^2$, respectively; thus in comparison with the relativistic flying flat mirror, the focusing provides additional enhancements of the field strength and intensity of $\approx \gamma_M \sqrt{3\pi^5/8} (w_e/\lambda_0)$ and $\approx \gamma_M^2 (3\pi^5/8) (w_e/\lambda_0)^2$, respectively. Assuming again a laser pulse of wavelength 0.8 μm , effective radius 3 μm , and peak intensity 10^{18} W/cm^2 being reflected from an ideal relativistic flying parabolic mirror with $\gamma_M = 10$, one obtains an intensity of $2.6 \times 10^{28} \text{ W/cm}^2$ at focus.

2.3.3 Reflection coefficient

In reality the reflection coefficient of relativistic flying mirrors in plasmas is, in general, very far from unity and, therefore, constitutes an important factor that has to be taken into

account. Here we present an estimation of the reflection coefficient for the mirror being physically realized with strongly nonlinear Langmuir wave in underdense plasma.

Let us consider a Langmuir wave near the threshold of breaking, which moves along the $+z$ -axis at a constant phase velocity $v_M = \beta_M c$. The counter-propagating electromagnetic wave incident on the mirror is characterized by the x -component of the vector potential $A_x(y, z; t)$; the interaction between the electromagnetic wave and the mirror is governed by the wave equation

$$\frac{\partial^2 A_x}{\partial t^2} - c^2 \left(\frac{\partial^2 A_x}{\partial y^2} + \frac{\partial^2 A_x}{\partial z^2} \right) + \omega_{pe}^2 A_x = 0, \quad (2.61)$$

where $\omega_{pe}(\zeta) = \sqrt{e^2 n(\zeta) / (\varepsilon_0 m_e \gamma_e)}$ is the relativistic Langmuir frequency, γ_e is the electron Lorentz factor (note that $\gamma_e = \gamma_M$ at the wave breaking coordinate ζ_{br}), $n(\zeta)$ is the distribution of the electron density within the Langmuir wave, and $\zeta = z - \beta_M c t$.

The form of Eq. (2.61) in the frame of reference moving with the mirror can be found using the Lorentz transformation as

$$\frac{d^2 a}{dz'^2} + (s^2 - \nu) a = 0. \quad (2.62)$$

Here $a(z')$ is the vector potential normalized by $m_e c/e$, $s = \sqrt{(\omega'_0/c)^2 - k_y'^2}$, and $\nu(z') = \omega_{pe}^2(z')/c^2$. We look for the solution of Eq. (2.62) in the form of

$$a = b_-(z') \exp(-isz') + b_+(z') \exp(isz'), \quad (2.63)$$

and impose the following boundary conditions on the functions $b_-(z')$ and $b_+(z')$: In the limit $z' \rightarrow +\infty$, functions $b_-(z')$ and $b_+(z')$ represent the amplitudes of the incident and reflected electromagnetic waves, respectively, i.e., we set $b_-(+\infty) = 1$ and $b_+(\infty) = \rho$. In the opposite limit $z' \rightarrow -\infty$, $b_-(z')$ is the amplitude of the transmitted wave and $b_+(z')$ vanishes, i.e., we set $b_-(-\infty) = \tau$ and $b_+(-\infty) = 0$. We also require the following condition on the derivative of a to be satisfied,

$$\frac{da}{dz'} = -isb_- \exp(-isz') + isb_+ \exp(isz'), \quad (2.64)$$

which implies that

$$\frac{db_+}{dz'} \exp(isz') = -\frac{db_-}{dz'} \exp(-isz'). \quad (2.65)$$

By plugging Eq. (2.63) into Eq. (2.62) and taking into account the condition of Eq. (2.65), we may write a system of equations for the functions b_- and b_+ in the following compact form,

$$\frac{d}{dz'} \begin{bmatrix} b_- \\ b_+ \end{bmatrix} = \frac{i\nu}{2s} \begin{bmatrix} \exp(2isz') & 1 \\ -1 & -\exp(-2isz') \end{bmatrix} \begin{bmatrix} b_- \\ b_+ \end{bmatrix}. \quad (2.66)$$

Assuming that the amplitude of the reflected wave is much smaller than the amplitude of the incident wave (i.e., $\rho \ll 1$), the solution of the system of Eqs. (2.66) can be written as

$$\rho = \frac{i}{2s} \int_{-\infty}^{+\infty} \nu(z') \exp(-2isz') dz'. \quad (2.67)$$

Since we consider a Langmuir wave at the threshold of wave breaking, we may use Eq. (2.35) to describe the distribution of the electron density. In the moving frame of

reference, in which the Langmuir wave is at rest, this yields

$$\nu = \frac{(2/9)^{1/3} (1 + a_{br}^2)^{1/6} k_p^{4/3} \gamma_M^{2/3}}{(z')^{2/3}}. \quad (2.68)$$

After substituting Eq. (2.68) into Eq. (2.67) and calculating the integral we obtain

$$\rho = \frac{i 3^{1/2} \Gamma(1/3) (2/9)^{1/3} (1 + a_{br}^2)^{1/6} k_p^{4/3} \gamma_M^{2/3}}{(2s)^{4/3}}, \quad (2.69)$$

where $\Gamma(\cdot)$ is the Euler gamma function [Gradshteyn and Ryzhik, 1980]. Finally, the reflection coefficient can be obtained as follows,

$$\mathcal{R} = \|\rho\|^2 = \frac{\Gamma^2(1/3) (1 + a_{br}^2)^{1/3} k_p^{8/3} \gamma_M^{4/3}}{2^2 3^{1/3} s^{8/3}}. \quad (2.70)$$

It is important to note that the formula for the reflection coefficient given by Eq. (2.70) is calculated in the moving frame of reference. In the stationary frame, it has to be interpreted as a reflection coefficient in terms of the photon number.

2.3.4 Recoil effects

Furthermore, the calculations presented above are valid only if the amplitude of the electromagnetic wave incident on the relativistic mirror is sufficiently low. When the amplitude is high, the electromagnetic wave may significantly affect the mirror motion (i.e., the radiation pressure of the wave may slow down or destroy the mirror) even if the mirror reflection coefficient is small. The knowledge of the onset of recoil effects associated with the interaction of the relativistic mirror and strong incident electromagnetic wave is thus crucial for maximizing the amplitude of the reflected wave.

The recoil effects of relativistic mirrors physically realized by the structures in laser plasmas have been recently investigated in one-dimensional [III.] and two-dimensional [Jeong et al., 2021] geometries. Here we present the one-dimensional description. Let us consider a relativistic mirror in the form of an electron layer interacting with a counter-propagating electromagnetic wave. We assume that all the electrons are characterized by the same momentum, the electromagnetic wave is monochromatic with the angular frequency ω_0 , and the reflection coefficient (in terms of photon number) is equal to \mathcal{R} . The conservation of momentum and energy before (unprimed quantities) and after (double-primed quantities) the interaction can be written as [III.]

$$\mathcal{N}_e p_e - \mathcal{N}_\omega p_\omega = \mathcal{N}_e p_e'' + \mathcal{R} \mathcal{N}_\omega p_\omega'' - (1 - \mathcal{R}) \mathcal{N}_\omega p_\omega, \quad (2.71a)$$

$$\mathcal{N}_e \mathcal{E}_e + \mathcal{N}_\omega \mathcal{E}_\omega = \mathcal{N}_e \mathcal{E}_e'' + \mathcal{R} \mathcal{N}_\omega \mathcal{E}_\omega'' + (1 - \mathcal{R}) \mathcal{N}_\omega \mathcal{E}_\omega. \quad (2.71b)$$

Here \mathcal{N} , p , and \mathcal{E} are the numbers, momenta, and energies of the interacting particles, respectively, and the subscripts e and ω denote the electrons (representing the relativistic flying mirror) and photons (representing the incident electromagnetic wave), respectively. The electron and photon momenta can be expressed as $p_e = m_e c \sqrt{\gamma_M^2 - 1}$ and $p_\omega = \hbar \omega_0 / c$, respectively, and the electron and photon energies are $\mathcal{E}_e = m_e c^2 \gamma_M$ and $\mathcal{E}_\omega = \hbar \omega_0$, respectively, where \hbar stands for the reduced Planck constant. The schematic of the analytical model is displayed in Fig. 4.

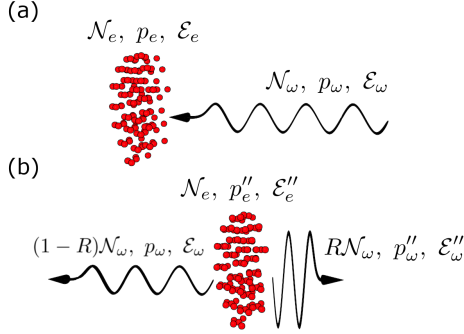


Figure 4: Schematic illustrating the analytical model of Eqs. (2.71) (a) before and (b) after the interaction of incident electromagnetic wave with a counter-propagating relativistic mirror, which is represented by thin electron layer (red dots).

By combining Eqs. (2.71) we obtain the following formula [III.],

$$\hbar\omega_0'' = \hbar\omega_0 \frac{\mathcal{E}_e (\mathcal{E}_e + p_e c)}{\mathcal{N}_e (\mathcal{E}_e + p_e c) + 2\mathcal{R}\mathcal{N}_\omega \hbar\omega_0} = \hbar\omega_0 \frac{\mathcal{N}_e m_e c^2 (\gamma_M + \sqrt{\gamma_M^2 - 1})}{\mathcal{N}_e m_e c^2 (\gamma_M - \sqrt{\gamma_M^2 - 1}) + 2\mathcal{R}\mathcal{N}_\omega \hbar\omega_0}. \quad (2.72)$$

In the relativistic limit, Eq. (2.72) can be simplified as

$$\omega_0'' \approx 4\gamma_M^2 \omega_0 \frac{\mathcal{N}_e m_e c^2 / 4\gamma_M}{\mathcal{N}_e m_e c^2 / 4\gamma_M + \mathcal{R}\mathcal{N}_\omega \hbar\omega_0} \approx 4\gamma_M^2 \omega_0 \left(1 - \frac{\mathcal{R}\mathcal{N}_\omega \hbar\omega_0}{\mathcal{N}_e m_e c^2 / 4\gamma_M} \right). \quad (2.73)$$

The fraction in parentheses on the right-hand side of Eq. (2.73) is the ratio between the energy of interacting photons (numerator) and the energy of electron layer (denominator), and it represents the correction to the frequency shift of the reflected wave by the recoil effects. The resulting frequency shift is determined by the relationship between both terms [III.],

$$\frac{\omega_0''}{\omega_0} \approx 4\gamma_M^2 \quad \text{if} \quad \mathcal{R}\mathcal{N}_\omega \hbar\omega_0 \ll \frac{\mathcal{N}_e m_e c^2}{4\gamma_M}, \quad (2.74a)$$

$$\frac{\omega_0''}{\omega_0} \approx \frac{\mathcal{N}_e m_e c^2 \gamma_M}{\mathcal{R}\mathcal{N}_\omega \hbar\omega_0} \quad \text{if} \quad \mathcal{R}\mathcal{N}_\omega \hbar\omega_0 \gg \frac{\mathcal{N}_e m_e c^2}{4\gamma_M}. \quad (2.74b)$$

The limit given by Eq. (2.74a) corresponds to the approximation of a weak incident electromagnetic wave and produces the classical frequency upshift factor as derived in Secs. 2.3.1 and 2.3.2. In the opposite limit given by Eq. (2.74b), the incident electromagnetic wave significantly affects the motion of the mirror so that the frequency of the reflected wave is in fact downshifted, as in the case of receding mirror. We define the threshold characterizing the importance of recoil effects in this interaction as a midpoint between the limits given by Eqs. (2.74a) and (2.74b), i.e., when the energy of the interacting photons is comparable to that of the electron layer [III.],

$$\mathcal{R}\mathcal{N}_\omega \hbar\omega_0 = \varkappa \frac{\mathcal{N}_e m_e c^2}{4\gamma_M}. \quad (2.75)$$

Here $\varkappa \ll 1$, i.e., much less energy than the kinetic energy of the mirror can affect the reflection process. The value of \varkappa was estimated using particle-in-cell simulations to $\approx 10^{-4}$ for the case of relativistic mirror realized with strongly nonlinear Langmuir wave [III].

2.4 Particle-in-cell method

In order to investigate various nonlinear phenomena involved in the collective behavior of particles and strong electromagnetic fields in the full three-dimensional geometry, one has to use numerical simulations. In this section we present the particle-in-cell method, which appears to be very convenient (among others) also for the investigations of the interaction of intense laser pulses with underdense plasmas, particularly on the $\mu\text{m} - \text{mm}$ spatial and $\text{fs} - \text{ps}$ temporal scales. We provide a brief description of the particle-in-cell method and closer discuss the core elements of the algorithm, namely particle pusher, field solver, field weighting, and particle weighting. An extensive study of the method can be found, e.g., in Refs. [Dawson, 1983](#); [Hockney and Eastwood, 1988](#); [Grigoryev et al., 2002](#); [Birdsall and Langdon, 2004](#).

2.4.1 General description

In the particle-in-cell method, the evolution of a system is determined by the motion of individual particles. However, real systems are in general very large in terms of a number of particles they contain. The particle-in-cell method therefore uses a finite set of so-called quasi-particles, each representing a group of physical particles that are near each other in the phase space. A quasi-particle becomes a carrier of certain attributes, e.g., mass, charge, position in space, momentum, etc. As shown below, it is possible to rescale the number of particles in the system, since the Lorentz force acting on the particles depends only on the charge to mass ratio, which is invariant to this transformation.

The particle-in-cell algorithm combines the Eulerian and Lagrangian approaches of the mathematical description. The electromagnetic fields are calculated on a fixed mesh (Eulerian frame), whereas the quasi-particles can move in a continuous phase space (Lagrangian frame). The algorithm is outlined below for regular spaced three-dimensional Cartesian grid, therefore we may discretize the spatial coordinate as $\mathbf{r} \rightarrow \mathbf{r}_{i,j,k}$, where $(i, j, k) \in \mathbb{Z}^3$ are the grid indices. If Δx , Δy , and Δz are the spatial steps in each direction, then $\mathbf{r}_{i,j,k} = (i\Delta x, j\Delta y, k\Delta z)$. The time is discretized as $t \rightarrow t^n$, where $n \in \mathbb{N}$ is the time level index. If Δt is the time step, then $t^n = n\Delta t$. Each quantity $A(\mathbf{r}_{i,j,k}, t^n)$ is hereafter denoted as $A_{i,j,k}^n$.

In kinetic theory, each particle species s in the system is assigned a distribution function $f_s(\mathbf{r}, \mathbf{p}, t)$, where \mathbf{r} and \mathbf{p} denote, respectively, the position and momentum of a phase-space element, and t is time. In the case of collisionless plasma, the evolution of f_s is governed by the Vlasov equation

$$\left(\frac{\partial}{\partial t} + \frac{\mathbf{p}}{m_s \gamma} \cdot \nabla + \mathbf{F}_L \cdot \frac{\partial}{\partial \mathbf{p}} \right) f_s = 0, \quad (2.76)$$

where $\mathbf{F}_L = q_s (\mathbf{E} + \mathbf{v} \times \mathbf{B})$ is the Lorentz force that stems from the existence of collective electric, $\mathbf{E}(\mathbf{r}, t)$, and magnetic, $\mathbf{B}(\mathbf{r}, t)$, fields in plasma, $\mathbf{v} = \mathbf{p}/(m_s \gamma)$, and $\gamma = \sqrt{1 + \mathbf{p}^2/(m_s^2 c^2)}$.

The particle-in-cell algorithm assumes that f_s is obtained by summing the distribution functions $f_{p,s}(\mathbf{r}, \mathbf{p}, t)$ of each quasi-particle p of species s ,

$$f_s = \sum_p f_{p,s}. \quad (2.77)$$

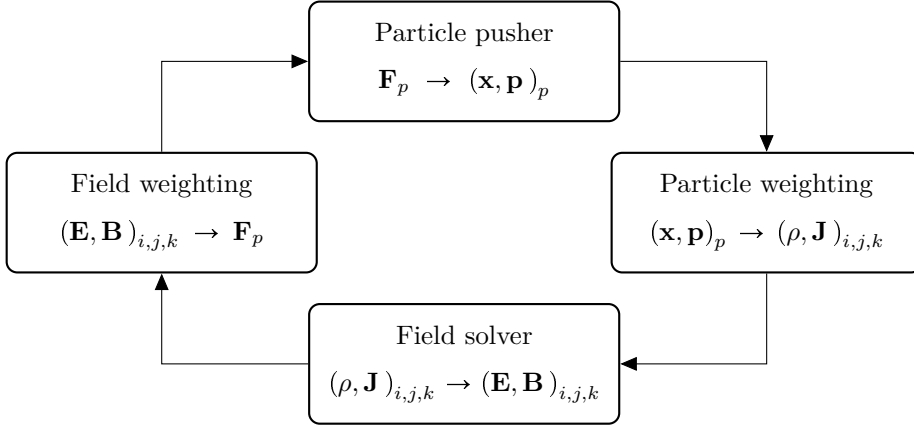


Figure 5: Fundamental steps of the computational cycle of the particle-in-cell method (taken from Ref. Valenta, 2017).

Here and below we use the subscript p to denote the quantities attributed to quasi-particles or evaluated at the quasi-particle positions. The quasi-particle distribution function can be defined as

$$f_{p,s}(\mathbf{r}, \mathbf{p}, t) = w_p S^r [\mathbf{r} - \mathbf{r}_p(t)] S^p [\mathbf{p} - \mathbf{p}_p(t)], \quad (2.78)$$

where S^r and S^p are the shape functions for the position and momentum variables, respectively, and w_p is the weight of the quasi-particle (i.e., a number of physical particles which the quasi-particle represents).

The shape functions cannot be chosen arbitrarily, they have to satisfy the following requirements: (i) the shape function is symmetric, (ii) the integral of the shape function is equal to unity, and (iii) the support of the shape function is compact. A standard implementation of the particle-in-cell algorithm is based on the choice of S^r as the B-spline function (covering one or up to few cells according to its order) and S^p as the Dirac δ -function. Note that smoother shape functions are used to reduce numerical noise and non-physical fluctuations in the simulations (at the cost of increased computational time).

The equations of motion for quasi-particle p can be obtained by substituting Eq. (2.77) into Eq.(2.76) and taking into account the properties of shape functions mentioned above,

$$\frac{d\mathbf{r}_p}{dt} = \frac{\mathbf{u}_p}{\gamma}, \quad (2.79)$$

$$\frac{d\mathbf{u}_p}{dt} = \frac{q_s}{m_s} \left(\mathbf{E}_p + \frac{\mathbf{u}_p}{\gamma} \times \mathbf{B}_p \right), \quad (2.80)$$

where $\mathbf{u}_p = \mathbf{p}_p/m_s$.

The core elements of the the particle-in-cell computational cycle are shown in Fig. 5. Having the information about the quasi-particle positions, \mathbf{r}_p , and momenta, \mathbf{p}_p , at a given time step, we calculate the charge, $\rho_{i,j,k}$, and current, $\mathbf{J}_{i,j,k}$, densities at each grid point (particle weighting). Then, the electric, $\mathbf{E}_{i,j,k}$, and magnetic, $\mathbf{B}_{i,j,k}$, fields at each grid point are advanced by solving the Maxwell's equations (field solver). After that, the new values of the electric and magnetic fields are interpolated back to the quasi-particle positions (field weighting). Finally, we calculate the new quasi-particle positions and momenta by solving the Newton-Lorentz equations of motion (particle pusher). The whole cycle repeats until the end

of simulation. We note that additional operations are usually performed in between these fundamental steps (e.g., current filtering, application of external fields, diagnostics, etc.).

2.4.2 Particle pusher

The motion of quasi-particles in the simulation, which is governed by Eqs. (2.79) and (2.80), can be solved numerically, e.g., using the explicit leap-frog scheme [Press et al., 2007],

$$\frac{\mathbf{r}_p^{n+1} - \mathbf{r}_p^n}{\Delta t} = \frac{\mathbf{u}_p^{n+1/2}}{\gamma^{n+1/2}}, \quad (2.81)$$

$$\frac{\mathbf{u}_p^{n+1/2} - \mathbf{u}_p^{n-1/2}}{\Delta t} = \frac{q_s}{m_s} \left(\mathbf{E}_p^n + \frac{\mathbf{u}_p^{n+1/2} + \mathbf{u}_p^{n-1/2}}{2\gamma^n} \times \mathbf{B}_p^n \right). \quad (2.82)$$

The effect of the electric, \mathbf{E}_p^n , and magnetic, \mathbf{B}_p^n , fields on quasi-particles in Eq. (2.82) can be efficiently separated by the Boris method [Boris, 1971]: By plugging

$$\mathbf{u}_p^{n-1/2} = \mathbf{u}_p^- - \frac{q_s \mathbf{E}_p^n}{m_s} \frac{\Delta t}{2} \quad (2.83a)$$

and

$$\mathbf{u}_p^{n+1/2} = \mathbf{u}_p^+ + \frac{q_s \mathbf{E}_p^n}{m_s} \frac{\Delta t}{2} \quad (2.83b)$$

into Eq. (2.82), one obtains

$$\frac{\mathbf{u}_p^+ - \mathbf{u}_p^-}{\Delta t} = \frac{q_s}{m_s} \frac{(\mathbf{u}_p^+ + \mathbf{u}_p^-)}{2\gamma^n} \times \mathbf{B}_p^n. \quad (2.84)$$

Eq. (2.84) describes pure rotation of the vector \mathbf{u}_p^- to \mathbf{u}_p^+ during a single simulation time step Δt , i.e., to obtain $\mathbf{u}_p^{n+1/2}$, we may first add half of the electric impulse \mathbf{E}_p^n to $\mathbf{u}_p^{n-1/2}$, then perform the full rotation according to Eq. (2.84), and finally add another half of the electric impulse \mathbf{E}_p^n to \mathbf{u}_p^+ .

The practical implementation of the algorithm can be summarized as follows: First, we express \mathbf{u}_p^- from Eq. (2.83a) and construct an auxiliary vector $\tilde{\mathbf{u}}_p$ which is simultaneously perpendicular to vectors $(\mathbf{u}_p^+ - \mathbf{u}_p^-)$ and \mathbf{B}_p^n ,

$$\tilde{\mathbf{u}}_p = \mathbf{u}_p^- + \mathbf{u}_p^- \times \mathbf{t}, \quad \mathbf{t} = \frac{q_s}{m_s} \frac{\mathbf{B}_p^n}{\gamma^n} \frac{\Delta t}{2}. \quad (2.85)$$

Using the fact that the vector $(\tilde{\mathbf{u}}_p \times \mathbf{B}_p^n)$ is parallel to $(\mathbf{u}_p^+ - \mathbf{u}_p^-)$, we express \mathbf{u}_p^+ as

$$\mathbf{u}_p^+ = \mathbf{u}_p^- + \mathbf{u}_p' \times \mathbf{s}, \quad \mathbf{s} = \frac{2\mathbf{t}}{1+t^2}. \quad (2.86)$$

Note that the transition from \mathbf{u}_p^- to \mathbf{u}_p^+ can be written in a more compact form as $\mathbf{u}_p^+ = \mathbb{M}\mathbf{u}_p^-$, where

$$\mathbb{M} = \begin{bmatrix} 1 - s_2 t_2 - s_3 t_3 & s_2 t_1 + s_3 & s_3 t_1 - s_2 \\ s_1 t_2 - s_3 & 1 - s_1 t_1 - s_3 t_3 & s_3 t_2 + s_1 \\ s_1 t_3 + s_2 & s_2 t_3 - s_1 & 1 - s_1 t_1 - s_2 t_2 \end{bmatrix}. \quad (2.87)$$

Finally, we substitute the vector \mathbf{u}_p^+ into Eq. (2.83b) and calculate the new values of quasi-particle momenta, $\mathbf{u}_p^{n+1/2}$, and positions, \mathbf{r}_p^{n+1} . For the alternatives to Boris solver, the reader can refer to, e.g., Refs. [Vay, 2008](#); [Higuera and Cary, 2017](#).

2.4.3 Field solver

The integration of the Maxwell's equations in time on the Cartesian grid is in the particle-in-cell algorithm usually carried out using the standard finite-difference time-domain method [[Yee, 1966](#)]. In this method, the vector components of the electric, $\mathbf{E}_{i,j,k}$, and magnetic, $\mathbf{B}_{i,j,k}$, fields are spatially staggered about the rectangular cells of the grid,

$$\mathbf{E}_{i,j,k} := \left[(E_x)_{i,j+1/2,k+1/2}, (E_y)_{i+1/2,j,k+1/2}, (E_z)_{i+1/2,j+1/2,k} \right], \quad (2.88)$$

$$\mathbf{B}_{i,j,k} := \left[(B_x)_{i+1/2,j,k}, (B_y)_{i,j+1/2,k}, (B_z)_{i,j,k+1/2} \right]. \quad (2.89)$$

The components of the current density, $\mathbf{J}_{i,j,k}$, are defined in the same way as the components of $\mathbf{E}_{i,j,k}$ and the charge density, $\rho_{i,j,k}$, is defined in the middle of the cell,

$$\mathbf{J}_{i,j,k} := \left[(J_x)_{i,j+1/2,k+1/2}, (J_y)_{i+1/2,j,k+1/2}, (J_z)_{i+1/2,j+1/2,k} \right], \quad (2.90)$$

$$\rho_{i,j,k} := \rho_{i+1/2,j+1/2,k+1/2}. \quad (2.91)$$

The illustration of this scheme, also known as the Yee lattice, is shown in Fig. 6.

The standard finite-difference time-domain method uses centered finite differences to approximate space and time derivatives achieving the second-order accuracy. The Maxwell's equations, being discretized using the explicit leap-frog scheme [[Press et al., 2007](#)], take the following form,

$$\nabla^+ \cdot \mathbf{E}_{i,j,k}^n = \frac{\rho_{i,j,k}^n}{\varepsilon_0}, \quad (2.92)$$

$$\nabla^- \cdot \mathbf{B}_{i,j,k}^{n+1/2} = 0, \quad (2.93)$$

$$\nabla^- \times \mathbf{E}_{i,j,k}^n = -\frac{\mathbf{B}_{i,j,k}^{n+1/2} - \mathbf{B}_{i,j,k}^{n-1/2}}{\Delta t}, \quad (2.94)$$

$$\nabla^+ \times \mathbf{B}_{i,j,k}^{n+1/2} = \mu_0 \mathbf{J}_{i,j,k}^{n+1/2} + \frac{1}{c^2} \frac{\mathbf{E}_{i,j,k}^{n+1} - \mathbf{E}_{i,j,k}^n}{\Delta t}. \quad (2.95)$$

The operators ∇^+ and ∇^- used in Eqs. (2.92) – (2.95) act on a scalar field $f_{i,j,k}$ as follows [[Esirkepov, 2001](#)],

$$\nabla^+ f_{i,j,k} = \left[\frac{f_{i+1,j,k} - f_{i,j,k}}{\Delta x}, \frac{f_{i,j+1,k} - f_{i,j,k}}{\Delta y}, \frac{f_{i,j,k+1} - f_{i,j,k}}{\Delta z} \right], \quad (2.96)$$

$$\nabla^- f_{i,j,k} = \left[\frac{f_{i,j,k} - f_{i-1,j,k}}{\Delta x}, \frac{f_{i,j,k} - f_{i,j-1,k}}{\Delta y}, \frac{f_{i,j,k} - f_{i,j,k-1}}{\Delta z} \right]. \quad (2.97)$$

These operators have the following properties [[Esirkepov, 2001](#)],

$$\nabla^- \cdot \nabla^- \times = \nabla^+ \cdot \nabla^+ \times = 0, \quad \nabla^- \cdot \nabla^+ = \nabla^+ \cdot \nabla^- = \Delta^\pm, \quad (2.98)$$

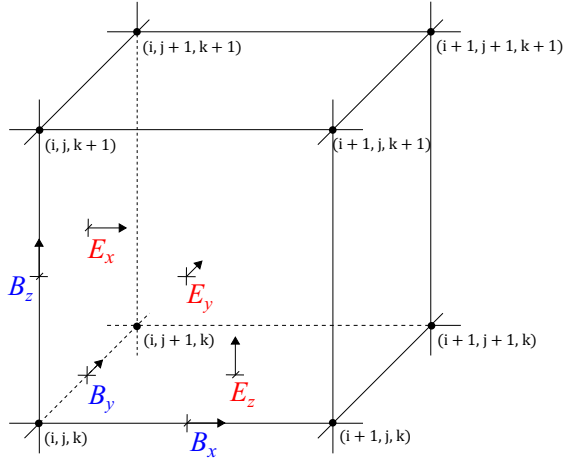


Figure 6: Standard Cartesian Yee cell used in the finite-difference time-domain method (taken from Ref. [Valenta, 2017](#)).

where the symbol Δ^\pm stands for the discrete Laplace operator [[Esirkepov, 2001](#)],

$$\begin{aligned} \Delta^\pm f_{i,j,k} = & \frac{f_{i-1,j,k} - 2f_{i,j,k} + f_{i+1,j,k}}{\Delta x^2} \\ & + \frac{f_{i,j-1,k} - 2f_{i,j,k} + f_{i,j+1,k}}{\Delta y^2} + \frac{f_{i,j,k-1} - 2f_{i,j,k} + f_{i,j,k+1}}{\Delta z^2}. \end{aligned} \quad (2.99)$$

It is important to realize that, in the three-dimensional case, the system of Eqs. (2.92) – (2.95) represents 8 first-order differential equations for 6 unknown vector components. Acting on Eqs. (2.94) and (2.95) by the operators $(\nabla^+ \cdot)$ and $(\nabla^- \cdot)$, respectively, one obtains

$$\frac{\nabla^- \cdot \mathbf{B}_{i,j,k}^{n+1/2} - \nabla^- \cdot \mathbf{B}_{i,j,k}^{n-1/2}}{\Delta t} = 0, \quad (2.100)$$

$$\frac{\rho_{i,j,k}^{n+1} - \rho_{i,j,k}^n}{\Delta t} + \nabla^+ \cdot \mathbf{J}_{i,j,k}^{n+1/2} = 0. \quad (2.101)$$

This means that, to get a complete description of the new electric and magnetic fields, it is sufficient to calculate only Eqs. (2.94) and (2.95), while Eqs. (2.92) and (2.93) can be considered as initial conditions. In such a case, however, the deposition of charge and current densities on the grid has to satisfy the discrete continuity equation [Eq. (2.101)].

The standard finite-difference time-domain method introduces a numerical dispersion in vacuum, the effect of which on the frequency ω and wavevector $\mathbf{k} = (k_x, k_y, k_z)$ of the electromagnetic wave can be described as follows [[Vay et al., 2011](#)],

$$\frac{1}{c^2 \Delta t^2} \sin^2 \left(\frac{\omega \Delta t}{2} \right) = \frac{1}{\Delta x^2} \sin^2 \left(\frac{k_x \Delta x}{2} \right) + \frac{1}{\Delta y^2} \sin^2 \left(\frac{k_y \Delta y}{2} \right) + \frac{1}{\Delta z^2} \sin^2 \left(\frac{k_z \Delta z}{2} \right). \quad (2.102)$$

According to Eq. (2.102), the electromagnetic waves may propagate in vacuum at velocities lower than c . Also, quasi-particles may travel faster than the electromagnetic waves and emit non-physical Cherenkov radiation [[Godfrey, 1974](#)], which is detrimental particularly when

modeling relativistic particle beams.

In general, the effects induced by the numerical dispersion can be mitigated by the use of a very high spatial resolution (at the cost of increased computational time). This is further complicated by the Courant–Friedrichs–Lewy condition [Courant et al., 1928], which ensures the numerical stability of the solver by preventing the electromagnetic waves to travel over a distance more than one grid cell in one time step,

$$\frac{C}{c^2 \Delta t^2} = \frac{1}{\Delta x^2} + \frac{1}{\Delta y^2} + \frac{1}{\Delta z^2}, \quad (2.103)$$

where $C \leq 1$. For the alternatives to the standard finite-difference time-domain method, the reader can refer to, e.g., Refs. Cole, 1997; Liu, 1997; Pukhov, 1999; Cowan et al., 2013; Lehe et al., 2013; Vay et al., 2013; Vincenti and Vay, 2016.

2.4.4 Field and particle weighting

In order to obtain the spatial averages of the electric, \mathbf{E}_p , and magnetic, \mathbf{B}_p , field components acting on quasi-particles, we may exploit the shape functions as in the following expressions,

$$\mathbf{E}_p = \sum_{i,j,k} \mathbf{E}_{i,j,k} S^r(\mathbf{r}_{i,j,k} - \mathbf{r}_p), \quad (2.104)$$

$$\mathbf{B}_p = \sum_{i,j,k} \mathbf{B}_{i,j,k} S^r(\mathbf{r}_{i,j,k} - \mathbf{r}_p). \quad (2.105)$$

This step represents the field weighting.

A final step that is yet to be discussed is thus the particle weighting, i.e., the deposition of the charge, $\rho(\mathbf{r}, t)$, and current, $\mathbf{J}(\mathbf{r}, t)$, densities from the quasi-particles to the grid points. According to the kinetic theory, $\rho(\mathbf{r}, t)$ and $\mathbf{J}(\mathbf{r}, t)$ can be obtained by the following integrals over the momentum space,

$$\rho(\mathbf{r}, t) = \sum_s q_s \int f_s(\mathbf{r}, \mathbf{p}, t) d\mathbf{p}, \quad (2.106)$$

$$\mathbf{J}(\mathbf{r}, t) = \sum_s q_s \int f_s(\mathbf{r}, \mathbf{p}, t) \mathbf{v} d\mathbf{p}. \quad (2.107)$$

After discretizing the expression of Eqs. (2.106) with quasi-particles and using the shape function properties, one gets

$$\rho_{i,j,k} = \sum_p q_p S^r(\mathbf{r}_{i,j,k} - \mathbf{r}_p), \quad (2.108)$$

where $q_p = q_s w_p$ is the charge of the quasi-particle.

One could assign the current densities to the grid points by the analogy to Eq. (2.108), but the discrete continuity equation [Eq. (2.101)] would be violated. To resolve this issue, one would have to calculate the Poisson equation [Eq. (2.92)] for the correction of the electric field at every simulation time step or use more sophisticated methods (referred to as the charge conservation methods) that satisfy the continuity equation exactly (see, e.g., Refs. Morse and Nielson, 1971; Eastwood, 1991; Villasenor and Buneman, 1992; Eastwood et al., 1995; Esirkepov, 2001; Umida et al., 2003).

Here we present the method of Esirkepov (see Ref. Esirkepov, 2001 for closer details),

which is valid for an arbitrary shape function. Due to the linearity of Eq. (2.101), the total current density deposited on the grid can be decomposed into the current densities associated with the motion of individual quasi-particles. Let us thus consider a single quasi-particle moving along a straight line from $\mathbf{r}_p = (x_p, y_p, z_p)$ to $\mathbf{r}_p + \delta\mathbf{r}_p$ over one time step, where $\delta\mathbf{r}_p = (\delta x_p, \delta y_p, \delta z_p)$ is a three-dimensional shift of the quasi-particle. Further, we define a vector $\mathbf{W} = (W_x, W_y, W_z)$ by the following equations,

$$(J_x)_{i+1,j,k} = (J_x)_{i,j,k} - q_p \frac{dx_p}{dt} (W_x)_{i,j,k}, \quad (2.109a)$$

$$(J_y)_{i,j+1,k} = (J_y)_{i,j,k} - q_p \frac{dy_p}{dt} (W_y)_{i,j,k}, \quad (2.109b)$$

$$(J_z)_{i,j,k+1} = (J_z)_{i,j,k} - q_p \frac{dz_p}{dt} (W_z)_{i,j,k}. \quad (2.109c)$$

According to Eq. (2.101) we may write

$$(W_x)_{i,j,k} + (W_y)_{i,j,k} + (W_z)_{i,j,k} = S^r(\mathbf{r}_{i,j,k} - \mathbf{r}_p - \delta\mathbf{r}_p) - S^r(\mathbf{r}_{i,j,k} - \mathbf{r}_p). \quad (2.109d)$$

The motion of the quasi-particle generates the following 8 functions,

$$\begin{aligned} & S^r(\mathbf{r}_{i,j,k} - \mathbf{r}_p), \quad S^r(\mathbf{r}_{i,j,k} - \mathbf{r}_p - \delta x_p \mathbf{e}_x), \quad S^r(\mathbf{r}_{i,j,k} - \mathbf{r}_p - \delta y_p \mathbf{e}_y), \\ & S^r(\mathbf{r}_{i,j,k} - \mathbf{r}_p - \delta z_p \mathbf{e}_z), \quad S^r(\mathbf{r}_{i,j,k} - \mathbf{r}_p - \delta x_p \mathbf{e}_x - \delta y_p \mathbf{e}_y), \\ & S^r(\mathbf{r}_{i,j,k} - \mathbf{r}_p - \delta x_p \mathbf{e}_x - \delta z_p \mathbf{e}_z), \quad S^r(\mathbf{r}_{i,j,k} - \mathbf{r}_p - \delta y_p \mathbf{e}_y - \delta z_p \mathbf{e}_z), \\ & S^r(\mathbf{r}_{i,j,k} - \mathbf{r}_p - \delta\mathbf{r}_p). \end{aligned} \quad (2.110)$$

According to Ref. Esirkepov, 2001, only one linear combination of the 8 functions, Eq. (2.110), satisfies the conditions imposed on \mathbf{W} ,

$$\begin{aligned} (W_x)_{i,j,k} &= \frac{1}{3}S^r(\mathbf{r}_{i,j,k} - \mathbf{r}_p - \delta\mathbf{r}_p) - \frac{1}{3}S^r(\mathbf{r}_{i,j,k} - \mathbf{r}_p - \delta y_p \mathbf{e}_y - \delta z_p \mathbf{e}_z) \\ &+ \frac{1}{6}S^r(\mathbf{r}_{i,j,k} - \mathbf{r}_p - \delta x_p \mathbf{e}_x - \delta z_p \mathbf{e}_z) - \frac{1}{6}S^r(\mathbf{r}_{i,j,k} - \mathbf{r}_p - \delta z_p \mathbf{e}_z) \\ &+ \frac{1}{6}S^r(\mathbf{r}_{i,j,k} - \mathbf{r}_p - \delta x_p \mathbf{e}_x - \delta y_p \mathbf{e}_y) - \frac{1}{6}S^r(\mathbf{r}_{i,j,k} - \mathbf{r}_p - \delta y_p \mathbf{e}_y) \\ &+ \frac{1}{3}S^r(\mathbf{r}_{i,j,k} - \mathbf{r}_p - \delta x_p \mathbf{e}_x) - \frac{1}{3}S^r(\mathbf{r}_{i,j,k} - \mathbf{r}_p), \end{aligned} \quad (2.111a)$$

$$\begin{aligned} (W_y)_{i,j,k} &= \frac{1}{3}S^r(\mathbf{r}_{i,j,k} - \mathbf{r}_p - \delta\mathbf{r}_p) - \frac{1}{3}S^r(\mathbf{r}_{i,j,k} - \mathbf{r}_p - \delta x_p \mathbf{e}_x - \delta z_p \mathbf{e}_z) \\ &+ \frac{1}{6}S^r(\mathbf{r}_{i,j,k} - \mathbf{r}_p - \delta y_p \mathbf{e}_y - \delta z_p \mathbf{e}_z) - \frac{1}{6}S^r(\mathbf{r}_{i,j,k} - \mathbf{r}_p - \delta z_p \mathbf{e}_z) \\ &+ \frac{1}{6}S^r(\mathbf{r}_{i,j,k} - \mathbf{r}_p - \delta x_p \mathbf{e}_x - \delta y_p \mathbf{e}_y) - \frac{1}{6}S^r(\mathbf{r}_{i,j,k} - \mathbf{r}_p - \delta x_p \mathbf{e}_x) \\ &+ \frac{1}{3}S^r(\mathbf{r}_{i,j,k} - \mathbf{r}_p - \delta y_p \mathbf{e}_y) - \frac{1}{3}S^r(\mathbf{r}_{i,j,k} - \mathbf{r}_p), \end{aligned} \quad (2.111b)$$

$$\begin{aligned}
 (W_z)_{i,j,k} = & \frac{1}{3} S^r (\mathbf{r}_{i,j,k} - \mathbf{r}_p - \boldsymbol{\delta}\mathbf{r}_p) - \frac{1}{3} S^r (\mathbf{r}_{i,j,k} - \mathbf{r}_p - \delta x_p \mathbf{e}_x - \delta y_p \mathbf{e}_y) \\
 & + \frac{1}{6} S^r (\mathbf{r}_{i,j,k} - \mathbf{r}_p - \delta y_p \mathbf{e}_y - \delta z_p \mathbf{e}_z) - \frac{1}{6} S^r (\mathbf{r}_{i,j,k} - \mathbf{r}_p - \delta y_p \mathbf{e}_y) \\
 & + \frac{1}{6} S^r (\mathbf{r}_{i,j,k} - \mathbf{r}_p - \delta x_p \mathbf{e}_x - \delta z_p \mathbf{e}_z) - \frac{1}{6} S^r (\mathbf{r}_{i,j,k} - \mathbf{r}_p - \delta x_p \mathbf{e}_x) \\
 & + \frac{1}{3} S^r (\mathbf{r}_{i,j,k} - \mathbf{r}_p - \delta z_p \mathbf{e}_z) - \frac{1}{3} S^r (\mathbf{r}_{i,j,k} - \mathbf{r}_p).
 \end{aligned} \tag{2.111c}$$

The expressions of Eqs. (2.111) define the current density decomposition. The current density associated with the motion of a single quasi-particle is obtained by solving Eqs. (2.109). We note that the charge conservation methods do not use the charge densities to advance the electromagnetic fields, they are usually projected on the grid only for diagnostics purposes.

“The science of today is the technology of tomorrow.”

– Edward Teller (1908 – 2003)

3

Author’s original results

In this chapter, the reader can find an overview of the main results achieved within the author’s postgraduate studies; in total, we select four papers published in peer-reviewed journals, Refs. I. – IV., which are fully (or from the most part) based on the author’s original work. Below, we provide a brief summary of each selected paper as well as a detailed description of the author’s role and contributions. Full texts of all the selected publications are enclosed with permission in Appendix B.

3.1 On the electromagnetic-electron rings

First, we present the results of research devoted to the coupled electromagnetic and electron rings originating from the interaction of high-power short-pulse laser and underdense plasma, which have been published in Ref. I. (the reader can find the full text of the paper in Appendix B.1). This research has been initiated after the experimental observation of stable and tunable ring-shaped beams of high-energy electrons; the experiment has been carried out by the ELI Beamlines Electron Acceleration Group at the Institute of Plasma Physics and Laser Microfusion in Warsaw, Poland (the reader can find further details in Ref. Grittani, 2018). Our preliminary goal was to find out and describe the underlying physical mechanisms which lead to the formation of ring-shaped electron beams in laser plasmas. Although several processes that may result in the electron rings of similar parameters were already identified and presented in literature at that time (see, e.g., Refs. Kaganovich et al., 2008; Zhang et al., 2012; Pollock et al., 2015; Zhao et al., 2016; Yang et al., 2017; Behm et al., 2019; Salehi et al., 2021), none of them seemed to correspond to the particular experimental parameters used in Ref. Grittani, 2018.

In general, this work investigates (analytically and using numerical simulations) the propagation of high-power short-pulse laser in a low-density plasma, which is a topic relevant to a number of scientific challenges, such as laser-driven acceleration of charged particles [Tajima and Dawson, 1979; Esarey et al., 2009; Gonsalves et al., 2019], development of sources of hard electromagnetic radiation [Pirozhkov et al., 2012; Bulanov et al., 2013], and nuclear fusion within the framework of the fast ignition concept [Tabak et al., 1994]. For most of these applications, it is essential that the laser pulse propagates over extended distances and

transmits its energy into the plasma in controlled way without incurring excessive losses. In this context, much of the attention has been focused on the evolution of the radial profile of the laser beam in a fully ionized plasma; it turned out that the process of self-focusing for high-power laser pulses may lead to the formation of the multifilament and, in particular, ring-shaped transverse structures [Mori et al., 1988; Cohen et al., 1991; Borisov et al., 1992; Krushelnick et al., 1997; Cattani et al., 2001; Kim et al., 2002; Naseri et al., 2016; Kovalev and Bychenkov, 2019]. We show that these electromagnetic rings can become a source of high-energy ring-shaped electron beams.

In addition to the applications mentioned above, the understanding of the physical processes that lead to the generation of the electromagnetic and electron ring structures is important due to the following reasons: (i) the electromagnetic rings may carry off a significant fraction of energy from the driver, and thus limit the overall efficiency of applications based on the laser-plasma interaction; (ii) the electron beams accelerated in the wake of the electromagnetic rings may cause a damage to surrounding equipment (e.g., capillaries used for the laser pulse guiding) and become a source of unwanted electromagnetic radiation; and (iii) the knowledge of the origin of the electromagnetic and electron rings could serve as a diagnostics for determining the regimes of laser-plasma interaction.

The first part of the paper presents an analytical model based on geometric optics approximation which qualitatively illustrates the origin and the initial stage of the electromagnetic ring formation. We define the plasma density distribution within the Langmuir wave as well as the Hamiltonian for the photon interaction with the Langmuir wave; the trajectories of photons are then obtained by solving the Hamilton equations. The second part of the paper presents a three-dimensional particle-in-cell simulation, the results of which demonstrate the formation of the electromagnetic as well as electron ring. We discuss the mechanism of formation of the electromagnetic ring and the processes of electron injection into the accelerating phase of the secondary wakefield generated by the electromagnetic ring. Finally, the third part of the paper contains the results of a systematic multi-parametric simulation study for various plasma densities, laser intensities, and laser spot sizes revealing the relationships among the properties of the electromagnetic rings and the parameters of laser and plasma.

The main results of the paper can be summarized as follows. We identify and describe a novel physical mechanism which leads to the formation of ring-shaped electromagnetic-electron structures, where the electromagnetic rings arise from the laser pulse defocusing induced by the excitation of Langmuir waves in underdense plasma, and the ring-shaped electron beams are formed and accelerated subsequently by the secondary toroidal wakefields generated by the electromagnetic rings. We further reveal that the electromagnetic rings are relatively robust nonlinear objects, whose properties can be controlled by tuning the parameters of laser and plasma. Within the studied parameter range, we find that up to $\approx 70\%$ of the total initial driver pulse energy can be carried off by the electromagnetic rings having the opening angles $\approx 45 - 115$ mrad.

Our research published in Ref. I. has been promoted by the editors of Physics of Plasmas journal by selecting the article as “Featured” and additionally reported by Scilight, which showcases the most interesting research across the physical sciences published in AIP Publishing journals. Furthermore, Fig. 4 from Ref. I. has been selected as the cover image of the journal’s December issue. Besides Ref. I., a portion of this work has been also published in Ref. [Valenta SPIE 2021] and presented by the author at “SPIE Optics+Optoelectronics 2021,” “OPTO2021 Symposium on Photon and Beam Science,” and “ELI Summer School 2021,” whereas the latter presentation has been awarded by the “Best poster prize.” The author contributed to all the aspects of the research, including the initial formulation of the scientific topic, development of the analytical model, setup and execution of the numerical simulations

on computer clusters, and analysis and interpretation of the simulation data. Furthermore, based on the results obtained the author prepared figures, wrote the bulk of the manuscript text, and submitted the manuscript to the journal whereas serving as a corresponding author. Last, the author was communicating with editors and referees concerning the requested revisions of the manuscript until the final publication in the journal.

3.2 On the laser-wakefield polarity reversal

Second, we present the results of research devoted to the laser-wakefield acceleration of electrons in the regime of ultrashort pulses and near-critical density plasmas, which have been published in Ref. II. (the reader can find the full text of the paper in Appendix B.2). This research is closely related to the laser-wakefield acceleration of electrons driven by high-repetition-rate (\gtrsim kHz) laser systems (such as the L1 laser system at ELI Beamlines).

The research on laser-wakefield acceleration of electrons has been predominantly oriented on high-energy laser systems. Recently, however, there has been also a growing interest in the laser-wakefield acceleration driven by high-repetition-rate (\gtrsim kHz) laser systems since they can significantly improve certain characteristics (e.g., stability, signal-to-noise ratio, average electron current [Faure et al., 2019]) required by a number of practical applications (e.g., ultrafast electron diffraction [Sciaini and Miller, 2011; Miller, 2014], fs x-ray generation [Ta Phuoc et al., 2012; Corde et al., 2013], and pulsed radiolysis [Muroya et al., 2008]). On the other hand, present-day high-repetition-rate lasers deliver (due to the constraints in technology) pulses with energy of only a few mJ. This (together with the requirements of the blow-out regime of the laser-wakefield acceleration) implies that, in order to produce high-quality relativistic electron sources, one has to use tightly-focused near-single-cycle pulses and thin near-critical density gas targets [Faure et al., 2019; Salehi et al., 2019]. Such considerations constitute a great challenge not only from a technical point of view, but also in the sense of the understanding of underlying physical processes (e.g., related to the λ^3 regime [Mourou et al., 2002; Naumova et al., 2004]).

In the first part of the paper we extend the standard model of the wakefield generation by considering the carrier-envelope phase shift of the driving laser pulse. The model shows that wakefield generated by the ultrashort laser pulse contains a long-wavelength modulation of its amplitude. In the second part of the paper we analytically investigate the acceleration of single relativistic electron by the modulated wakefield. We show that the electron energy gain depends on the initial phase of the driver and find the case for which the net energy acquired by the electron over given distance is maximal. Finally, the third part of the paper contains the description of setup and the results of the three-dimensional particle-in-cell simulation on the self-consistent evolution of the ultrashort laser pulse and near-critical density plasma. The simulation results are in qualitative agreement with the analytical model.

The main results of the paper can be summarized as follows. We reveal for the first time (to the best of our knowledge) that the wakefield, being excited by an ultrashort laser pulse in plasma, periodically reverses its polarity. As shown by the analytical model and numerical simulation, the wakefield polarity reversal is caused by dispersion and the corresponding difference between the propagation speed of the carrier and the envelope of the driving laser pulse. Further, we show that the novel phenomenon of the wakefield polarity reversal occurs on spatial scales shorter than the dephasing length and, therefore, significantly affects the energy spectra of accelerated electron beams. In the nonlinear regime, however, there may exist a case for which the polarity reversal length is equal to the dephasing length. In such a case, the dephasing limit is overcome and the electrons are accelerated until the

energy of the driver pulse depletes. The discovery of this phenomenon is crucial for better control of the parameters of electron beams accelerated via the laser-wakefield mechanism (e.g., by adjusting the initial phase of the driver or by controlling the phase of the electron injection), particularly in experiments carried out with the present-day high-repetition-rate laser systems.

Besides Ref. II., a portion of this work has been also published in Refs. [Lazzarini + book, Valenta SPIE 2019, Valenta EPS 2018] and presented by the author at “ELI Users’ conference 2020,” “SPIE Optics+Optoelectronics 2019,” and “45th EPS Conference on Plasma Physics,” whereas the latter presentation has been awarded by the “Best poster prize.” The author contributed to all the aspects of the research, including the initial formulation of the scientific topic, development of the analytical model, setup and execution of the numerical simulations on computer clusters, and analysis and interpretation of the simulation data. Furthermore, based on the results obtained the author prepared figures and wrote the bulk of the manuscript text, submitted the manuscript to the journal whereas serving as a corresponding author. Last, the author was communicating with editors and referees concerning the requested revisions of the manuscript until the final publication in the journal.

3.3 On the recoil effects of relativistic mirrors

Third, we present the results of research devoted to the sources of coherent short-wavelength radiation based on the concept of relativistic flying mirrors in plasma, which have been published in Ref. III. (the reader can find the full text of the paper in Appendix B.3). Maximization of the energy of radiation reflected from the relativistic mirror requires a more intense incident electromagnetic wave. However, sufficiently strong incident light can significantly affect the motion of the relativistic mirror (i.e., its radiation pressure can stop or destroy the mirror). This work investigates (analytically and using numerical simulations) the recoil effects associated with the interaction of relativistic mirrors and strong counter-propagating electromagnetic waves as well as the corresponding changes in the properties of reflected radiation. The considered topic is important for the question of the feasibility of relativistic mirrors for various purposes.

In the first part of the paper we exploit the conservation of momentum and energy before and after the interaction of relativistic flying mirror with counter-propagating electromagnetic wave to develop an analytical model describing the factors of amplification and frequency upshift of the relativistic mirror beyond the approximation of a weak incident electromagnetic wave. Furthermore, we define a threshold for the fluence of the incident electromagnetic wave which characterizes the recoil importance in this interaction. In the second part of the paper, we consider a relativistic flying mirror in the form of strongly nonlinear Langmuir wave and estimate the threshold derived before for this particular case of physical realization of relativistic mirror. Finally, in the third part of the paper we investigate the applicability of our model by one-dimensional particle-in-cell simulations and numerically obtain the properties of interest, such as reflection coefficient of the Langmuir wave and factors of the electric field amplification and the frequency upshift of the incident laser pulse.

The main results of the paper can be summarized as follows. We present an analytical model which shows that if the fluence of the electromagnetic wave incident on the relativistic mirror exceeds a certain threshold, the relativistic mirror undergoes a back reaction significantly affecting its amplification and frequency upshift factors. Further, the numerical simulations reveal that the Langmuir wave driven by a short intense laser pulse in uniform plasma decelerates and, therefore, the reflected radiation has a positive chirp. We find that

the electric field amplification factor of the reflected radiation reaches its maximum at the moment of wave-breaking. In addition, our results show that for a given intensity of the source pulse there exists an optimal duration of the source pulse; longer-than-optimal pulses have lower reflected-to-incident energy ratio. Moreover, for a given Langmuir wave excited by the driver pulse there exists an optimal intensity of the source pulse which provides the most intense reflected wave with almost the same frequency upshift factor as in the weak-source approximation.

Besides Ref. III., a portion of this work has been also published in Refs. [Valenta OSA 2020, Jeong ICXRL 2020] and presented by the author at “OSA High-brightness Sources and Light-driven Interactions Congress 2020,” “ELI Summer School 2020,” “LeCosPA Cosmology and Particle Astrophysics Seminar,” “4th Users’ Conference of IT4Innovations,” and “28th Symposium on Plasma Physics and Technology.” The author contributed to all the aspects of the research, including the initial formulation of the scientific topic, development of the analytical model, setup and execution of the numerical simulations on computer clusters (requiring significant changes to the source code in this case), and analysis and interpretation of the simulation data. Furthermore, based on the results obtained the author prepared figures, wrote the bulk of the manuscript text, and submitted the manuscript to the journal whereas serving as a corresponding author. Last, the author was communicating with editors and referees concerning the requested revisions of the manuscript until the final publication in the journal.

3.4 On the relativistic flying forcibly oscillating mirror

The last selected research topic introduces a novel scheme for physical realization of relativistic flying mirrors based on the density singularities in laser plasmas; its results have been published in Ref. IV. (the reader can find the full text of the paper in Appendix B.4). In this scheme, the mirror surface is realized by electron density singularities that emerge near the joining area of the wake wave cavity and the bow wave; the mirror moves together with the driving laser pulse and undergoes forced oscillations induced by the driver field. Besides the source pulse base frequency, the spectrum of the reflected light thus contains also its harmonics, all multiplied by a large factor due to the double Doppler effect, which is one of the main advantages of this novel scheme. Furthermore, a counter-propagating laser pulse is incident on the mirror surface at grazing angles, which significantly improves the reflection efficiency.

Apart from the applications mentioned in Sec. 3.3, the scheme described in Ref. IV. provides an additional tool in laser-plasma diagnostics, helping to analyze the dynamics of nonlinear physical processes in relativistic plasmas. The peculiar spectrum of the reflected radiation in this scheme, using the head-on collision of the driver and source, substantially extends the capabilities for probing relativistic plasma singularities by a transverse source pulse, as suggested in Ref. Esirkepov et al., 2020. Using a weak and short laser pulse as a probe, one can deduce or characterize the parameters of the laser-plasma interaction, including the geometrical properties of the first period of the plasma wave (wake wave cavity and bow wave), driver pulse frequency and magnitude at the location of the mirror, the phase velocity of the wake wave, the electron temperature and momentum distribution at the location of the mirror, etc.

One of the immediate applications of such a diagnostic is control and tuning of the burst intensification by singularity emitting radiation (BISER) [Pirozhkov et al., 2012; Pirozhkov et al., 2014; Pirozhkov et al., 2017; Sagisaka et al., 2020], which occurs with the same

parameters for the driver laser and plasma as required by the described scheme, so that off-axis radiation from the mirror can be observed simultaneously with near- or on-axis BISER. In addition to the fundamental physics concerning intense laser-plasma interactions, plasma diagnostics with the described scheme may help to substantially improve the quality of the laser pulse by revealing what laser parameters are the most critical. Such investigations, in the example of the laser pulse quality effects on the BISER realization, were conducted recently [Pirozhkov et al., 2018]. That work revealed some critical parameters of the laser pulse which must be improved to obtain good results and scalings predicted by theory. Last but not least, optical probing of relativistic plasma singularities could reveal a phenomenon similar to the Lampa-Penrose-Terrell effect [Lampa, 1924; Penrose, 1959; Terrell, 1959], i.e., the image of the constellation of density singularities in plasma would be such as if the singularities were slightly rotated with respect to each other (for closer details see Ref. Esirkepov et al., 2020).

In the first part of the paper we describe the physical mechanisms underlying the formation of the electron density singularities in laser plasmas and propose a novel scheme in which these singularities act as a relativistic mirror. Furthermore, we develop an analytical model in order to predict the base frequency and direction angle of reflected radiation. In the second part of the paper we present a setup and results of three-dimensional and high-resolution two-dimensional particle-in-cell simulations. We demonstrate the feasibility of the novel scheme and analyze the properties of the reflected electromagnetic wave and its spectrum. Finally, in the third part of the paper we investigate the effects of finite temperature on the proposed scheme.

The main results of the paper can be summarized as follows. We propose a novel scheme for physical realization of relativistic mirrors based on the density singularities in laser plasmas - a relativistic flying forcibly oscillating mirror. The proposed scheme uses the electron density singularity at the joining area of the laser wake and bow waves to reflect the counter-propagating source pulse. Since in this regime the surface of the mirror is modulated and oscillates due to the presence of the strong electromagnetic field of the driving laser pulse, it acts as a reflective diffraction grating and generates boosted high-order harmonics of very high brightness. Compared with the boosted high-order harmonics produced by a high-density plasma slab and a thin electron layer [Kulagin et al., 2007a; Esirkepov et al., 2009; Wu et al., 2010], the regime under consideration has the properties of a relativistic flying mirror [Bulanov et al., 2003], relativistic oscillating mirror [Bulanov et al., 1994; Naumova et al., 2004], and it inherits the properties of the laser driven oscillating electron spikes [Pirozhkov et al., 2014; Pirozhkov et al., 2017].

Besides Ref. IV., a portion of this work has been also published in Refs. Esirkepov et al., 2020[Mu SPIE 2019, Mu Phys. Wave. Phen. 2019] and presented by the author at “SPIE Optics & Photonics International Congress 2019,” “KPSI Scientific Seminar,” and “2nd Users’ Conference of IT4Innovations.” The author contributed mainly to the setup and execution of three-dimensional numerical simulations on computer clusters and subsequent analysis and interpretation of the simulation data. Based on the results obtained the author prepared figures and wrote the bulk of the manuscript text corresponding to the part dealing with the numerical simulations. Last, the author also contributed concerning the requested revisions of the manuscript until the final publication in the journal.

“The best is the enemy of the good.”

– Voltaire (1694 – 1778)

4

Conclusion

4.1 Summary

4.2 Future research and perspectives

Acknowledgements

Bibliography

- [Akhiezer and Polovin, 1956] Akhiezer, A. and Polovin, R. (1956). Theory of wave motion of an electron plasma. *Soviet Physics - JETP*, **3**(5):696–704.
- [Armstrong et al., 1962] Armstrong, J. A., Bloembergen, N., Ducuing, J., and Pershan, P. S. (1962). **Interactions between light waves in a nonlinear dielectric**. *Physical Review*, **127**(6):1918–1939.
- [Bahk et al., 2004] Bahk, S. W., Rousseau, P., Planchon, T. A., Chvykov, V., Kalintchenko, G., Maksimchuk, A., Mourou, G. A., and Yanovsky, V. (2004). **Generation and characterization of the highest laser intensities (10^{22} W/cm²)**. *Optics Letters*, **29**(24):2837.
- [Bass et al., 1962] Bass, M., Franken, P. A., Ward, J. F., and Weinreich, G. (1962). **Optical rectification**. *Physical Review Letters*, **9**(11):446–448.
- [Baumgartner and Byer, 1979] Baumgartner, R. A. and Byer, R. K. (1979). **Optical parametric amplification**. *IEEE Journal of Quantum Electronics*, **15**(6):432–444.
- [Behm et al., 2019] Behm, K., Hussein, A., Zhao, T. Z., Dann, S., Hou, B. X., Yanovsky, V., Nees, J., Maksimchuk, A., Schumaker, W., Thomas, A. G., and Krushelnick, K. (2019). **Measurements of electron beam ring structures from laser wakefield accelerators**. *Plasma Physics and Controlled Fusion*, **61**(6):65012.
- [Berezhiani and Murusidze, 1990] Berezhiani, V. I. and Murusidze, I. G. (1990). **Relativistic wake-field generation by an intense laser pulse in a plasma**. *Physics Letters A*, **148**(6-7):338–340.
- [Birdsall and Langdon, 2004] Birdsall, C. K. and Langdon, A. B. (2004). *Plasma Physics via Computer Simulation*. Taylor and Francis, New York.
- [Boris, 1971] Boris, J. P. (1971). Relativistic plasma simulation - Optimization of a hybrid code. In *Proceedings of the Fourth Conference on Numerical Simulation of Plasmas*, pages 3–67. Office of Naval Research, Arlington, Va.
- [Borisov et al., 1992] Borisov, A. B., Borovskiy, A. V., Shiryaev, O. B., Korobkin, V. V., Prokhorov, A. M., Solem, J. C., Luk, T. S., Boyer, K., and Rhodes, C. K. (1992). **Relativistic and charge-displacement self-channeling of intense ultrashort laser pulses in plasmas**. *Physical Review A*, **45**(8):5830–5845.
- [Budriūnas et al., 2017] Budriūnas, R., Stanislauskas, T., Adamonis, J., Aleknavičius, A., Veitas, G., Gadonas, D., Balickas, S., Michailovas, A., and Varanavičius, A. (2017). **53 W average power CEP-stabilized OPCPA system delivering 55 TW few cycle pulses at 1 kHz repetition rate**. *Optics Express*, **25**(5):5797.

Bibliography

- [Bulanov et al., 1989] Bulanov, S., Kirsanov, V., and Sakharov, A. (1989). Excitation of ultrarelativistic plasma waves by pulse of electromagnetic radiation. *JETP letters*, **50**(4):176–178.
- [Bulanov et al., 2010] Bulanov, S. S., Mur, V. D., Narozhny, N. B., Nees, J., and Popov, V. S. (2010). [Multiple colliding electromagnetic pulses: A way to lower the threshold of \$e^+e^-\$ pair production from vacuum](#). *Physical Review Letters*, **104**(22):220404.
- [Bulanov, 2021] Bulanov, S. V. (2021). [Electron dynamics in the field of strong plasma and electromagnetic waves: A review](#). *Physics of Wave Phenomena*, **29**(1):1–46.
- [Bulanov et al., 2011] Bulanov, S. V., Esirkepov, T. Z., Hayashi, Y., Kando, M., Kiriyama, H., Koga, J. K., Kondo, K., Kotaki, H., Pirozhkov, A. S., Bulanov, S. S., Zhidkov, A. G., Chen, P., Neely, D., Kato, Y., Narozhny, N. B., and Korn, G. (2011). [On the design of experiments for the study of extreme field limits in the interaction of laser with ultrarelativistic electron beam](#). *Nuclear Instruments and Methods in Physics Research A*, **660**(1):31–42.
- [Bulanov et al., 2016a] Bulanov, S. V., Esirkepov, T. Z., Hayashi, Y., Kiriyama, H., Koga, J. K., Kotaki, H., Mori, M., and Kando, M. (2016). [On some theoretical problems of laser wake-field accelerators](#). *Journal of Plasma Physics*, **82**(3):905820308.
- [Bulanov et al., 2016b] Bulanov, S. V., Esirkepov, T. Z., Kando, M., and Koga, J. (2016). [Relativistic mirrors in laser plasmas \(analytical methods\)](#). *Plasma Sources Science and Technology*, **25**(5):53001.
- [Bulanov et al., 2013] Bulanov, S. V., Esirkepov, T. Z., Kando, M., Pirozhkov, A. S., and Rosanov, N. N. (2013). [Relativistic mirrors in plasmas. Novel results and perspectives](#). *Physics-Uspekhi*, **56**(5):429–464.
- [Bulanov et al., 2002] Bulanov, S. V., Esirkepov, T. Z., Khoroshkov, V. S., Kuznetsov, A. V., and Pegoraro, F. (2002). [Oncological hadrontherapy with laser ion accelerators](#). *Physics Letters A*, **299**(2-3):240–247.
- [Bulanov et al., 2003] Bulanov, S. V., Esirkepov, T. Z., and Tajima, T. (2003). [Light intensification towards the Schwinger limit](#). *Physical Review Letters*, **91**(8):85001.
- [Bulanov et al., 1994] Bulanov, S. V., Naumova, N. M., and Pegoraro, F. (1994). [Interaction of an ultrashort, relativistically strong laser pulse with an overdense plasma](#). *Physics of Plasmas*, **1**(3):745–757.
- [Bulanov et al., 1995] Bulanov, S. V., Pegoraro, F., and Pukhov, A. M. (1995). [Two-dimensional regimes of self-focusing, wake field generation, and induced focusing of a short intense laser pulse in an underdense plasma](#). *Physical Review Letters*, **74**(5):710–713.
- [Bulanov and Sakharov, 1991] Bulanov, S. V. and Sakharov, A. S. (1991). Induced focusing of electromagnetic wave in a wake plasma wave. *JETP Letters*, **54**(4):203–207.
- [Byer, 1988] Byer, R. L. (1988). [Diode laser-pumped solid-state lasers](#). *Science*, **239**(4841):742–747.
- [Cattani et al., 2001] Cattani, F., Kim, A., Anderson, D., and Lisak, M. (2001). [Multifilament structures in relativistic self-focusing](#). *Physical Review E*, **64**(1):8.
- [Chen and Mourou, 2017] Chen, P. and Mourou, G. (2017). [Accelerating plasma mirrors to investigate the black hole information loss paradox](#). *Physical Review Letters*, **118**(4):45001.

- [Chen and Mourou, 2020] Chen, P. and Mourou, G. (2020). [Trajectory of a flying plasma mirror traversing a target with density gradient](#). *Physics of Plasmas*, **27**(12):123106.
- [Chiao et al., 1964a] Chiao, R. Y., Garmire, E., and Townes, C. H. (1964). [Self-trapping of optical beams](#). *Physical Review Letters*, **13**(15):479–482.
- [Chiao et al., 1964b] Chiao, R. Y., Townes, C. H., and Stoicheff, B. P. (1964). [Stimulated Brillouin scattering and coherent generation of intense hypersonic waves](#). *Physical Review Letters*, **12**(21):592–595.
- [Cohen et al., 1991] Cohen, B. I., Lasinski, B. F., Langdon, A. B., and Cummings, J. C. (1991). [Dynamics of ponderomotive self-focusing in plasmas](#). *Physics of Fluids B*, **3**(3):766–775.
- [Cole, 1997] Cole, J. B. (1997). [A high-accuracy realization of the Yee algorithm using non-standard finite differences](#). *IEEE Transactions on Microwave Theory and Techniques*, **45**(6):991–996.
- [Corde et al., 2013] Corde, S., Ta Phuoc, K., Lambert, G., Fitour, R., Malka, V., Rousse, A., Beck, A., and Lefebvre, E. (2013). [Femtosecond x rays from laser-plasma accelerators](#). *Reviews of Modern Physics*, **85**(1):1–48.
- [Couperus et al., 2017] Couperus, J. P., Pausch, R., Köhler, A., Zarini, O., Krämer, J. M., Garten, M., Huebl, A., Gebhardt, R., Helbig, U., Bock, S., Zeil, K., Debus, A., Bussmann, M., Schramm, U., and Irman, A. (2017). [Demonstration of a beam loaded nanocoulomb-class laser wakefield accelerator](#). *Nature Communications*, **8**(1):487.
- [Courant et al., 1928] Courant, R., Friedrichs, K., and Lewy, H. (1928). [Über die partiellen Differenzengleichungen der mathematischen Physik](#). *Mathematische Annalen*, **100**(1):32–74.
- [Cowan et al., 2013] Cowan, B. M., Bruhwiler, D. L., Cary, J. R., Cormier-Michel, E., and Geddes, C. G. (2013). [Generalized algorithm for control of numerical dispersion in explicit time-domain electromagnetic simulations](#). *Physical Review Special Topics - Accelerators and Beams*, **16**(4):41303.
- [Danson et al., 2019] Danson, C. N., Haefner, C., Bromage, J., Butcher, T., Chanteloup, J. C. F., Chowdhury, E. A., Galvanauskas, A., Gizzi, L. A., Hein, J., Hillier, D. I., Hopps, N. W., Kato, Y., Khazanov, E. A., Kodama, R., Korn, G., Li, R., Li, Y., Limpert, J., Ma, J., Nam, C. H., Neely, D., Papadopoulos, D., Penman, R. R., Qian, L., Rocca, J. J., Shaykin, A. A., Siders, C. W., Spindloe, C., Szatmári, S., Trines, R. M., Zhu, J., Zhu, P., and Zuegel, J. D. (2019). [Petawatt and exawatt class lasers worldwide](#). *High Power Laser Science and Engineering*, **7**:e54.
- [Dawson, 1959] Dawson, J. M. (1959). [Nonlinear electron oscillations in a cold plasma](#). *Physical Review*, **113**(2):383–387.
- [Dawson, 1983] Dawson, J. M. (1983). [Particle simulation of plasmas](#). *Reviews of Modern Physics*, **55**(2):403–447.
- [Debus et al., 2010] Debus, A. D., Bussmann, M., Schramm, U., Sauerbrey, R., Murphy, C. D., Major, Z., Hörlein, R., Veisz, L., Schmid, K., Schreiber, J., Witte, K., Jamison, S. P., Gallacher, J. G., Jaroszynski, D. A., Kaluza, M. C., Hidding, B., Kiselev, S., Heathcote, R.,

Bibliography

- Foster, P. S., Neely, D., Divall, E. J., Hooker, C. J., Smith, J. M., Ertel, K., Langley, A. J., Norreys, P., Collier, J. L., and Karsch, S. (2010). [Electron bunch length measurements from laser-accelerated electrons using single-shot THz time-domain interferometry](#). *Physical Review Letters*, **104**(8):84802.
- [DesRosiers et al., 2000] DesRosiers, C., Moskvin, V., Bielajew, A. F., and Papiez, L. (2000). [150-250 MeV electron beams in radiation therapy](#). *Physics in Medicine and Biology*, **45**(7):1781–1805.
- [Dubietis et al., 1992] Dubietis, A., Jonušauskas, G., and Piskarskas, A. (1992). [Powerful femtosecond pulse generation by chirped and stretched pulse parametric amplification in BBO crystal](#). *Optics Communications*, **88**(4-6):437–440.
- [Eastwood, 1991] Eastwood, J. W. (1991). [The virtual particle electromagnetic particle-mesh method](#). *Computer Physics Communications*, **64**(2):252–266.
- [Eastwood et al., 1995] Eastwood, J. W., Arter, W., Brealey, N. J., and Hockney, R. W. (1995). [Body-fitted electromagnetic PIC software for use on parallel computers](#). *Computer Physics Communications*, **87**(1-2):155–178.
- [Einstein, 1905] Einstein, A. (1905). [Zur Elektrodynamik bewegter Körper](#). *Annalen der Physik*, **322**(10):891–921.
- [Esarey et al., 2009] Esarey, E., Schroeder, C. B., and Leemans, W. P. (2009). [Physics of laser-driven plasma-based electron accelerators](#). *Reviews of Modern Physics*, **81**(3):1229–1285.
- [Esarey et al., 1996] Esarey, E., Sprangle, P., Krall, J., and Ting, A. (1996). [Overview of plasma-based accelerator concepts](#). *IEEE Transactions on Plasma Science*, **24**(2):252–288.
- [Esirkepov et al., 2006] Esirkepov, T., Bulanov, S. V., Yamagiwa, M., and Tajima, T. (2006). [Electron, positron, and photon wakefield acceleration: Trapping, wake overtaking, and ponderomotive acceleration](#). *Physical Review Letters*, **96**(1):14803.
- [Esirkepov, 2001] Esirkepov, T. Z. (2001). [Exact charge conservation scheme for particle-in-cell simulation with an arbitrary form-factor](#). *Computer Physics Communications*, **135**(2):144–153.
- [Esirkepov et al., 2009] Esirkepov, T. Z., Bulanov, S. V., Kando, M., Pirozhkov, A. S., and Zhidkov, A. G. (2009). [Boosted high-harmonics pulse from a double-sided relativistic mirror](#). *Physical Review Letters*, **103**(2):25002.
- [Esirkepov et al., 2020] Esirkepov, T. Z., Mu, J., Gu, Y., Jeong, T. M., Valenta, P., Klimo, O., Koga, J. K., Kando, M., Neely, D., Korn, G., Bulanov, S. V., and Pirozhkov, A. S. (2020). [Optical probing of relativistic plasma singularities](#). *Physics of Plasmas*, **27**(5):052103.
- [Farina and Bulanov, 2001] Farina, D. and Bulanov, S. V. (2001). [Relativistic electromagnetic solitons in the electron-ion plasma](#). *Physical Review Letters*, **86**(23):5289–5292.
- [Faure et al., 2004] Faure, J., Glinec, Y., Pukhov, A., Klselev, S., Gordienko, S., Lefebvre, E., Rousseau, J. P., Burgy, F., and Malka, V. (2004). [A laser-plasma accelerator producing monoenergetic electron beams](#). *Nature*, **431**(7008):541–544.

- [Faure et al., 2019] Faure, J., Gustas, D., Guénot, D., Vernier, A., Böhle, F., Ouillé, M., Haessler, S., Lopez-Martens, R., and Lifschitz, A. (2019). [A review of recent progress on laser-plasma acceleration at kHz repetition rate](#). *Plasma Physics and Controlled Fusion*, **61**(1):14012.
- [Franken et al., 1961] Franken, P. A., Hill, A. E., Peters, C. W., and Weinreich, G. (1961). [Generation of optical harmonics](#). *Physical Review Letters*, **7**(4):118–119.
- [Gauduel et al., 2010] Gauduel, Y. A., Glinec, Y., Rousseau, J. P., Burg, F., and Malka, V. (2010). [High energy radiation femtochemistry of water molecules: Early electron-radical pairs processes](#). *European Physical Journal D*, **60**(1):121–135.
- [Geddes et al., 2004] Geddes, C. G., Toth, C., Van Tilborg, J., Esarey, E., Schroeder, C. B., Bruhwiler, D., Nieter, C., Cary, J., and Leemans, W. P. (2004). [High-quality electron beams from a laser wakefield accelerator using plasma-channel guiding](#). *Nature*, **431**(7008):538–541.
- [Giordmaine and Miller, 1965] Giordmaine, J. A. and Miller, R. C. (1965). [Tunable coherent parametric oscillation in LiNbO₃ at optical frequencies](#). *Physical Review Letters*, **14**(24):973–976.
- [Glinec et al., 2005] Glinec, Y., Faure, J., Le Dain, L., Darbon, S., Hosokai, T., Santos, J. J., Lefebvre, E., Rousseau, J. P., Burg, F., Mercier, B., and Malka, V. (2005). [High-resolution \$\gamma\$ -ray radiography produced by a laser-plasma driven electron source](#). *Physical Review Letters*, **94**(2):25003.
- [Godfrey, 1974] Godfrey, B. B. (1974). [Numerical Cherenkov instabilities in electromagnetic particle codes](#). *Journal of Computational Physics*, **15**(4):504–521.
- [Gonoskov et al., 2012] Gonoskov, I., Aiello, A., Heugel, S., and Leuchs, G. (2012). [Dipole pulse theory: Maximizing the field amplitude from \$4\pi\$ focused laser pulses](#). *Physical Review A*, **86**(5):53836.
- [Gonsalves et al., 2019] Gonsalves, A. J., Nakamura, K., Daniels, J., Benedetti, C., Pieronek, C., De Raadt, T. C., Steinke, S., Bin, J. H., Bulanov, S. S., Van Tilborg, J., Geddes, C. G., Schroeder, C. B., Tóth, C., Esarey, E., Swanson, K., Fan-Chiang, L., Bagdasarov, G., Bobrova, N., Gasilov, V., Korn, G., Sasorov, P., and Leemans, W. P. (2019). [Petawatt laser guiding and electron beam acceleration to 8 GeV in a laser-heated capillary discharge waveguide](#). *Physical Review Letters*, **122**(8):84801.
- [Gradshteyn and Ryzhik, 1980] Gradshteyn, I. S. and Ryzhik, I. M. (1980). *Table of integrals, series, and products*. Academic Press.
- [Grigoryev et al., 2002] Grigoryev, Y. N., Vshivkov, V. A., and Fedoruk, M. P. (2002). *Numerical "Particle-in-cell" Methods: Theory and Applications*. De Gruyter, Utrecht.
- [Grittani, 2018] Grittani, G. M. (2018). *Experimental study of laser-wakefield acceleration and applications of laser-accelerated electron beams in the ELI Beamlines project*. Doctoral thesis, Czech Technical University in Prague.
- [Haefner et al., 2017] Haefner, C. L., Bayramian, A., Betts, S., Bopp, R., Buck, S., Cupal, J., Drouin, M., Erlandson, A., Horáček, J., Horner, J., Jarboe, J., Kasl, K., Kim, D., Koh, E., Koubíková, L., Maranville, W., Marshall, C., Mason, D., Menapace, J., Miller,

Bibliography

- P., Mazurek, P., Naylor, A., Novák, J., Peceli, D., Rosso, P., Schaffers, K., Sistrunk, E., Smith, D., Spinka, T., Stanley, J., Steele, R., Stolz, C., Suratwala, T., Telford, S., Thoma, J., VanBlarcom, D., Weiss, J., and Wegner, P. (2017). [High average power, diode pumped petawatt laser systems: a new generation of lasers enabling precision science and commercial applications](#). In Korn, G. and Silva, L. O., editors, *Research Using Extreme Light: Entering New Frontiers with Petawatt-Class Lasers III*, volume 10241, page 1024102. International Society for Optics and Photonics, SPIE.
- [Higuera and Cary, 2017] Higuera, A. V. and Cary, J. R. (2017). [Structure-preserving second-order integration of relativistic charged particle trajectories in electromagnetic fields](#). *Physics of Plasmas*, **24**(5):52104.
- [Hockney and Eastwood, 1988] Hockney, R. W. and Eastwood, J. W. (1988). *Computer Simulation Using Particles*. Hilger, Bristol.
- [Hooker, 2013] Hooker, S. M. (2013). [Developments in laser-driven plasma accelerators](#). *Nature Photonics*, **7**(10):775–782.
- [Hotz, 1965] Hotz, D. F. (1965). [Gain narrowing in a laser amplifier](#). *Applied Optics*, **4**(5):527.
- [Jeong et al., 2020] Jeong, T. M., Bulanov, S. V., Sasorov, P. V., Bulanov, S. S., Koga, J. K., and Korn, G. (2020). [4π-spherically focused electromagnetic wave: Diffraction optics approach and high-power limits](#). *Optics Express*, **28**(9):13991.
- [Jeong et al., 2021] Jeong, T. M., Bulanov, S. V., Valenta, P., Korn, G., Esirkepov, T. Z., Koga, J. K., Pirozhkov, A. S., Kando, M., and Bulanov, S. S. (2021). [Relativistic-flying laser focus by a laser-produced parabolic plasma mirror](#). *Physical Review A*, **104**(5):53533.
- [Jeong et al., 2015] Jeong, T. M., Weber, S., Le Garrec, B., Margarone, D., Mocek, T., and Korn, G. (2015). [Spatio-temporal modification of femtosecond focal spot under tight focusing condition](#). *Optics Express*, **23**(9):11641.
- [Kaganovich et al., 2008] Kaganovich, D., Gordon, D. F., and Ting, A. (2008). [Observation of large-angle quasimonoenergetic electrons from a laser wakefield](#). *Physical Review Letters*, **100**(21):215002.
- [Kaiser and Garrett, 1961] Kaiser, W. and Garrett, C. G. (1961). [Two-photon excitation in CaF₂: Eu²⁺](#). *Physical Review Letters*, **7**(6):229–231.
- [Kando et al., 2007] Kando, M., Fukuda, Y., Pirozhkov, A. S., Ma, J., Daito, I., Chen, L. M., Esirkepov, T. Z., Ogura, K., Homma, T., Hayashi, Y., Kotaki, H., Sagisaka, A., Mori, M., Koga, J. K., Daido, H., Bulanov, S. V., Kimura, T., Kato, Y., and Tajima, T. (2007). [Demonstration of laser-frequency upshift by electron-density modulations in a plasma wakefield](#). *Physical Review Letters*, **99**(13):135001.
- [Kando et al., 2009] Kando, M., Pirozhkov, A. S., Kawase, K., Esirkepov, T. Z., Fukuda, Y., Kiriyama, H., Okada, H., Daito, I., Kameshima, T., Hayashi, Y., Kotaki, H., Mori, M., Koga, J. K., Daido, H., Faenov, A. Y., Pikuz, T., Ma, J., Chen, L. M., Ragozin, E. N., Kawachi, T., Kato, Y., Tajima, T., and Bulanov, S. V. (2009). [Enhancement of photon number reflected by the relativistic flying mirror](#). *Physical Review Letters*, **103**(23):235003.
- [Kiefer et al., 2013] Kiefer, D., Yeung, M., Dzelzainis, T., Foster, P. S., Rykovanov, S. G., Lewis, C. L., Marjoribanks, R. S., Ruhl, H., Habs, D., Schreiber, J., Zepf, M., and Dromey, B. (2013). [Relativistic electron mirrors from nanoscale foils for coherent frequency upshift to the extreme ultraviolet](#). *Nature Communications*, **4**(1):1763.

- [Kim et al., 2002] Kim, A., Tushentsov, M., Cattani, F., Anderson, D., and Lisak, M. (2002). **Axisymmetric relativistic self-channeling of laser light in plasmas.** *Physical Review E*, **65**(3):36416.
- [Kim et al., 2013] Kim, H. T., Pae, K. H., Cha, H. J., Kim, I. J., Yu, T. J., Sung, J. H., Lee, S. K., Jeong, T. M., and Lee, J. (2013). **Enhancement of electron energy to the multi-GeV regime by a dual-stage laser-wakefield accelerator pumped by petawatt laser pulses.** *Physical Review Letters*, **111**(16):165002.
- [Koga et al., 2018] Koga, J. K., Bulanov, S. V., Esirkepov, T. Z., Kando, M., Bulanov, S. S., and Pirozhkov, A. S. (2018). **Relativistically upshifted higher harmonic generation via relativistic flying mirrors.** *Plasma Physics and Controlled Fusion*, **60**(7):74007.
- [Koga et al., 2012] Koga, J. K., Bulanov, S. V., Esirkepov, T. Z., Pirozhkov, A. S., Kando, M., and Rosanov, N. N. (2012). **Possibility of measuring photon-photon scattering via relativistic mirrors.** *Physical Review A*, **86**(5):53823.
- [Kovalev and Bychenkov, 2019] Kovalev, V. F. and Bychenkov, V. Y. (2019). **Analytic theory of relativistic self-focusing for a Gaussian light beam entering a plasma: Renormalization-group approach.** *Physical Review E*, **99**(4):43201.
- [Krausz and Ivanov, 2009] Krausz, F. and Ivanov, M. (2009). **Attosecond physics.** *Reviews of Modern Physics*, **81**(1):163–234.
- [Krushelnick et al., 1997] Krushelnick, K., Ting, A., Moore, C. I., Burris, H. R., Esarey, E., Sprangle, P., and Baine, M. (1997). **Plasma channel formation and guiding during high intensity short pulse laser plasma experiments.** *Physical Review Letters*, **78**(21):4047–4050.
- [Kulagin et al., 2007a] Kulagin, V. V., Cherepenin, V. A., Hur, M. S., and Suk, H. (2007). **Flying mirror model for interaction of a super-intense nonadiabatic laser pulse with a thin plasma layer: Dynamics of electrons in a linearly polarized external field.** *Physics of Plasmas*, **14**(11):113101.
- [Kulagin et al., 2007b] Kulagin, V. V., Cherepenin, V. A., Hur, M. S., and Suk, H. (2007). **Theoretical Investigation of Controlled Generation of a Dense Attosecond Relativistic Electron Bunch from the Interaction of an Ultrashort Laser Pulse with a Nanofilm.** *Physical Review Letters*, **99**(12):124801.
- [Lampa, 1924] Lampa, A. (1924). **Wie erscheint nach der Relativitätstheorie ein bewegter Stab einem ruhenden Beobachter?** *Zeitschrift für Physik*, **27**(1):138–148.
- [Leemans et al., 2014] Leemans, W. P., Gonsalves, A. J., Mao, H. S., Nakamura, K., Benedetti, C., Schroeder, C. B., Tóth, C., Daniels, J., Mittelberger, D. E., Bulanov, S. S., Vay, J. L., Geddes, C. G., and Esarey, E. (2014). **Multi-Gev electron beams from capillary-discharge-guided subpetawatt laser pulses in the self-trapping regime.** *Physical Review Letters*, **113**(24):245002.
- [Lehe et al., 2013] Lehe, R., Lifschitz, A., Thaury, C., Malka, V., and Davoine, X. (2013). **Numerical growth of emittance in simulations of laser-wakefield acceleration.** *Physical Review Special Topics - Accelerators and Beams*, **16**(2):21301.
- [Li et al., 2021] Li, Z., Kato, Y., and Kawanaka, J. (2021). **Simulating an ultra-broadband concept for Exawatt-class lasers.** *Scientific Reports*, **11**(1):151.

Bibliography

- [Lichters et al., 1996] Lichters, R., Meyer-ter Vehn, J., and Pukhov, A. (1996). [Short-pulse laser harmonics from oscillating plasma surfaces driven at relativistic intensity](#). *Physics of Plasmas*, **3**(9):3425–3437.
- [Liu, 1997] Liu, Q. H. (1997). [The PSTD algorithm: A time-domain method requiring only two cells per wavelength](#). *Microwave and Optical Technology Letters*, **15**(3):158–165.
- [Lu et al., 2006] Lu, W., Huang, C., Zhou, M., Mori, W. B., and Katsouleas, T. (2006). [Nonlinear theory for relativistic plasma wakefields in the blowout regime](#). *Physical Review Letters*, **96**(16):165002.
- [Lu et al., 2007] Lu, W., Tzoufras, M., Joshi, C., Tsung, F. S., Mori, W. B., Vieira, J., Fonseca, R. A., and Silva, L. O. (2007). [Generating multi-GeV electron bunches using single stage laser wakefield acceleration in a 3D nonlinear regime](#). *Physical Review Special Topics - Accelerators and Beams*, **10**(6):61301.
- [Lundh et al., 2011] Lundh, O., Lim, J., Rechatin, C., Ammoura, L., Ben-Ismaïl, A., Davoine, X., Gallot, G., Goddet, J. P., Lefebvre, E., Malka, V., and Faure, J. (2011). [Few femtosecond, few kiloampere electron bunch produced by a laser-plasma accelerator](#). *Nature Physics*, **7**(3):219–222.
- [Ma et al., 2014] Ma, W. J., Bin, J. H., Wang, H. Y., Yeung, M., Kreuzer, C., Streeter, M., Foster, P. S., Cousens, S., Kiefer, D., Dromey, B., Yan, X. Q., Meyer-Ter-Vehn, J., Zepf, M., and Schreiber, J. (2014). [Bright subcycle extreme ultraviolet bursts from a single dense relativistic electron sheet](#). *Physical Review Letters*, **113**(23):235002.
- [Maiman, 1960] Maiman, T. H. (1960). [Stimulated optical radiation in Ruby](#). *Nature*, **187**(4736):493–494.
- [Maine and Mourou, 1988] Maine, P. and Mourou, G. (1988). [Amplification of 1-nsec pulses in Nd:glass followed by compression to 1 psec](#). *Optics Letters*, **13**(6):467–469.
- [Maker et al., 1964] Maker, P. D., Terhune, R. W., and Savage, C. M. (1964). [Intensity-dependent changes in the refractive index of liquids](#). *Physical Review Letters*, **12**(18):507–509.
- [Maksimchuk et al., 2008] Maksimchuk, A., Reed, S., Bulanov, S. S., Chvykov, V., Kalintchenko, G., Matsuka, T., McGuffey, C., Mourou, G., Naumova, N., Nees, J., Rousseau, P., Yanovsky, V., Krushelnick, K., Matlis, N. H., Kalmykov, S., Shvets, G., Downer, M. C., Vane, C. R., Beene, J. R., Stracener, D., and Schultz, D. R. (2008). [Studies of laser wakefield structures and electron acceleration in underdense plasmas](#). *Physics of Plasmas*, **15**(5):56703.
- [Malka et al., 2010] Malka, V., Faure, J., and Gauduel, Y. A. (2010). [Ultra-short electron beams based spatio-temporal radiation biology and radiotherapy](#). *Mutation Research*, **704**(1-3):142–151.
- [Mangles et al., 2004] Mangles, S. P., Murphy, C. D., Najmudin, Z., Thomas, A. G., Collier, J. L., Dangor, A. E., Divall, E. J., Foster, P. S., Gallacher, J. G., Hooker, C. J., Jaroszynski, D. A., Langley, A. J., Mori, W. B., Norreys, P. A., Tsung, F. S., Viskup, R., Walton, B. R., and Krushelnick, K. (2004). [Monoenergetic beams of relativistic electrons from intense laser-plasma interactions](#). *Nature*, **431**(7008):535–538.

- [Matlis et al., 2006] Matlis, N. H., Reed, S., Bulanov, S. S., Chvykov, V., Kalintchenko, G., Matsuoka, T., Rousseau, P., Yanovsky, V., Maksimchuk, A., Kalmykov, S., Shvets, G., and Downer, M. C. (2006). **Snapshots of laser wakefields**. *Nature Physics*, **2**(11):749–753.
- [McClung and Hellwarth, 1962] McClung, F. J. and Hellwarth, R. W. (1962). **Giant optical pulsations from ruby**. *Journal of Applied Physics*, **33**(3):828–829.
- [Miller, 2014] Miller, R. J. (2014). **Femtosecond crystallography with ultrabright electrons and x-rays: Capturing chemistry in action**. *Science*, **343**(6175):1108–1116.
- [Mocker and Collins, 1965] Mocker, H. W. and Collins, R. J. (1965). **Mode competition and self-locking effects in a Q-switched ruby laser**. *Applied Physics Letters*, **7**(10):270–273.
- [Mori et al., 1988] Mori, W. B., Joshi, C., Dawson, J. M., Forslund, D. W., and Kindel, J. M. (1988). **Evolution of self-focusing of intense electromagnetic waves in plasma**. *Physical Review Letters*, **60**(13):1298–1301.
- [Morse and Nielson, 1971] Morse, R. L. and Nielson, C. W. (1971). **Numerical simulation of the Weibel instability in one and two dimensions**. *Physics of Fluids*, **14**(4):830–840.
- [Mourou et al., 2002] Mourou, G., Chang, Z., Maksimchuk, A., Nees, J., Bulanov, S. V., Bychenkov, V. Y., Esirkepov, T. Z., Naumova, N. M., Pegoraro, F., and Ruhl, H. (2002). **On the design of experiments for the study of relativistic nonlinear optics in the limit of single-cycle pulse duration and single-wavelength spot size**. *Plasma Physics Reports*, **28**(1):12–27.
- [Muroya et al., 2008] Muroya, Y., Lin, M., Han, Z., Kumagai, Y., Sakumi, A., Ueda, T., and Katsumura, Y. (2008). **Ultra-fast pulse radiolysis: A review of the recent system progress and its application to study on initial yields and solvation processes of solvated electrons in various kinds of alcohols**. *Radiation Physics and Chemistry*, **77**(10-12):1176–1182.
- [Nagy et al., 2020] Nagy, T., Kretschmar, M., Vrakking, M. J. J., and Rouzée, A. (2020). **Generation of above-terawatt 1.5-cycle visible pulses at 1 kHz by post-compression in a hollow fiber**. *Optics Letters*, **45**(12):3313.
- [Nakatsutsumi et al., 2010] Nakatsutsumi, M., Kon, A., Buffeaux, S., Audebert, P., Fuchs, J., and Kodama, R. (2010). **Fast focusing of short-pulse lasers by innovative plasma optics toward extreme intensity**. *Optics Letters*, **35**(13):2314.
- [Naseri et al., 2016] Naseri, N., Rozmus, W., and Pesme, D. (2016). **Self-channelling of intense laser pulses in underdense plasma and stability analysis**. *Physics of Plasmas*, **23**(11):113101.
- [Naumova et al., 2004] Naumova, N. M., Nees, J. A., Sokolov, I. V., Hou, B., and Mourou, G. A. (2004). **Relativistic generation of isolated attosecond pulses in a λ^3 focal volume**. *Physical Review Letters*, **92**(6):063902.
- [Neutzo et al., 2000] Neutzo, R., Wouts, R., Van Der Spoel, D., Weckert, E., and Hajdu, J. (2000). **Potential for biomolecular imaging with femtosecond X-ray pulses**. *Nature*, **406**(6797):752–757.
- [Nisoli et al., 1996] Nisoli, M., De Silvestri, S., and Svelto, O. (1996). **Generation of high energy 10 fs pulses by a new pulse compression technique**. *Applied Physics Letters*, **68**(20):2793–2795.

Bibliography

- [Ohkubo et al., 2007] Ohkubo, T., Maekawa, A., Tsujii, R., Hosokai, T., Kinoshita, K., Kobayashi, K., Uesaka, M., Zhidkov, A., Nemoto, K., Kondo, Y., and Shibata, Y. (2007). **Temporal characteristics of monoenergetic electron beams generated by the laser wakefield acceleration.** *Physical Review Special Topics - Accelerators and Beams*, **10**(3):31301.
- [Osvay et al., 2019] Osvay, K., Börzsönyi, Á., Cao, H., Cormier, E., Csontos, J., Jójárt, P., Kalashnikov, M., Kiss, B., López-Martens, R., Tóth, S., and Varallyay, Z. (2019). **Development status and operation experiences of the few cycle high average power lasers of ELI-ALPS.** In Bakule, P. and Haefner, C. L., editors, *Short-pulse High-energy Lasers and Ultrafast Optical Technologies*, volume 11034, page 19. International Society for Optics and Photonics, SPIE.
- [Ouillé et al., 2020] Ouillé, M., Vernier, A., Böhle, F., Bocoum, M., Jullien, A., Lozano, M., Rousseau, J. P., Cheng, Z., Gustas, D., Blumenstein, A., Simon, P., Haessler, S., Faure, J., Nagy, T., and Lopez-Martens, R. (2020). **Relativistic-intensity near-single-cycle light waveforms at kHz repetition rate.** *Light: Science and Applications*, **9**(1):47.
- [Panchenko et al., 2008] Panchenko, A. V., Esirkepov, T. Z., Pirozhkov, A. S., Kando, M., Kamenets, F. F., and Bulanov, S. V. (2008). **Interaction of electromagnetic waves with caustics in plasma flows.** *Physical Review E*, **78**(5):56402.
- [Peng et al., 2019] Peng, H., Marquès, J. R., Lancia, L., Amiranoff, F., Berger, R. L., Weber, S., and Riconda, C. (2019). **Plasma optics in the context of high intensity lasers.** *Matter and Radiation at Extremes*, **4**(6):65401.
- [Penrose, 1959] Penrose, R. (1959). **The apparent shape of a relativistically moving sphere.** *Mathematical Proceedings of the Cambridge Philosophical Society*, **55**(1):137–139.
- [Perry et al., 1999] Perry, M. D., Pennington, D., Stuart, B. C., Tietbohl, G., Britten, J. A., Brown, C., Herman, S., Golick, B., Kartz, M., Miller, J., Powell, H. T., Vergino, M., and Yanovsky, V. (1999). **Petawatt laser pulses.** *Optics Letters*, **24**(3):160.
- [Pirozhkov et al., 2006] Pirozhkov, A. S., Bulanov, S. V., Esirkepov, T. Z., Mori, M., Sagisaka, A., and Daido, H. (2006). **Attosecond pulse generation in the relativistic regime of the laser-foil interaction: The sliding mirror model.** *Physics of Plasmas*, **13**(1):1–12.
- [Pirozhkov et al., 2018] Pirozhkov, A. S., Esirkepov, T. Z., Pikuz, T., Faenov, A., Sagisaka, A., Ogura, K., Hayashi, Y., Kotaki, H., Ragozin, E., Neely, D., Koga, J., Fukuda, Y., Nishikino, M., Imazono, T., Hasegawa, N., Kawachi, T., Daido, H., Kato, Y., Bulanov, S., Kondo, K., Kiriyama, H., and Kando, M. (2018). **Laser requirements for high-order harmonic generation by relativistic plasma singularities.** *Quantum Beam Science*, **2**(1):7.
- [Pirozhkov et al., 2017] Pirozhkov, A. S., Esirkepov, T. Z., Pikuz, T. A., Faenov, A. Y., Ogura, K., Hayashi, Y., Kotaki, H., Ragozin, E. N., Neely, D., Kiriyama, H., Koga, J. K., Fukuda, Y., Sagisaka, A., Nishikino, M., Imazono, T., Hasegawa, N., Kawachi, T., Bolton, P. R., Daido, H., Kato, Y., Kondo, K., Bulanov, S. V., and Kando, M. (2017). **Burst intensification by singularity emitting radiation in multi-stream flows.** *Scientific Reports*, **7**(1):17968.
- [Pirozhkov et al., 2012] Pirozhkov, A. S., Kando, M., Esirkepov, T. Z., Gallegos, P., Ahmed, H., Ragozin, E. N., Faenov, A. Y., Pikuz, T. A., Kawachi, T., Sagisaka, A., Koga, J. K., Coury, M., Green, J., Foster, P., Brenner, C., Dromey, B., Symes, D. R., Mori, M., Kawase, K., Kameshima, T., Fukuda, Y., Chen, L., Daito, I., Ogura, K., Hayashi, Y., Kotaki, H.,

- Kiriyama, H., Okada, H., Nishimori, N., Imazono, T., Kondo, K., Kimura, T., Tajima, T., Daido, H., Rajeev, P., McKenna, P., Borghesi, M., Neely, D., Kato, Y., and Bulanov, S. V. (2012). [Soft-x-ray harmonic comb from relativistic electron spikes](#). *Physical Review Letters*, **108**(13):135004.
- [Pirozhkov et al., 2014] Pirozhkov, A. S., Kando, M., Esirkepov, T. Z., Gallegos, P., Ahmed, H., Ragozin, E. N., Faenov, A. Y., Pikuz, T. A., Kawachi, T., Sagisaka, A., Koga, J. K., Coury, M., Green, J., Foster, P., Brenner, C., Dromey, B., Symes, D. R., Mori, M., Kawase, K., Kameshima, T., Fukuda, Y., Chen, L., Daito, I., Ogura, K., Hayashi, Y., Kotaki, H., Kiriyama, H., Okada, H., Nishimori, N., Imazono, T., Kondo, K., Kimura, T., Tajima, T., Daido, H., Rajeev, P., McKenna, P., Borghesi, M., Neely, D., Kato, Y., and Bulanov, S. V. (2014). [High order harmonics from relativistic electron spikes](#). *New Journal of Physics*, **16**(9):93003.
- [Pirozhkov et al., 2007] Pirozhkov, A. S., Ma, J., Kando, M., Esirkepov, T. Z., Fukuda, Y., Chen, L. M., Daito, I., Ogura, K., Homma, T., Hayashi, Y., Kotaki, H., Sagisaka, A., Mori, M., Koga, J. K., Kawachi, T., Daido, H., Bulanov, S. V., Kimura, T., Kato, Y., and Tajima, T. (2007). [Frequency multiplication of light back-reflected from a relativistic wake wave](#). *Physics of Plasmas*, **14**(12):123106.
- [Pollock et al., 2015] Pollock, B. B., Tsung, F. S., Albert, F., Shaw, J. L., Clayton, C. E., Davidson, A., Lemos, N., Marsh, K. A., Pak, A., Ralph, J. E., Mori, W. B., and Joshi, C. (2015). [Formation of ultrarelativistic electron rings from a laser-wakefield accelerator](#). *Physical Review Letters*, **115**(5):55004.
- [Press et al., 2007] Press, W. H., Teukolsky, S. A., Vetterling, W. T., and Flannery, B. P. (2007). *Numerical Recipes: The Art of Scientific Computing*. Cambridge University Press, USA, 3rd edition.
- [Pukhov, 1999] Pukhov, A. (1999). [Three-dimensional electromagnetic relativistic particle-in-cell code VLPL \(Virtual Laser Plasma Lab\)](#). *Journal of Plasma Physics*, **61**(3):425–433.
- [Pukhov and Meyer-ter Vehn, 2002] Pukhov, A. and Meyer-ter Vehn, J. (2002). [Laser wake field acceleration: The highly non-linear broken-wave regime](#). *Applied Physics B*, **74**(4-5):355–361.
- [Rivas et al., 2017] Rivas, D. E., Borot, A., Cardenas, D. E., Marcus, G., Gu, X., Herrmann, D., Xu, J., Tan, J., Kormin, D., Ma, G., Dallari, W., Tsakiris, G. D., Földes, I. B., Chou, S. W., Weidman, M., Bergues, B., Wittmann, T., Schröder, H., Tzallas, P., Charalambidis, D., Razskazovskaya, O., Pervak, V., Krausz, F., and Veisz, L. (2017). [Next generation driver for attosecond and laser-plasma physics](#). *Scientific Reports*, **7**(1):5224.
- [Sagisaka et al., 2020] Sagisaka, A., Ogura, K., Esirkepov, T. Z., Neely, D., Pikuz, T. A., Koga, J. K., Fukuda, Y., Kotaki, H., Hayashi, Y., Gonzalez-Izquierdo, B., Huang, K., Bulanov, S. V., Kiriyama, H., Kondo, K., Kawachi, T., Kando, M., and Pirozhkov, A. S. (2020). [Observation of burst intensification by singularity emitting radiation generated from relativistic plasma with a high-intensity laser](#). *High Energy Density Physics*, **36**:100751.
- [Salehi et al., 2019] Salehi, F., Goers, A. J., Feder, L., Miao, B., Woodbury, D., and Milchberg, H. M. (2019). [Characterization of a 100 micrometer-scale cryogenically cooled gas jet for near-critical density laser-plasma experiments](#). *Review of Scientific Instruments*, **90**(10):103001.

Bibliography

- [Salehi et al., 2021] Salehi, F., Le, M., Railing, L., Kolesik, M., and Milchberg, H. M. (2021). [Laser-accelerated, low-divergence 15-MeV quasimonoenergetic electron bunches at 1 kHz](#). *Physical Review X*, **11**(2):21055.
- [Sciaini and Miller, 2011] Sciaini, G. and Miller, R. J. (2011). [Femtosecond electron diffraction: Heralding the era of atomically resolved dynamics](#). *Reports on Progress in Physics*, **74**(9):96101.
- [Shadwick et al., 2002] Shadwick, B. A., Tarkenton, G. M., Esarey, E. H., and Leemans, W. P. (2002). [Fluid simulations of intense laser-plasma interactions](#). *IEEE Transactions on Plasma Science*, **30**(1):38–39.
- [Strickland and Mourou, 1985] Strickland, D. and Mourou, G. (1985). [Compression of amplified chirped optical pulses](#). *Optics Communications*, **56**(3):219–221.
- [Ta Phuoc et al., 2012] Ta Phuoc, K., Corde, S., Thaury, C., Malka, V., Tafzi, A., Goddet, J. P., Shah, R. C., Sebbar, S., and Rousse, A. (2012). [All-optical Compton gamma-ray source](#). *Nature Photonics*, **6**(5):308–311.
- [Tabak et al., 1994] Tabak, M., Hammer, J., Glinsky, M. E., Krueer, W. L., Wilks, S. C., Woodworth, J., Campbell, E. M., Perry, M. D., and Mason, R. J. (1994). [Ignition and high gain with ultrapowerful lasers](#). *Physics of Plasmas*, **1**(5):1626–1634.
- [Tajima and Dawson, 1979] Tajima, T. and Dawson, J. M. (1979). [Laser electron accelerator](#). *Physical Review Letters*, **43**(4):267–270.
- [Tamburini et al., 2014] Tamburini, M., Di Piazza, A., Liseykina, T. V., and Keitel, C. H. (2014). [Plasma-based generation and control of a single few-cycle high-energy ultrahigh-intensity laser pulse](#). *Physical Review Letters*, **113**(2):25005.
- [Tanaka et al., 2020] Tanaka, K. A., Spohr, K. M., Balabanski, D. L., Balascuta, S., Capponi, L., Cernaianu, M. O., Cuciuc, M., Cucoanes, A., Dancus, I., Dhal, A., Diaconescu, B., Doria, D., Ghenuche, P., Ghita, D. G., Kisoyov, S., Nastasa, V., Ong, J. F., Rotaru, F., Sangwan, D., Söderström, P. A., Stutman, D., Suliman, G., Tesileanu, O., Tudor, L., Tsoneva, N., Ur, C. A., Ursescu, D., and Zamfir, N. V. (2020). [Current status and highlights of the ELI-NP research program](#). *Matter and Radiation at Extremes*, **5**(2):24402.
- [Terrell, 1959] Terrell, J. (1959). [Invisibility of the Lorentz contraction](#). *Physical Review*, **116**(4):1041–1045.
- [Thaury et al., 2007] Thaury, C., Quéré, F., Geindre, J. P., Levy, A., Ceccotti, T., Monot, P., Bougeard, M., Réau, F., D’Oliveira, P., Audebert, P., Marjoribanks, R., and Martin, P. (2007). [Plasma mirrors for ultrahigh-intensity optics](#). *Nature Physics*, **3**(6):424–429.
- [Toth et al., 2020] Toth, S., Stanislauskas, T., Balciunas, I., Budriunas, R., Adamonis, J., Danilevicius, R., Viskontas, K., Lengvinas, D., Veitas, G., Gadonas, D., Varanavičius, A., Csontos, J., Somoskoi, T., Toth, L., Borzsonyi, A., and Osvay, K. (2020). [SYLOS lasers - The frontier of few-cycle, multi-TW, kHz lasers for ultrafast applications at extreme light infrastructure attosecond light pulse source](#). *Journal of Physics: Photonics*, **2**(4):45003.
- [Umeda et al., 2003] Umeda, T., Omura, Y., Tominaga, T., and Matsumoto, H. (2003). [A new charge conservation method in electromagnetic particle-in-cell simulations](#). *Computer Physics Communications*, **156**(1):73–85.

- [Valenta, 2017] Valenta, P. (2017). *Tight-focusing of short intense laser pulses in particle-in-cell simulations of laser-plasma interaction*. Master's thesis, Czech Technical University in Prague.
- [Van Tilborg et al., 2006] Van Tilborg, J., Schroeder, C. B., Filip, C. V., Tóth, C., Geddes, C. G., Fubiani, G., Huber, R., Kaindl, R. A., Esarey, E., and Leemans, W. P. (2006). **Temporal characterization of femtosecond laser-plasma-accelerated electron bunches using terahertz radiation**. *Physical Review Letters*, **96**(1):014801.
- [Vay, 2008] Vay, J. L. (2008). **Simulation of beams or plasmas crossing at relativistic velocity**. *Physics of Plasmas*, **15**(5):56701.
- [Vay et al., 2011] Vay, J. L., Geddes, C. G., Cormier-Michel, E., and Grote, D. P. (2011). **Numerical methods for instability mitigation in the modeling of laser wakefield accelerators in a Lorentz-boosted frame**. *Journal of Computational Physics*, **230**(15):5908–5929.
- [Vay et al., 2013] Vay, J. L., Haber, I., and Godfrey, B. B. (2013). **A domain decomposition method for pseudo-spectral electromagnetic simulations of plasmas**. *Journal of Computational Physics*, **243**:260–268.
- [Villasenor and Buneman, 1992] Villasenor, J. and Buneman, O. (1992). **Rigorous charge conservation for local electromagnetic field solvers**. *Computer Physics Communications*, **69**(2-3):306–316.
- [Vincenti, 2019] Vincenti, H. (2019). **Achieving extreme light intensities using optically curved relativistic plasma mirrors**. *Physical Review Letters*, **123**(10):105001.
- [Vincenti and Vay, 2016] Vincenti, H. and Vay, J. L. (2016). **Detailed analysis of the effects of stencil spatial variations with arbitrary high-order finite-difference Maxwell solver**. *Computer Physics Communications*, **200**:147–167.
- [Voronov and Delone, 1966] Voronov, G. and Delone, N. (1966). Many-photon ionization of the xenon atom by ruby laser radiation. *Journal of Experimental and Theoretical Physics*, **23**(1):54.
- [Wheeler et al., 2012] Wheeler, J., Borot, A., Malvache, A., Ricci, A., Jullien, A., Lopez-Martens, R., Monchocé, S., Vincenti, H., and Quéré, F. (2012). **Attosecond lighthouses from plasma mirrors**. *Nature Photonics*, **6**(12):829–833.
- [Woodbury and Ng, 1962] Woodbury, E. J. and Ng, W. K. (1962). Ruby laser operation in near IR. *Proceedings of the Institute of Radio Engineers*, **50**(11):2367.
- [Wu et al., 2010] Wu, H. C., Meyer-Ter-Vehn, J., Fernández, J., and Hegelich, B. M. (2010). **Uniform laser-driven relativistic electron layer for coherent thomson scattering**. *Physical Review Letters*, **104**(23):234801.
- [Yang et al., 2017] Yang, X., Brunetti, E., Gil, D. R., Welsh, G. H., Li, F. Y., Cipiccia, S., Ersfeld, B., Grant, D. W., Grant, P. A., Islam, M. R., Tooley, M. P., Vieux, G., Wiggins, S. M., Sheng, Z. M., and Jaroszynski, D. A. (2017). **Three electron beams from a laser-plasma wakefield accelerator and the energy apportioning question**. *Scientific Reports*, **7**(1):43910.
- [Yee, 1966] Yee, K. S. (1966). Numerical solution of initial boundary value problems involving Maxwell's equations in isotropic media. *IEEE Transactions on Antennas and Propagation*, **14**(3):302–307.

Bibliography

- [Yoon et al., 2021] Yoon, J. W., Kim, Y. G., Choi, I. W., Sung, J. H., Lee, H. W., Lee, S. K., and Nam, C. H. (2021). [Realization of laser intensity over \$10^{23}\$ W/cm²](#). *Optica*, **8**(5):630.
- [Zeng et al., 2017] Zeng, X., Zhou, K., Zuo, Y., Zhu, Q., Su, J., Wang, X., Wang, X., Huang, X., Jiang, X., Jiang, D., Guo, Y., Xie, N., Zhou, S., Wu, Z., Mu, J., Peng, H., and Jing, F. (2017). [Multi-petawatt laser facility fully based on optical parametric chirped-pulse amplification](#). *Optics Letters*, **42**(10):2014.
- [Zhang et al., 2012] Zhang, L., Chen, L. M., Wang, W. M., Yan, W. C., Yuan, D. W., Mao, J. Y., Wang, Z. H., Liu, C., Shen, Z. W., Faenov, A., Pikuz, T., Li, D. Z., Li, Y. T., Dong, Q. L., Lu, X., Ma, J. L., Wei, Z. Y., Sheng, Z. M., and Zhang, J. (2012). [Electron acceleration via high contrast laser interacting with submicron clusters](#). *Applied Physics Letters*, **100**(1):14104.
- [Zhao et al., 2016] Zhao, T. Z., Behm, K., Dong, C. F., Davoine, X., Kalmykov, S. Y., Petrov, V., Chvykov, V., Cummings, P., Hou, B., Maksimchuk, A., Nees, J. A., Yanovsky, V., Thomas, A. G., and Krushelnick, K. (2016). [High-flux femtosecond x-ray emission from controlled generation of annular electron beams in a laser wakefield accelerator](#). *Physical Review Letters*, **117**(9):94801.

Appendices

A

List of author's publications

Below, the reader can find the full list of publications (as of the day of submission of this dissertation) in peer-reviewed journals, conference proceedings, and as book chapters authored or co-authored by the author during the author's postgraduate studies. The publications are listed in chronological order.

A.1 Publications in peer-reviewed journals

- Mu, J., Esirkepov, T. Z., Valenta, P., Jeong, T. M., Gu, Y., Koga, J. K., Pirozhkov, A. S., Kando, M., Korn, G., and Bulanov, S. V. (2019). [High-order harmonics from laser irradiated electron density singularity formed at the bow wave in the laser plasma](#). *Physics of Wave Phenomena*, **27**(4):247-256.
- Valenta, P., Esirkepov, T. Z., Koga, J. K., Pirozhkov, A. S., Kando, M., Kawachi, T., Liu, Y. K., Fang, P., Chen, P., Mu, J., Korn, G., Klimo, O., and Bulanov, S. V. (2020). [Recoil effects on reflection from relativistic mirrors in laser plasmas](#)., *Physics of Plasmas*, **27**(3):032109.
- Esirkepov, T. Z., Mu, J., Gu, Y., Jeong, T. M., Valenta, P., Klimo, O., Koga, J. K., Kando, M., Neely, D., Korn, G., Bulanov, S. V., and Pirozhkov, A. S. (2020). [Optical probing of relativistic plasma singularities](#). *Physics of Plasmas*, **27**(3):052103.
- Mu, J., Esirkepov, T. Z., Valenta, P., Gu, Y., Jeong, T. M., Pirozhkov, A. S., Koga, J. K., Kando, M., Korn, G., and Bulanov, S. V. (2020). [Relativistic flying forcibly oscillating reflective diffraction grating](#). *Physical Review E*, **102**(5):053202.
- Valenta, P., Esirkepov, T. Z., Koga, J. K., Nečas, A., Grittani, G. M., Lazzarini, C. M., Klimo, O., Korn, G., and Bulanov, S. V. (2020). [Polarity reversal of wakefields driven by ultrashort pulse laser](#). *Physical Review E*, **102**(5):053216.
- Hadjisolomou, P., Jeong, T. M., Valenta, P., Korn, G., and Bulanov, S. V. (2021). [Gamma-ray flash generation in irradiating a thin foil target by a single-cycle tightly focused extreme power laser pulse](#). *Physical Review E*, **104**(1):015203.

- Jeong, T. M., Bulanov, S. V., Valenta, P., Korn, G., Esirkepov, T. Z., Koga, J. K., Pirozhkov, A. S., Kando, M., and Bulanov, S. S. (2021). **Relativistic-flying laser focus by a laser-produced parabolic plasma mirror.** *Physical Review A*, **104**(6):053533.
- Valenta, P., Grittani, G. M., Lazzarini, C. M., Klimo, O., and Bulanov, S. V. (2021). **On the electromagnetic-electron rings originating from the interaction of high-power short-pulse laser and underdense plasma.** *Physics of Plasmas*, **28**(12):122104.
- Hadjisolomou, P., Jeong, T. M., Valenta, P., Kolenatý, D., Versaci, R., Olšovcová, V., Ridgers, C. P., and Bulanov, S. V. (2021). **Gamma-ray flash in the interaction of a tightly focused single-cycle ultraintense laser pulse with a solid target.** *Journal of Plasma Physics*, **XXX**(X):XXXXXX.

A.2 Publications in conference proceedings

- Klimo, O., Valenta, P., and Weber, S. (2017). **Laser absorption and ion acceleration under tight-focusing conditions.** *44th EPS Conference on Plasma Physics*, P5.225.
- Valenta, P., Klimo, O., Bulanov, S. V., and Korn, G. (2018). **On high-quality electron beam generated by breaking wake wave in near-critical density plasmas.** *45th EPS Conference on Plasma Physics*, P2.2031.
- Valenta, P., Klimo, O., Grittani, G. M., Esirkepov, T. Z., Korn, G., and Bulanov, S. V. (2019). **Wakefield excited by ultrashort laser pulses in near-critical density plasmas.** *Proc. SPIE 11037, Laser Acceleration of Electrons, Protons, and Ions V*, 110370T.
- Mu, J., Gu, Y., Jeong, T. M., Valenta, P., Klimo, O., Esirkepov, T. Z., Pirozhkov, A. S., Koga, J. K., Kando, M., Korn, G., and Bulanov, S. V. (2019). **High order harmonics generation via laser reflection at electron density peaks.** *Proc. SPIE 11039, Research Using Extreme Light: Entering New Frontiers with Petawatt-Class Lasers IV*, 110390H.
- Lazzarini, C. M., Goncalves, L. V., Grittani, G. M., Lorenz, S., Nevrkla, M., Valenta, P., Levato, T., Bulanov, S. V., and Korn, G. (2020). **Electron acceleration at ELI Beamlines: towards high-energy and high-repetition-rate accelerators.** *International Journal of Modern Physics A*, **34**(34):1943010.
- Valenta, P., Esirkepov, T. Z., Koga, J. K., Pirozhkov, A. S., Kando, M., Kawachi, T., Liu, Y. K., Fang, P., Chen, P., Mu, J., Korn, G., Klimo, O., and Bulanov, S. V. (2020). **Relativistic flying mirrors as a compact source of coherent short-wavelength radiation.** *OSA High-brightness Sources and Light-driven Interactions Congress 2020*, EM1A.5.
- Valenta, P., Grittani, G. M., Lazzarini, C. M., Klimo, O., and Bulanov, S. V. (2021). **Ring-shaped electron beams from laser-wakefield accelerator.** *Proc. SPIE 11779, Laser Acceleration of Electrons, Protons, and Ions VI*, 11777909.
- Jeong, T. M., Bulanov, S. V., Valenta, P., Korn, G., Esirkepov, T. Z., Koga, J. K., and Pirozhkov, A. S (2021) **Ultra-strong attosecond laser focus produced by a relativistic-flying parabolic mirror.** *Proc. SPIE 11886, International Conference on X-Ray Lasers 2020*, 118860H.

A.3 Book chapters

- Matys, M., Pšikal, J., Danielová, M., Valenta, P., and Bulanov, S. V. (2019). [Laser-driven ion acceleration using cryogenic hydrogen targets](#). *Supercomputing in Science and Engineering 2017-18*, pp. 149-151.
- Lazzarini, C. M., Goncalves, L. V., Grittani, G. M., Lorenz, S., Nevrkla, M., Valenta, P., Levato, T., Bulanov, S. V., and Korn, G. (2020) [Electron acceleration at ELI Beamlines: towards high-energy and high-repetition-rate accelerators](#). *Beam Acceleration in Crystals and Nanostructures*, pp. 153-170.
- Matys, M., Valenta, P., Kecová, M., Nishihara, K., Pšikal, J., Esirkepov, T. Z., Koga, J. K., Nečas, A., Grittani, G. M., Lazzarini, C. M., Klimo, O., Korn, G., and Bulanov, S. V. (2021). [Laser-driven acceleration of charged particles](#). *Supercomputing in Science and Engineering 2019-20*, pp. 86-88.

B

Selected publications

- B.1. On the electromagnetic-electron rings originating from the interaction of high-power short-pulse laser and underdense plasma
-

B.1 On the electromagnetic-electron rings originating from the interaction of high-power short-pulse laser and underdense plasma

The following article is reproduced from Valenta, P., Grittani, G. M., Lazzarini, C. M., Klimo, O., and Bulanov, S. V. (2021). [On the electromagnetic-electron rings originating from the interaction of high-power short-pulse laser and underdense plasma](#). *Physics of Plasmas*, **28**(12):122104, with the permission of AIP Publishing.

Copyright © 2021 American Institute of Physics.

On the electromagnetic-electron rings originating from the interaction of high-power short-pulse laser and underdense plasma

F SCI

Cite as: Phys. Plasmas **28**, 122104 (2021); doi: 10.1063/5.0065167

Submitted: 30 July 2021 · Accepted: 7 November 2021 ·

Published Online: 6 December 2021



View Online



Export Citation



CrossMark

P. Valenta,^{1,2,a)} G. M. Grittani,¹ C. M. Lazzarini,^{1,2} O. Klimo,^{1,2} and S. V. Bulanov^{1,3}

AFFILIATIONS

¹ELI Beamlines Centre, Institute of Physics, Czech Academy of Sciences, Za Radnicí 835, 25241 Dolní Břežany Czech Republic²Faculty of Nuclear Sciences and Physical Engineering, Czech Technical University in Prague, Břehová 7, 11519 Prague, Czech Republic³Kansai Photon Science Institute, National Institutes for Quantum Science and Technology, Umemidai 8-1-7, Kizugawa, 619-0215 Kyoto, Japan^{a)}Author to whom correspondence should be addressed: petr.valenta@eli-beams.eu

ABSTRACT

We investigate the evolution of radial profile of a high-power short-pulse laser interacting with underdense plasma, and in particular, we concentrate on the transverse electromagnetic rings, which are formed due to the laser radiation defocusing induced by the excitation of Langmuir waves. We illustrate the physical processes involved in the formation of such structures analytically and use the three-dimensional numerical simulations to reveal the relationships among the electromagnetic ring properties and the parameters of laser and plasma. Within the studied parameter range, we find that up to $\approx 70\%$ of the total initial driver pulse energy can be carried off by the electromagnetic rings having the opening angles $\approx 45\text{--}115$ mrad. Furthermore, we show that the electromagnetic rings can become a source of high-energy ring-shaped electron beams.

Published under an exclusive license by AIP Publishing. <https://doi.org/10.1063/5.0065167>

I. INTRODUCTION

A high-power laser pulse propagation in underdense plasmas is relevant to a number of scientific challenges, such as laser-driven acceleration of charged particles,^{1–3} development of sources of hard electromagnetic (EM) radiation,^{4,5} and nuclear fusion within the framework of the fast ignition concept.⁶ For many of these applications, it is essential that the laser pulse propagates over extended distances and transmits its energy into plasma in a controlled way without incurring excessive losses. At high laser power, relativistic effects change the properties of the collective response of the plasma. This concerns the propagation as qualitatively new processes occur, including relativistic self-focusing,^{7,8} filamentation,^{9,10} and formation of solitons^{11–14} and vortices.^{15,16}

In this context, much of the attention has been focused on the evolution of the radial profile of the laser beam in a fully ionized plasma. It turned out that the process of self-focusing for high-power laser pulses may lead to the formation of the multifilament and, in particular, ring-shaped transverse structures as reported in numerous theoretical and experimental works.^{17–25} In this paper, we present a

systematic study focused on the formation of the EM rings in the regime of high-power, ultrashort laser pulses, where the longitudinal charge separation and the generation of Langmuir waves cannot be neglected. The physical processes involved in the formation of the EM rings are illustrated using an analytical model based on the geometric optics approximation and demonstrated by a three-dimensional (3D) particle-in-cell (PIC) simulation. The properties of the EM rings are revealed by a multi-parametric PIC study for various plasma densities, laser intensities, and laser spot sizes. Furthermore, we show that the EM rings can become a source of high-energy ring-shaped electron beams.

The EM and electron ring structures are of interest for a number of potential applications. The EM rings, in the form of Laguerre-Gaussian laser pulses, have been studied as drivers for the plasma acceleration of electrons, positrons, and ions.^{26–32} The hollow electron ring structures have been considered as drivers for the plasma acceleration of positrons,^{33,34} as a source of high-flux x rays,³⁵ and as compact collimators for proton bunches in radio frequency accelerators.³⁶

In addition to the applications mentioned above, the understanding of the physical processes that lead to the generation of the EM and electron ring structures is important due to the following reasons: (i) The EM rings may carry off a significant fraction of energy from the driver and, thus, limit the overall efficiency of applications based on the laser-plasma interaction; (ii) the electron beams accelerated in the wake of the EM rings may cause damage to surrounding equipment (e.g., capillaries used for the laser pulse guiding) and become a source of unwanted EM radiation; and (iii) the knowledge of the origin of the EM and electron rings could serve as a diagnostic for determining the regimes of the laser-plasma interaction.

The paper is structured as follows. In Sec. II, we employ an analytical model to illustrate the radial evolution of the EM wave in the interaction with a Langmuir wave. In Sec. III, we present the setup and results of the 3D PIC simulation where the formation of the EM-electron rings is demonstrated. We also include the results of multi-parametric PIC study and describe the relationships among the EM ring properties and the parameters of laser and plasma. Finally, the results of this work are summarized and discussed in conclusion.

II. ELECTROMAGNETIC WAVE REFRACTION IN THE INTERACTION WITH LANGMUIR WAVE

First, we describe the distribution of electrons within the Langmuir wave. We assume that the plasma is cold and the ions are immobile. The continuity equation for the electron density n_e in one spatial dimension x and time t is

$$\frac{\partial n_e}{\partial t} + \frac{\partial}{\partial x}(n_e v_e) = 0, \quad (1)$$

where v_e is the electron velocity. We solve Eq. (1) using the quasistatic approximation, i.e., we make a mathematical transformation to the $\xi = x - v_{ph}t$ and $\tau = t$ coordinates, where v_{ph} is the phase velocity of the Langmuir wave, and neglect the $\partial/\partial\tau$ derivatives. We get

$$\frac{1}{n_e} \frac{\partial n_e}{\partial \xi} = \frac{1}{v_{ph} - v_e} \frac{\partial v_e}{\partial \xi}. \quad (2)$$

The solution of Eq. (2) is

$$n_e(\xi) = \frac{n_0 \beta_{ph}}{\beta_{ph} - \beta_e(\xi)}, \quad (3)$$

where n_0 is the electron density of ambient plasma, $\beta_{ph} = v_{ph}/c$, $\beta_e = v_e/c$, and c denotes the velocity of light in vacuum. When the denominator of Eq. (3) tends to zero, i.e., when the electron velocity approaches the phase velocity of the Langmuir wave, the electron density becomes infinite. This phenomenon is called the wave breaking. In what follows, we assume the Langmuir wave in the limit well below the wave breaking.

We consider that the Langmuir wave is generated by a given EM wave packet characterized by normalized vector potential $a = eE/m_e\omega c$, where E and ω are, respectively, the electric field and the angular frequency of the wave packet and m_e and $-e$ stand for the mass and charge of the electron, respectively. The distribution of the normalized electron velocity in the Langmuir wave can be approximated as $\beta_e \approx a_0^2 \cos(k_p \xi)/2$, where a_0 is the EM wave strength parameter, i.e., the peak amplitude of a in vacuum, and k_p is the

plasma wavenumber. Thus, the electron density distribution in the Langmuir wave is

$$n_e(\xi) = \frac{n_0 \beta_{ph}}{\beta_{ph} - a_0^2 \cos(k_p \xi)/2}. \quad (4)$$

This result can be generalized to the transverse direction r . As theoretically foreseen in Ref. 37 and later observed in a number of simulations and experiments,^{38–42} the density peaks of the Langmuir wave driven by a Gaussian pulse have the characteristic “horseshoe” shape and monotonically diminish with an increase in distance from the longitudinal axis. To take this into account, we extend Eq. (4) as follows:

$$n_e(\xi, r) = \frac{n_0 \beta_{ph}}{\beta_{ph} - a_0^2 \exp(-r^2/L^2) \cos(k_p \xi - r^2/L^2)/2}, \quad (5)$$

where L is the characteristic transverse size of the driver. The density distribution given by Eq. (5) for $a_0 = 0.6$, $\beta_{ph} = 0.95$ and $L = \lambda_p/2$, where $\lambda_p = 2\pi/k_p$ stands for the plasma wavelength, is shown in Fig. 1.

Second, we investigate the propagation of the EM wave packet (it can be, e.g., a rear part of the driver pulse or a separate “witness” pulse trailing behind the driver) in the plasma modulated by the Langmuir wave. The intensity of this EM wave packet is assumed to be low so that the plasma density given by Eq. (5) is unaffected by its propagation. Provided further that the wave packet is sufficiently short and its wavelength is small compared to the size of the Langmuir wave structures with which it interacts, its propagation can be described in the geometric optics approximation by examining the trajectories of particles (“photons”), each having a coordinate (ξ, r) and momentum (k_x, k_r) . The Hamiltonian for the photon interaction with the Langmuir wave is

$$\Omega(\xi, r, k_x, k_r) = \sqrt{k_x^2 + k_r^2 + n_e(\xi, r)} - \beta_{ph} k_x. \quad (6)$$

Here, k_x and k_r are measured in the units of ω/c and $n(\xi, r)$ is normalized by the critical plasma density $n_c = \sqrt{m_e \omega^2 / 4\pi e^2}$.

The trajectories of photons in plasma can be obtained by solving the set of Hamilton equations,

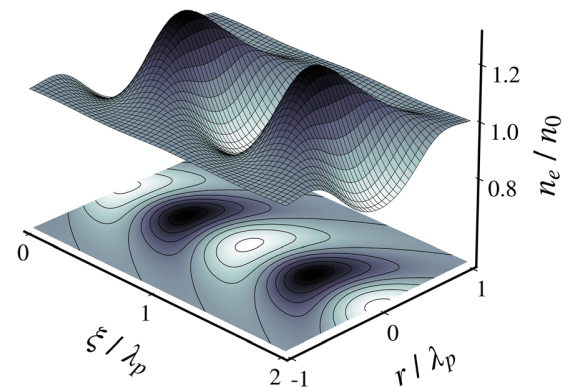


FIG. 1. Distribution of the normalized electron number density, n_e/n_0 , being perturbed by the action of the EM wave packet (i.e., the Langmuir wave) as described by Eq. (5) for $a_0 = 0.6$, $\beta_{ph} = 0.95$, and $L = \lambda_p/2$.

$$\begin{aligned} \frac{d\xi}{dt} &= \frac{k_x}{\sqrt{k_x^2 + k_r^2 + n_e(\xi, r)}} - \beta_{ph}, \\ \frac{dr}{d\xi} &= \frac{k_r}{k_x - \beta_{ph}\sqrt{k_x^2 + k_r^2 + n_e(\xi, r)}}, \\ \frac{dk_x}{d\xi} &= -\frac{1}{2} \frac{\partial n_e(\xi, r)}{\partial \xi} \frac{1}{k_x - \beta_{ph}\sqrt{k_x^2 + k_r^2 + n_e(\xi, r)}}, \\ \frac{dk_r}{d\xi} &= -\frac{1}{2} \frac{\partial n_e(\xi, r)}{\partial r} \frac{1}{k_x - \beta_{ph}\sqrt{k_x^2 + k_r^2 + n_e(\xi, r)}}. \end{aligned} \quad (7)$$

A numerical solution of the system of Eq. (7) for photons with several different initial values of r is displayed in Fig. 2. The photons initially propagate parallel to the Langmuir wave propagation direction with $k_x = 10$, whereas the Langmuir wave is described by Eq. (5) with $a_0 = 0.6$, $L = \lambda_p/2$, $n_0 = 0.01$, and $\beta_{ph} = 0.95$. The illustration shows that the trajectories of photons interacting with the Langmuir wave structures are curved toward and outward the propagation axis due to the changes in the plasma refractive index. In regions of electron density depressions (i.e., where $n_e/n_0 < 1$), the plasma enhances focusing. On the other hand, in regions of electron density peaks (i.e., where $n_e/n_0 > 1$), the plasma enhances defocusing. The focusing and defocusing of photons are, thus, induced by the excitation of the Langmuir wave. In addition, in the presence of plasma density gradients, the photons undergo energy (and, thus, the frequency) changes.^{43,44}

Since the plasma density profile and the initial photon distribution in Fig. 2 are axially symmetric, the defocused photons form a halo, which may in the high intensity limit evolve into an EM ring well separated from the axial part of the pulse (as shown in Sec. III). Provided that the EM ring contains a sufficient number of photons, it generates a secondary wakefield whose accelerating regions have

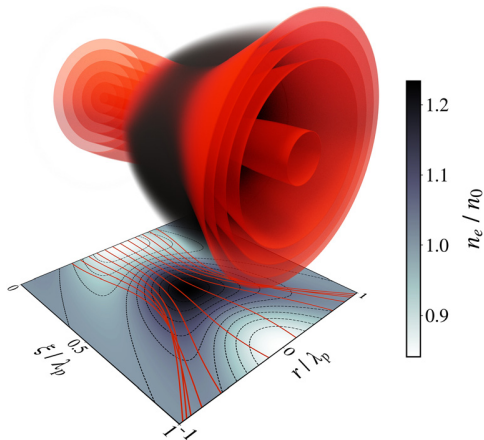


FIG. 2. Numerical solution of system of Eq. (7) showing the changes in the distribution of photons (reds) during their interaction with the Langmuir wave (grays). The photons, having several different initial values of r , initially propagate parallel to the Langmuir wave propagation direction (from left to right) with $k_x = 10$. The Langmuir wave is described by the parameters $a_0 = 0.6$, $L = \lambda_p/2$, $n_0 = 0.01$, and $\beta_{ph} = 0.95$. The projection at the bottom shows the photon trajectories (solid lines) and the normalized electron number density, n_e/n_0 , with its isolocountours (grays and dashed lines) in the (ξ, r) -plane.

toroidal shapes (similar to those driven by Laguerre-Gaussian pulses^{26,27}). The electrons accelerated in such a wakefield may subsequently form ring-shaped structures as well. Since the properties of the EM and electron rings depend on the parameters of the generated Langmuir wave, they can be controlled by tuning the parameters of the driver and plasma.

A somewhat more rigorous analysis on how the transverse non-uniformities affect the evolution of an EM wave as it interacts with a Langmuir wave can be found in Ref. 37, where the authors consider predominantly the induced focusing. Here, we follow up on this work by studying the process of induced defocusing. We employ a model based on the approximation of geometric optics, which qualitatively illustrates the origin and the initial stage of the higher order Gaussian modes formation. Further evolution of the EM wave, which has to be treated self-consistently, particularly in the nonlinear case, is addressed by the 3D PIC simulations in the following section.

III. PARTICLE-IN-CELL SIMULATIONS

A. Simulation setup

In order to study the EM-electron ring formation self-consistently, we carry out a PIC simulation in the 3D Cartesian geometry using the fully relativistic EPOCH⁴⁵ code. The driver laser pulse is characterized by the strength parameter $a_0 = 16$ and by the angular frequency $\omega_0 = 2\pi c/\lambda_0$, where λ_0 is its wavelength in vacuum. The driver has Gaussian temporal and spatial profiles with the full-with-at-half-maximum duration $\tau_0 = 12 T_0$, where $T_0 = \lambda_0/c$ is the cycle period of the driver, and the beam waist (a radius at $1/e^2$ of the peak intensity) $w_0 = 6\lambda_0$. The driver pulse, being linearly polarized along the z -axis, enters the simulation box from the left boundary and propagates parallel to the x -axis. Its focal spot is located at the distance of $500\lambda_0$ from the boundary along the propagation direction. The corresponding energy, peak power, and peak intensity of the driver are, respectively, $\mathcal{E}_0 \approx 6J \times \lambda_0(\mu\text{m})$, $P_0 \approx 200\text{ TW}$, and $I_0 \approx 3.5 \times 10^{20} \text{ W/cm}^2 \times [\lambda_0(\mu\text{m})]^{-2}$. The peak driver electric field amplitude in vacuum is $E_0 = m_e c \omega_0 a_0 / e \approx 0.5 \text{ TV/cm} \times [\lambda_0(\mu\text{m})]^{-1}$.

The driver pulse propagates in a pre-ionized homogeneous hydrogen plasma with the electron number density $n_e = 5 \times 10^{-3} n_c$. The critical power for self-focusing⁷ is, thus, $P_c \approx 17.4 \text{ GW} \times n_c/n_e \approx 3.5 \text{ TW}$. (The pulse peak power exceeds this value by a factor of ≈ 57 .) The threshold for the Langmuir wave breaking⁴⁶ (and equally the threshold for the electron self-injection) is $E_{wb} = E_p \sqrt{2(\gamma_w - 1)} \approx 11.6 \text{ GV/cm} \times [\lambda_0(\mu\text{m})]^{-1}$, where $E_p = m_e \omega_p c / e$, $\gamma_w \approx \omega_0 / \omega_p$ is the relativistic factor of the Langmuir wave, and $\omega_p = \sqrt{4\pi n_e e^2 / m_e}$ is the Langmuir frequency. The plasma is cold and collisionless, and the electrons and protons are represented by quasi-particles with triangular shape functions. The initial number of quasi-particles per grid cell is 2 for both particle species.

The simulation utilizes the moving window technique. The simulation window, having the longitudinal and transverse dimensions of $80\lambda_0$ and $150\lambda_0$, respectively, moves along the driver propagation direction at a velocity equal to c . The underlying Cartesian grid is uniform with the resolution of 20 and 10 cells per λ_0 along the driver propagation direction and the transverse directions, respectively. The simulation is evolved over the time interval of $1200 T_0$. The equations of motion for quasi-particles are solved using the Boris algorithm,⁴⁷ and the EM fields are calculated using the standard second-order

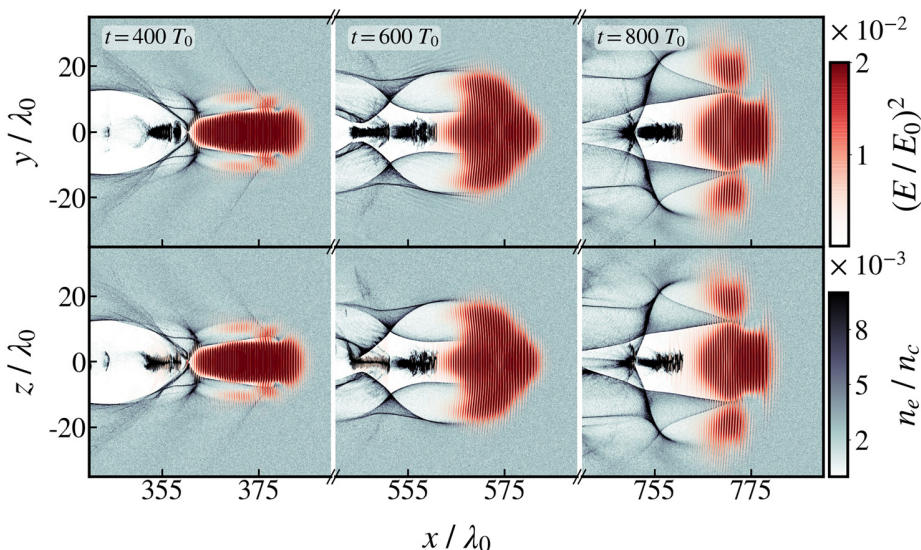


FIG. 3. Cross sections of the normalized driver field intensity, $(E/E_0)^2$, and the normalized electron number density, n_e/n_c , in the xy - and xz -planes at three successive instants of time obtained from the PIC simulation. The colorbars are saturated.

Yee solver⁴⁸ with the Courant -Friedrichs -Lowy (CFL) number⁴⁹ equal to 0.99. Absorbing boundary conditions are applied on each of the simulation domain sides for both the EM fields and particles.

B. Simulation results

The formation of the EM ring during the driver pulse propagation in plasma can be seen in Figs. 3 and 4. The relativistic self-focusing of the driver occurs as soon as it enters the plasma. Resulting tightly focused pulse ($t = 400 T_0$) reaches the peak amplitude of the normalized vector potential $a \approx 24.47$ (being $\approx 1.5 \times$ higher than a_0)

and pushes the plasma electrons not only along the laser axis, but also aside, creating a cavity void of electrons. At the same time, one may observe longitudinal wave breaking triggering the self-injection of electrons, part of which is being accelerated by the wakefield.

The cavity of the first Langmuir wave bucket is surrounded by a high-density electron sheath whose transverse size is smaller than the transverse size of the driver. Because of the strongly varying refractive index, a portion of the driver interacting with the inner surface of the cavity walls is focused toward the propagation axis forming a narrow density channel, which further guides the pulse. On the other hand, a portion of the driver interacting with the outer surface is pushed outward. This leads to a breakup of the driver into two distinct pulses ($t = 600 T_0$) according to the model presented in Sec. II. At $t = 800 T_0$, one can see that a ring of increased intensity encircling the axial part of the pulse is fully developed, whereas both parts are separated by a clear gap. A 3D representation of the driver field intensity and the electron density at $t = 1000 T_0$ is depicted in Fig. 4, where the EM ring is well visible.

Apart from the process of light defocusing induced by the plasma density variations described in Sec. II, the self-modulation instability (see, e.g., Refs. 50–52) may also contribute to the radial redistribution of the driver pulse energy. Its growth rate and other properties described in the literature may be applicable here as well. The self-modulation instability is closely related to Raman forward scattering, whose growth rate is⁵³

$$\Gamma_{\text{RFS}} = \frac{\omega_p^2 a_0}{\sqrt{8\omega_0(1 + a_0^2/2)}}. \quad (8)$$

For the parameters of the simulation, the characteristic time $t_{\text{RFS}} = 1/\Gamma_{\text{RFS}} \approx 726 T_0$ is comparable to the timescale of the ring development seen in the simulation.

Figure 5 shows the time evolution of the areal energy density of the EM field,

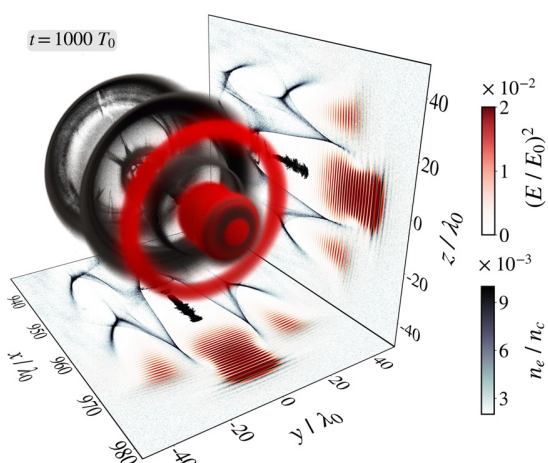


FIG. 4. 3D representation of the normalized driver field intensity, $(E/E_0)^2$, and the normalized electron number density, n_e/n_c , at the time $t = 1000 T_0$ obtained from the PIC simulation. Projections show the cross sections of the driver field intensity and the electron density in the xy - and xz -planes. The colorbars are saturated.

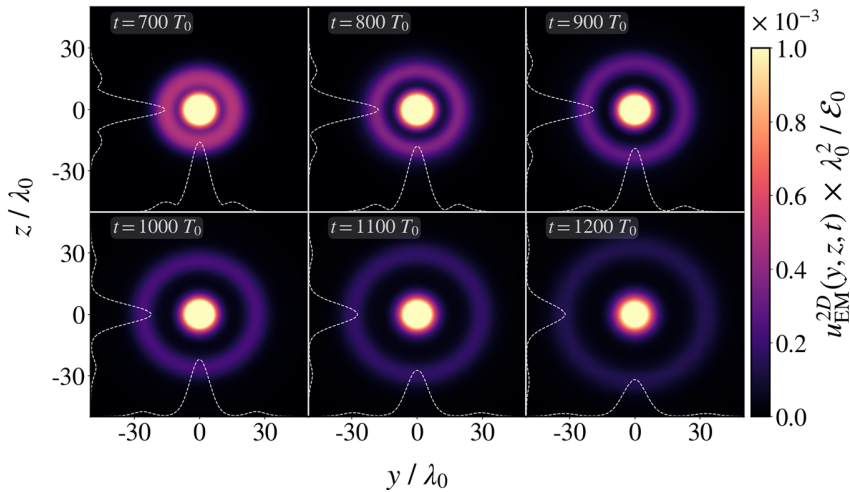


FIG. 5. The normalized areal energy density of the EM field, $u_{\text{EM}}^{2D}(y, z, t) \times \lambda_0^2 / \epsilon_0$, defined by Eq. (9) at six successive instants of time obtained from the PIC simulation. The white dashed lines show the line-outs of the EM field areal energy density along the y - and z -axes. The colorbar is saturated.

$$u_{\text{EM}}^{2D}(y, z, t) = \int_{-\infty}^{+\infty} u_{\text{EM}}(x, y, z, t) dx. \quad (9)$$

Here, $u_{\text{EM}} = (E^2 + B^2)/8\pi$ is the EM field energy density, where E and B are, respectively, the electric and magnetic fields of the driver pulse. As can be seen, the EM ring is azimuthally symmetric with no observable nonuniformities in the energy distribution. While the ring expands radially outward, the energy of the axial part of the driver pulse is well confined within a density channel formed along the propagation axis. The radius of the density channel at the end of the simulation ($t = 1200 T_0$) is $R \approx 16 \lambda_0$.

For the purposes of more quantitative analysis of the EM ring, we define the following variable:

$$u_{\text{EM}}^{1D}(r, t) = \oint_l u_{\text{EM}}^{2D}(y, z, t) dl, \quad (10)$$

where l is the circle of radius r in the yz -plane, i.e., $y^2 + z^2 = r^2$. The time evolution of u_{EM}^{1D} is displayed in Fig. 6. As can be seen, this quantity develops two peaks: the first one (closer to the origin) corresponds to the axial part of the pulse and the second one (farther from the origin) corresponds to the EM ring. We denote $r_0(t)$ as a radial coordinate of minimum between the two peaks and $r_1(t)$ as a radial coordinate of maximum of the second peak (see Fig. 6).

Using the quantities described above, we define the instantaneous total EM ring energy,

$$\mathcal{E}_r(t) = \int_{r_0(t)}^{+\infty} u_{\text{EM}}^{1D}(r, t) dr, \quad (11)$$

and the instantaneous EM ring opening angle,

$$\theta_r(t) = 2 \arcsin \left(\frac{1}{v_g(t)} \frac{dr_1(t)}{dt} \right), \quad (12)$$

where $v_g(t)$ is the group velocity of the driver pulse. The time dependence of the quantities defined by Eqs. (11) and (12) is relatively weak within the timescale of the simulation; thus, in what follows, we consider the total EM ring energy, \mathcal{E}_r , and the EM ring opening angle, θ_r .

to be the time-averaged values of $\mathcal{E}_r(t)$ and $\theta_r(t)$, respectively. Using these definitions, we find that $\mathcal{E}_r \approx 3.36 J \times \lambda_0 (\mu m)$ (which accounts for 56% of the initial total driver pulse energy) and $\theta_r \approx 68$ mrad.

The accelerating regions of the wakefield left behind the EM ring are of toroidal shapes. The peak normalized vector potential of the EM ring decreases in time; it reaches $a \approx 3.97$ at the moment of detachment of the EM ring from the axial part of the driver ($t = 650 T_0$) and drops to $a \approx 1.74$ at the end of the simulation ($t = 1200 T_0$) mostly due to the EM ring radial expansion. The peak amplitude of the wakefield generated by the EM ring is less than E_{wb} and, thus, the self-injection of electrons does not occur. Figure 7 shows the time evolution of the areal kinetic energy density of electrons,

$$u_e^{2D}(y, z, t) = \int_{-\infty}^{+\infty} u_e(x, y, z, t) dx. \quad (13)$$

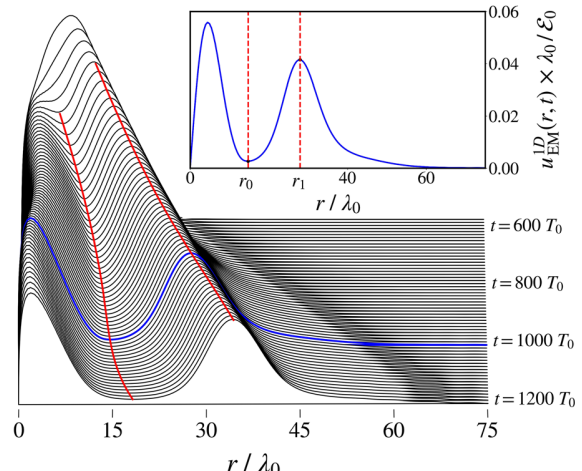


FIG. 6. The time evolution of $u_{\text{EM}}^{1D}(r, t) \times \lambda_0^2 / \epsilon_0$ defined by Eq. (10) obtained from the PIC simulation. The inset shows $u_{\text{EM}}^{1D}(r, t) \times \lambda_0^2 / \epsilon_0$ at $t = 1000 T_0$. The red lines mark r_0 and r_1 as defined in text.

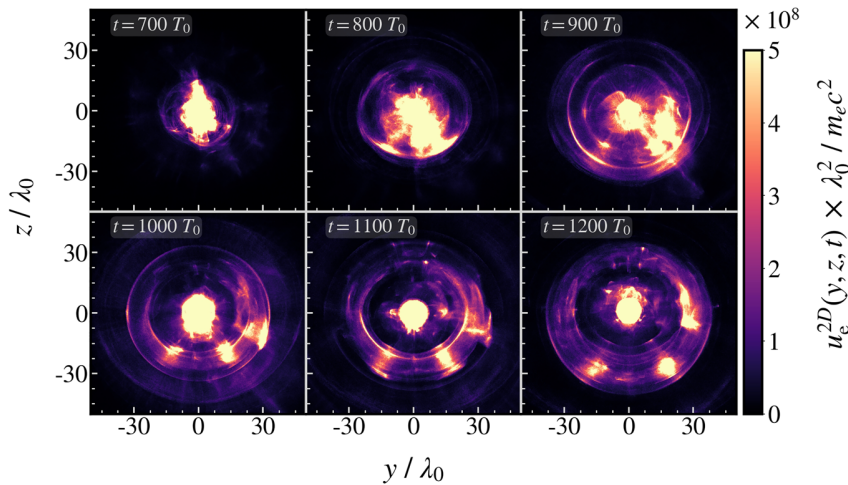


FIG. 7. The normalized areal kinetic energy density of electrons, $u_e^{2D}(y, z, t) \times \lambda_0^2 / m_e c^2$, defined by Eq. (13) at six successive instants of time obtained from the PIC simulation. The colorbar is saturated.

Here, u_e is the density of the electron kinetic energy $\mathcal{E}_e = m_e c^2 (\gamma_e - 1)$, where γ_e is the relativistic factor of electrons. Although the EM ring does not trigger the self-injection, we may observe an increased electron energy density along a ring encircling the axial electron beam; it consists of a lower energy density ring segments and unevenly distributed spots of local energy density enhancements. Resulting ring-shaped electron beam inherits the opening angle from the EM ring.

The spots of higher electron energy density emerge in certain prominent directions with respect to the driver propagation axis. In order to unveil the origin of their formation, in Fig. 8, we plot the cross sections of the electron energy density together with the electron number density and the longitudinal electric field in the xh -plane, where h is a line in the yz -plane along which one of the spots appears. As the figure indicates, the spots of higher energy density are formed by the

electrons injected into the second period of the Langmuir wave. They exhibit a spiral motion ($t = 600 T_0$) due to the focusing forces of the wakefield and a nonzero transverse momentum of electrons at the moment of injection. Later on ($t = 800 T_0$), a large fraction of these electrons is dragged into the secondary wakefield generated by the EM ring. The direction of the drag is determined by the instantaneous position of the electrons on the spiral at the moment of the EM ring detachment from the driver.

On the other hand, the lower energy density ring segments are formed by the electrons injected into the first period of the Langmuir wave. When the EM ring detaches from the driver, the energy of the axial part of the pulse drops and the wake structure shrinks longitudinally ($t = 700 T_0$). The electrons from the rear part of the beam consequently find themselves in the defocusing and decelerating

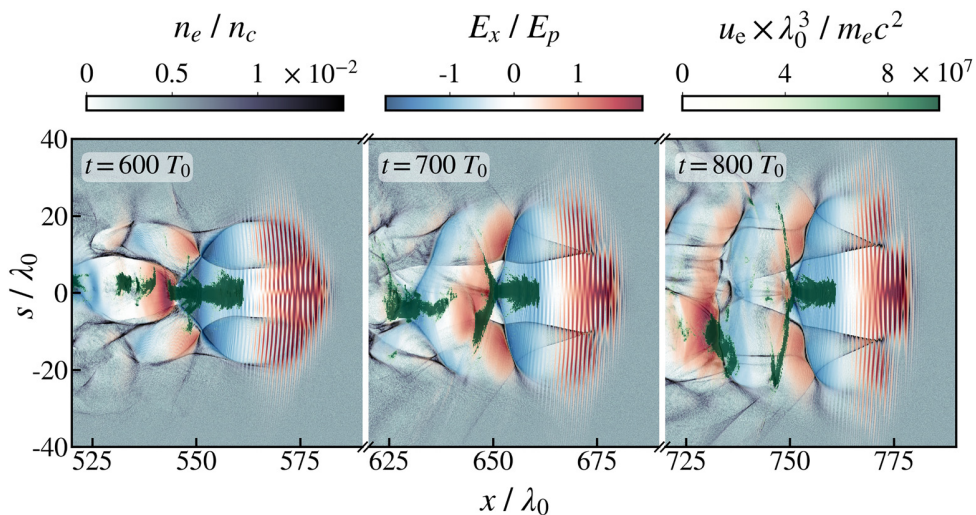


FIG. 8. Cross sections of the normalized electron number density, n_e / n_c , the normalized longitudinal electric field, E_x / E_p , and the normalized kinetic energy density of electrons, $u_e \times \lambda_0^3 / m_e c^2$, in the xh -plane at three successive instant of time obtained from the PIC simulation, where h is a line in the yz -plane defined using parameter s as $y = s \cos \varphi$, $z = s \sin \varphi$ with $\varphi = 2.27$ rad. The colorbars are saturated.

region of the wakefield. These electrons are then as well directed into the second period of the secondary wakefield generated by the EM ring. However, their distribution is much more azimuthally uniform.

The energy spectra of the electrons located in the region defined by $r \leq r_0(t)$ (i.e., the electrons in the vicinity of the driver propagation axis) and of the electrons located in the region defined by $r > r_0(t)$ (i.e., the electrons at the periphery) at the end of the simulation ($t = 1200 T_0$) are shown in Fig. 9. They reveal that the axial electron beam possesses a relatively broad energy peak at ≈ 130 MeV on the background of quasi-thermal spectrum. As far as the ring-shaped electron beam is concerned, one can distinguish peaks around ≈ 25 MeV and ≈ 50 MeV corresponding, respectively, to the populations of electrons forming the lower energy density ring segments and the higher energy density spots. The charge of electrons having the kinetic energy > 10 MeV in the vicinity of the driver propagation axis and at the periphery is, respectively, ≈ 4.36 nC and ≈ 1.68 nC. The ring electrons, thus, carry up to 28% of the total electron beam charge.

We emphasize that the purpose of the electron analysis above is solely to show that the EM ring can become a source of ring-shaped high-energy electron beams. In this work, no effort has been made in order to optimize the parameters of the electron beams for specific applications. Regarding the optimization and tuning of the electron beam parameters, the reader can refer to the theory of laser-wakefield acceleration.^{1,2} Furthermore, we note that the emissions of the electron ring patterns from the laser-plasma interaction have been also reported in other works and several different mechanisms of their origin have been identified (see, e.g., Refs. 35 and 54–60).

C. Multi-parametric study

In order to find out whether the properties of the generated EM rings are sensitive to changes in the parameters of laser and plasma and, if so, to explain the relationships among them, we carry out a multi-parametric PIC study. We perform numerous 3D PIC simulations where we vary the values of the ambient plasma electron density, n_0 , the laser strength parameter, a_0 , and the laser beam waist, w_0 . All other simulation parameters remain the same as for the simulation described in Sec. III A except for the Cartesian grid resolution and the number of quasi-particles per grid cell. In order to reduce the

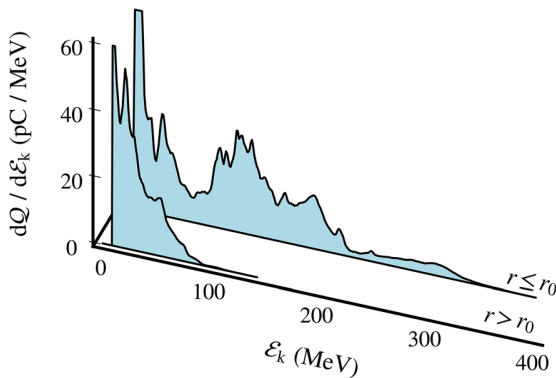


FIG. 9. Energy spectra of the electrons located in the region defined by $r \leq r_0(t)$ and in the region defined by $r > r_0(t)$ at the end of the PIC simulation ($t = 1200 T_0$).

computational demands of the simulations, the grid resolution is twice as low and the number of quasi-particles per grid cell for both particle species is set to 1. We ensured, however, that such a simulation setup is justified by performing several simulations with higher resolution and number of quasi-particles that resulted in negligible differences in the properties of interest of the EM rings.

First, we compare the results of simulations where solely the laser strength parameter is varied. Figure 10 shows the quantity u_{EM}^{1D} defined by Eq. (10) for a_0 ranging from 4 to 20. It can be clearly seen that the portion of the energy leakage from the laser pulse increases with a_0 until it saturates at certain value. While for $a_0 \geq 6$, the leaked part of the pulse forms a distinct EM ring separated from the axial pulse by a clear gap, for $a_0 < 6$, we observe rather a broad low intensity halo instead of the EM ring, which is in accordance with the analytical model introduced in Sec. II. The onset of the EM ring formation occurs when the power of the leaked part of the pulse exceeds the critical power for self-guiding in plasma. In the studied case, this corresponds to a_0 somewhere between 4 and 6 (or to P_0/P_c in the range from 3.5 to 8). For $a_0 \leq 2$, the self-focusing of the laser pulse does not happen, and, consequently, the energy leakage is negligible. For this reason, we do not include the results here.

The dependence of the ratio of the total EM ring energy to the total initial driver pulse energy and the EM ring opening angle on the laser strength parameter is shown in Fig. 11. We note that since for $a_0 < 6$ the EM rings do not occur, we cannot include their attributes in this comparison. Figure 11 reveals that the portion of energy in the EM ring grows with a_0 until it saturates at $\approx 57\%$ of \mathcal{E}_0 for $a_0 \geq 16$. This growth can be explained by the fact that stronger driver yields steeper electron density gradients, which then defocus the interacting parts of the pulse more effectively. On the contrary, the opening angle decreases with a_0 , from ≈ 100 mrad for $a_0 = 6$ to ≈ 63 mrad for $a_0 = 20$. As one can see from Fig. 12, the opening angle of the EM ring correlates with the elongation of the ion cavity and the surrounding electron wall. The larger the elongation of the cavity, the smaller the opening angle of the EM ring.

Second, we compare the results of simulations where the laser strength parameter is varied alongside the laser beam waist and the electron density. Figure 13 shows the dependence of $\mathcal{E}_r/\mathcal{E}_0$ and θ_r on n_0 , a_0 , and w_0 , where a_0 is varied from 14 to 18, n_0 is varied from

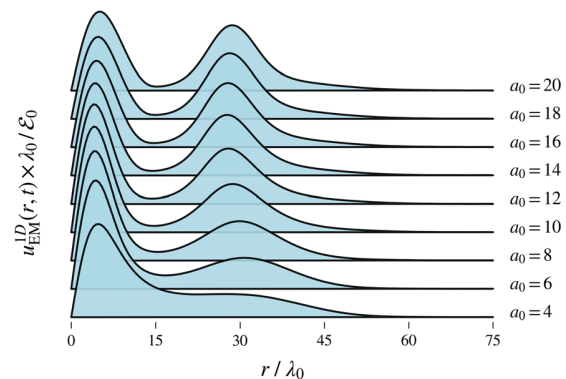


FIG. 10. The quantity $u_{EM}^{1D}(r, t) \times \lambda_0^2 / \mathcal{E}_0$ defined by Eq. (10) for several different laser strength parameters, a_0 , at $t = 1000 T_0$ obtained from the PIC simulations.

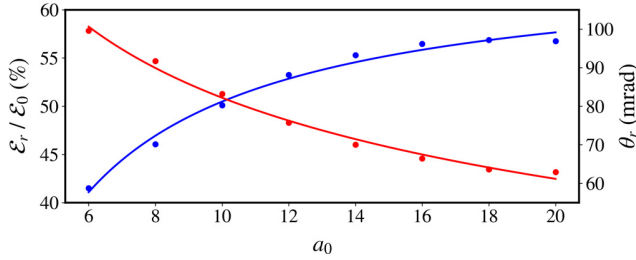


FIG. 11. The ratio of the total EM ring energy to the total initial driver pulse energy, $\mathcal{E}_r/\mathcal{E}_0$, (blue) and the EM ring opening angle, θ_r , (red) for several different laser strength parameters, a_0 . The dots mark the values obtained from the PIC simulations, and the lines are curves fitting the data.

0.4 % of n_c to 0.6 % of n_c , and w_0 is varied from $4\lambda_0$ to $8\lambda_0$. Within the studied parameter range, we see that both $\mathcal{E}_r/\mathcal{E}_0$ and θ_r increase strongly with the decrease in the driver beam waist. The portions of energy carried off by the EM rings vary from ≈ 45 to ≈ 49 % of \mathcal{E}_0 for $w_0 = 8\lambda_0$, from ≈ 55 to ≈ 58 % of \mathcal{E}_0 for $w_0 = 6\lambda_0$, and from ≈ 65 to ≈ 68 % of \mathcal{E}_0 for $w_0 = 4\lambda_0$. The opening angles of the EM rings vary from ≈ 47 to ≈ 60 mrad for $w_0 = 8\lambda_0$, from ≈ 58 to ≈ 73 mrad for $w_0 = 6\lambda_0$, and from ≈ 85 to ≈ 115 mrad for $w_0 = 4\lambda_0$.

For a fixed driver beam waist, the dependence of $\mathcal{E}_r/\mathcal{E}_0$ and θ_r on the electron density and the laser strength parameter is more complex. In the case of $w_0 = 8\lambda_0$, we observe that the value of $\mathcal{E}_r/\mathcal{E}_0$ depends predominantly on the electron density, both quantities being inversely proportional to each other. On the contrary, when $w_0 = 4\lambda_0$, the value of $\mathcal{E}_r/\mathcal{E}_0$ depends mainly on a_0 and the proportionality is direct. As for the opening angle of the EM ring, it is inversely proportional to both a_0 and n_0 or, equivalently, inversely proportional to the ratio between the driver pulse peak power and the critical power for self-focusing, P_0/P_c , regardless the value of w_0 . The relationships between the EM ring properties and the parameters of laser and plasma can be again explained (from the most part) by the dynamical evolution of the Langmuir wave, particularly the shape and steepness of its density peaks, excited by the driver pulse.

The results of the multi-parametric study reveal that the EM rings are present in a relatively broad range of studied cases (always

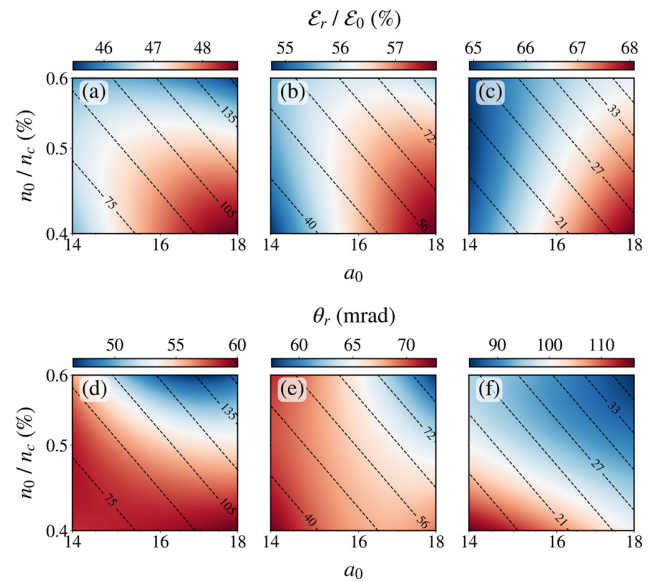


FIG. 13. The ratio of the total EM ring energy to the total initial driver pulse energy, $\mathcal{E}_r/\mathcal{E}_0$, dependence on the normalized ambient plasma electron density, n_0/n_c , the laser strength parameter, a_0 , and the laser beam waist: (a) $w_0 = 8\lambda_0$, (b) $w_0 = 6\lambda_0$, and (c) $w_0 = 4\lambda_0$. The EM ring opening angle, θ_r , dependence on the normalized ambient plasma electron density, n_0/n_c , the laser strength parameter, a_0 , and the laser beam waist: (d) $w_0 = 8\lambda_0$, (e) $w_0 = 6\lambda_0$, and (f) $w_0 = 4\lambda_0$. The scattered data obtained from the PIC simulations are interpolated using the radial basis function interpolation with Gaussian kernel and the shape parameter $\varepsilon = 10$. The black dashed lines are the isocontours of the ratio between the driver pulse peak power and the critical power for self-focusing, P_0/P_c .

together with the axial part of the pulse). This fact indicates that the EM rings are rather robust nonlinear EM objects. Furthermore, all the EM rings exhibit surprisingly high azimuthal symmetry, with very weak sensitivity to the laser polarization. It is known, however, that the ring modes are unstable to azimuthal perturbations. Their stability against symmetric and asymmetric azimuthal perturbations have been investigated in detail in Ref. 23. Finally, this multi-parametric study

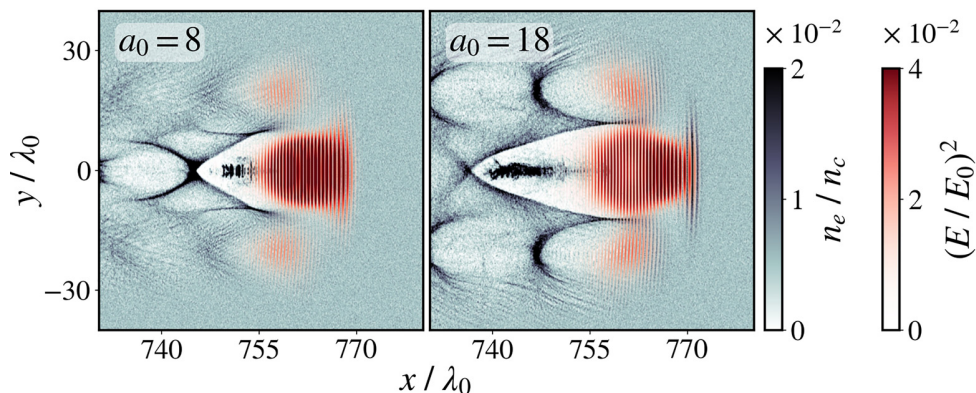


FIG. 12. Cross sections of the normalized driver field intensity, $(E/E_0)^2$, and the normalized electron density, n_e/n_c , in the xy -plane for $a_0 = 8$ ($\theta_r \approx 93.8$ mrad) and $a_0 = 18$ ($\theta_r \approx 66.1$ mrad) at $t = 800 T_0$ obtained from the PIC simulations. The colorbars are saturated.

verifies that the properties of the EM rings (and consequently the properties of the ring-shaped electron beams) can be controlled by tuning the parameters of the laser and plasma.

IV. CONCLUSION

In this paper, we investigate the interaction of Langmuir waves with driving laser pulses as they co-propagate in underdense plasma. We observe the formation of ring-shaped EM-electron structures, where the EM rings arise from the laser pulse defocusing induced by the excitation of Langmuir waves in underdense plasma, and the ring-shaped electron beams are formed and accelerated subsequently by the secondary toroidal wakefields generated by the EM rings. The underlying physical process of laser radiation defocusing by the electron density modulations in the Langmuir wave is illustrated using an analytical model based on the geometric optics approximation and demonstrated by a 3D PIC simulation. A multi-parametric PIC study further reveals that the EM rings are relatively robust nonlinear objects, whose properties can be controlled by tuning the parameters of laser and plasma. Within the studied parameter range, we find that up to $\approx 70\%$ of the total initial driver pulse energy can be carried off by the EM rings having the opening angles $\approx 45\text{--}115$ mrad.

The results obtained are important in the sense that the generated EM ring structures may carry off a significant fraction of energy from the driver and, thus, limit the overall efficiency of applications based on the laser-plasma interaction. Furthermore, the relatively wide-angle electron beams accelerated in the wake of the EM rings may cause a damage to surrounding equipment and become a source of unwanted EM radiation. Finally, the understanding of the EM-electron ring origins could serve as a diagnostics for determining the regimes of laser-plasma interaction and contribute to the development of numerous practical applications.^{26–36}

ACKNOWLEDGMENTS

This work was supported by the projects “High Field Initiative” (Grant No. CZ.02.1.01/0.0/0.0/15_003/0000449) from the European Regional Development Fund and “e-INFRA CZ” (ID:90140) from the Ministry of Education, Youth and Sports of the Czech Republic. The EPOCH code was in part funded by the UK EPSRC Grant Nos. EP/G054950/1, EP/G056803/1, EP/G055165/1, and EP/M022463/1.

AUTHOR DECLARATIONS

Conflict of Interest

The authors have no conflicts of interest to disclose.

DATA AVAILABILITY

The data that support the findings of this study are openly available in a Zenodo repository titled “On the electromagnetic-electron rings originating from the interaction of high-power short-pulse laser and underdense plasma” at <https://doi.org/10.5281/zenodo.5711101>.

REFERENCES

- ¹T. Tajima and J. M. Dawson, *Phys. Rev. Lett.* **43**, 267 (1979).
- ²E. Esarey, C. B. Schroeder, and W. P. Leemans, *Rev. Mod. Phys.* **81**, 1229 (2009).
- ³A. J. Gonsalves, K. Nakamura, J. Daniels, C. Benedetti, C. Pieronek, T. C. De Raadt, S. Steinke, J. H. Bin, S. S. Bulanov, J. Van Tilborg, C. G. Geddes, C. B. Schroeder, C. Tóth, E. Esarey, K. Swanson, L. Fan-Chiang, G. Bagdasarov, N. Bobrova, V. Gasilov, G. Korn, P. Sasorov, and W. P. Leemans, *Phys. Rev. Lett.* **122**, 084801 (2019).
- ⁴S. V. Bulanov, T. Z. Esirkepov, M. Kando, A. S. Pirozhkov, and N. N. Rosanov, *Phys.-Usp.* **56**, 429 (2013).
- ⁵A. S. Pirozhkov, M. Kando, T. Z. Esirkepov, P. Gallegos, H. Ahmed, E. N. Ragozin, A. Y. Faenov, T. A. Pikuz, T. Kawachi, A. Sagisaka, J. K. Koga, M. Courty, J. Green, P. Foster, C. Brenner, B. Dromey, D. R. Symes, M. Mori, K. Kawase, T. Kameshima, Y. Fukuda, L. Chen, I. Daito, K. Ogura, Y. Hayashi, H. Kotaki, H. Kiriyama, H. Okada, N. Nishimori, T. Imazono, K. Kondo, T. Kimura, T. Tajima, H. Daido, P. Rajeev, P. McKenna, M. Borghesi, D. Neely, Y. Kato, and S. V. Bulanov, *Phys. Rev. Lett.* **108**, 135004 (2012).
- ⁶M. Tabak, J. Hammer, M. E. Glinsky, W. L. Krueer, S. C. Wilks, J. Woodworth, E. M. Campbell, M. D. Perry, and R. J. Mason, *Phys. Plasmas* **1**, 1626 (1994).
- ⁷G.-Z. Sun, E. Ott, Y. C. Lee, and P. Guzdar, *Phys. Fluids* **30**, 526 (1987).
- ⁸P. Monot, T. Auguste, P. Gibbon, F. Jakober, G. Mainfray, A. Dulieu, M. Louis-Jacquet, G. Malka, and J. L. Miquel, *Phys. Rev. Lett.* **74**, 2953 (1995).
- ⁹P. E. Young and P. R. Bolton, *Phys. Rev. Lett.* **77**, 4556 (1996).
- ¹⁰N. M. Naumova, S. V. Bulanov, K. Nishihara, T. Z. Esirkepov, and F. Pegoraro, *Phys. Rev. E* **65**, 045402(R) (2002).
- ¹¹T. Z. Esirkepov, F. F. Kamenets, S. V. Bulanov, and N. M. Naumova, *JETP Lett.* **68**, 36 (1998).
- ¹²S. V. Bulanov, T. Z. Esirkepov, N. M. Naumova, and V. A. Vshivkov, *Phys. Rev. Lett.* **82**, 3440 (1999).
- ¹³D. Farina and S. V. Bulanov, *Phys. Rev. Lett.* **86**, 5289 (2001).
- ¹⁴T. Z. Esirkepov, K. Nishihara, S. V. Bulanov, and F. Pegoraro, *Phys. Rev. Lett.* **89**, 275002 (2002).
- ¹⁵S. V. Bulanov, M. Lontano, T. Z. Esirkepov, F. Pegoraro, and A. M. Pukhov, *Phys. Rev. Lett.* **76**, 3562 (1996).
- ¹⁶D. N. Yue, M. Chen, P. F. Geng, X. H. Yuan, S. M. Weng, S. S. Bulanov, S. V. Bulanov, K. Mima, Z. M. Sheng, and J. Zhang, *Phys. Plasmas* **28**, 042303 (2021).
- ¹⁷W. B. Mori, C. Joshi, J. M. Dawson, D. W. Forslund, and J. M. Kindel, *Phys. Rev. Lett.* **60**, 1298 (1988).
- ¹⁸B. I. Cohen, B. F. Lasinski, A. B. Langdon, and J. C. Cummings, *Phys. Fluids B* **3**, 766 (1991).
- ¹⁹A. B. Borisov, A. V. Borovskiy, O. B. Shiryaev, V. V. Korobkin, A. M. Prokhorov, J. C. Solem, T. S. Luk, K. Boyer, and C. K. Rhodes, *Phys. Rev. A* **45**, 5830 (1992).
- ²⁰K. Krushelnick, A. Ting, C. I. Moore, H. R. Burris, E. Esarey, P. Sprangle, and M. Baine, *Phys. Rev. Lett.* **78**, 4047 (1997).
- ²¹F. Cattani, A. Kim, D. Anderson, and M. Lisak, *Phys. Rev. E* **64**, 016412 (2001).
- ²²A. Kim, M. Tushentsov, F. Cattani, D. Anderson, and M. Lisak, *Phys. Rev. E* **65**, 036416 (2002).
- ²³N. Naseri, W. Rozmus, and D. Pesme, *Phys. Plasmas* **23**, 113101 (2016).
- ²⁴V. F. Kovalev and V. Y. Bychenkov, *Phys. Rev. E* **99**, 043201 (2019).
- ²⁵P. Valenta, G. M. Grittani, C. M. Lazzarini, O. Klimo, and S. V. Bulanov, in *Laser Acceleration of Electrons, Protons, and Ions VI*, edited by S. S. Bulanov, J. Schreiber, and C. B. Schroeder (International Society for Optics and Photonics, SPIE, 2021), Vol. 11779, p. 1177909.
- ²⁶P. Michel, E. Esarey, C. B. Schroeder, B. A. Shadwick, and W. P. Leemans, *Phys. Plasmas* **13**, 113112 (2006).
- ²⁷J. Vieira and J. T. Mendonça, *Phys. Rev. Lett.* **112**, 215001 (2014).
- ²⁸G. B. Zhang, M. Chen, C. B. Schroeder, J. Luo, M. Zeng, F. Y. Li, L. L. Yu, S. M. Weng, Y. Y. Ma, T. P. Yu, Z. M. Sheng, and E. Esarey, *Phys. Plasmas* **23**, 033114 (2016).
- ²⁹Z. Y. Xu, C. F. Xiao, H. Y. Lu, R. H. Hu, J. Q. Yu, Z. Gong, Y. R. Shou, J. X. Liu, C. Z. Xie, S. Y. Chen, H. G. Lu, T. Q. Xu, R. X. Li, N. Hafz, S. Li, Z. Najmudin, P. P. Rajeev, D. Neely, and X. Q. Yan, *Phys. Rev. Accel. Beams* **23**, 091301 (2020).
- ³⁰X. Zhang, B. Shen, L. Zhang, J. Xu, X. Wang, W. Wang, L. Yi, and Y. Shi, *New J. Phys.* **16**, 123051 (2014).
- ³¹C. Brabetz, S. Busold, T. Cowan, O. Deppert, D. Jahn, O. Kester, M. Roth, D. Schumacher, and V. Bagnoud, *Phys. Plasmas* **22**, 013105 (2015).
- ³²W. P. Wang, C. Jiang, H. Dong, X. M. Lu, J. F. Li, R. J. Xu, Y. J. Sun, L. H. Yu, Z. Guo, X. Y. Liang, Y. X. Leng, R. X. Li, and Z. Z. Xu, *Phys. Rev. Lett.* **125**, 034801 (2020).
- ³³N. Jain, T. M. Antonsen, and J. P. Palastro, *Phys. Rev. Lett.* **115**, 195001 (2015).

- ³⁴N. Jain, *Phys. Plasmas* **26**, 023107 (2019).
- ³⁵T. Z. Zhao, K. Behm, C. F. Dong, X. Davoine, S. Y. Kalmykov, V. Petrov, V. Chvykov, P. Cummings, B. Hou, A. Maksimchuk, J. A. Nees, V. Yanovsky, A. G. Thomas, and K. Krushelnick, *Phys. Rev. Lett.* **117**, 094801 (2016).
- ³⁶G. Stancari, A. Valishev, G. Annala, G. Kuznetsov, V. Shiltsev, D. A. Still, and L. G. Vorobiev, *Phys. Rev. Lett.* **107**, 084802 (2011).
- ³⁷S. V. Bulanov and A. S. Sakharov, *JETP Lett.* **54**, 203 (1991).
- ³⁸S. V. Bulanov, F. Pegoraro, and A. M. Pukhov, *Phys. Rev. Lett.* **74**, 710 (1995).
- ³⁹B. A. Shadwick, G. M. Tarkenton, E. H. Esarey, and W. P. Leemans, *IEEE Trans. Plasma Sci.* **30**, 38 (2002).
- ⁴⁰N. H. Matlis, S. Reed, S. S. Bulanov, V. Chvykov, G. Kalintchenko, T. Matsuoka, P. Rousseau, V. Yanovsky, A. Maksimchuk, S. Kalmykov, G. Shvets, and M. C. Downer, *Nat. Phys.* **2**, 749 (2006).
- ⁴¹A. Maksimchuk, S. Reed, S. S. Bulanov, V. Chvykov, G. Kalintchenko, T. Matsuoka, C. McGuffey, G. Mourou, N. Naumova, J. Nees, P. Rousseau, V. Yanovsky, K. Krushelnick, N. H. Matlis, S. Kalmykov, G. Shvets, M. C. Downer, C. R. Vane, J. R. Beene, D. Stracener, and D. R. Schultz, *Phys. Plasmas* **15**, 056703 (2008).
- ⁴²M. C. Downer, R. Zgadzaj, A. Debus, U. Schramm, and M. C. Kaluza, *Rev. Mod. Phys.* **90**, 035002 (2018).
- ⁴³S. C. Wilks, J. M. Dawson, W. B. Mori, T. Katsouleas, and M. E. Jones, *Phys. Rev. Lett.* **62**, 2600 (1989).
- ⁴⁴T. Z. Esirkepov, S. V. Bulanov, M. Yamagiwa, and T. Tajima, *Phys. Rev. Lett.* **96**, 014803 (2006).
- ⁴⁵T. D. Arber, K. Bennett, C. S. Brady, A. Lawrence-Douglas, M. G. Ramsay, N. J. Sircombe, P. Gillies, R. G. Evans, H. Schmitz, A. R. Bell, and C. P. Ridgers, *Plasma Phys. Controlled Fusion* **57**, 113001 (2015).
- ⁴⁶A. Akhiezer and R. Polovin, Sov. Phys. JETP **3**, 696 (1956).
- ⁴⁷J. P. Boris, in *Proceedings of the Fourth Conference on Numerical Simulation of Plasmas* (Office of Naval Research, Arlington, VA, 1971), pp. 3–67.
- ⁴⁸K. S. Yee, IEEE Trans. Antennas Propag. **14**, 302 (1966).
- ⁴⁹R. Courant, K. Friedrichs, and H. Lewy, *Math. Ann.* **100**, 32 (1928).
- ⁵⁰T. M. Antonsen and P. Mora, *Phys. Rev. Lett.* **69**, 2204 (1992).
- ⁵¹P. Sprangle, E. Esarey, J. Krall, and G. Joyce, *Phys. Rev. Lett.* **69**, 2200 (1992).
- ⁵²N. Andreev, L. Gorbunov, V. Kirsanov, A. Pogosova, R. Ramazashvili, and D. Parsons, *JETP Lett.* **55**, 571 (1992).
- ⁵³W. B. Mori, C. D. Decker, D. E. Hinkel, and T. Katsouleas, *Phys. Rev. Lett.* **72**, 1482 (1994).
- ⁵⁴D. Kaganovich, D. F. Gordon, and A. Ting, *Phys. Rev. Lett.* **100**, 215002 (2008).
- ⁵⁵L. Zhang, L. M. Chen, W. M. Wang, W. C. Yan, D. W. Yuan, J. Y. Mao, Z. H. Wang, C. Liu, Z. W. Shen, A. Faenov, T. Pikuz, D. Z. Li, Y. T. Li, Q. L. Dong, X. Lu, J. L. Ma, Z. Y. Wei, Z. M. Sheng, and J. Zhang, *Appl. Phys. Lett.* **100**, 014104 (2012).
- ⁵⁶B. B. Pollock, F. S. Tsung, F. Albert, J. L. Shaw, C. E. Clayton, A. Davidson, N. Lemos, K. A. Marsh, A. Pak, J. E. Ralph, W. B. Mori, and C. Joshi, *Phys. Rev. Lett.* **115**, 055004 (2015).
- ⁵⁷X. Yang, E. Brunetti, D. R. Gil, G. H. Welsh, F. Y. Li, S. Cipiccia, B. Ersfeld, D. W. Grant, P. A. Grant, M. R. Islam, M. P. Tooley, G. Vieux, S. M. Wiggins, Z. M. Sheng, and D. A. Jaroszynski, *Sci. Rep.* **7**, 43910 (2017).
- ⁵⁸E. Brunetti, X. Yang, F. Y. Li, D. Reboredo Gil, G. H. Welsh, S. Cipiccia, B. Ersfeld, D. W. Grant, P. A. Grant, M. R. Islam, M. Shahzad, M. P. Tooley, G. Vieux, S. M. Wiggins, Z. M. Sheng, and D. A. Jaroszynski, in *Laser Acceleration of Electrons, Protons, and Ions IV*, edited by E. Esarey, C. B. Schroeder, and F. J. Grüner (International Society for Optics and Photonics, SPIE, 2017), Vol. 10240, p. 102400P.
- ⁵⁹K. Behm, A. Hussein, T. Z. Zhao, S. Dann, B. X. Hou, V. Yanovsky, J. Nees, A. Maksimchuk, W. Schumaker, A. G. Thomas, and K. Krushelnick, *Plasma Phys. Controlled Fusion* **61**, 065012 (2019).
- ⁶⁰F. Salehi, M. Le, L. Railing, M. Kolesik, and H. M. Milchberg, *Phys. Rev. X* **11**, 021055 (2021).

B.2 Polarity reversal of wakefields driven by ultrashort pulse laser

The following article is reproduced from Valenta, P., Esirkepov, T. Z., Koga, J. K., Nečas, A., Grittani, G. M., Lazzarini, C. M., Klimo, O., Korn, G., and Bulanov, S. V. (2020). [Polarity reversal of wakefields driven by ultrashort pulse laser](#). *Physical Review E*, **102**(5):053216, with the permission of APS.

Copyright © 2020 American Physical Society.

Polarity reversal of wakefields driven by ultrashort pulse laser

P. Valenta^{1,2,*}, T. Zh. Esirkepov^{1,3}, J. K. Koga^{1,3}, A. Nečas⁴, G. M. Grittani¹, C. M. Lazzarini¹, O. Klimo^{1,2}, G. Korn¹, and S. V. Bulanov^{1,3}

¹ELI Beamlines, Institute of Physics of the Czech Academy of Sciences, Na Slovance 2, Prague 18221, Czech Republic

²Faculty of Nuclear Sciences and Physical Engineering, Czech Technical University in Prague, Brehova 7, Prague 11519, Czech Republic

³Kansai Photon Science Institute, National Institutes for Quantum and Radiological Science and Technology, Umemidai 8-1-7, Kizugawa, Kyoto 619-0215, Japan

⁴TAE Technologies, Pauling 19631, Foothill Ranch, California 92610, USA



(Received 7 July 2020; revised 3 September 2020; accepted 25 October 2020; published 30 November 2020)

Using an analytical model and computer simulation, we show that the wakefield driven by an ultrashort laser pulse in high-density plasma periodically reverses its polarity due to the carrier-envelope phase shift of the driver. The wakefield polarity reversal occurs on spatial scales shorter than the typical length considered for electron acceleration with the laser-wakefield mechanism. Consequently, the energies of accelerated electrons are significantly affected. The results obtained are important for the laser-wakefield acceleration under the conditions relevant to present-day high-repetition-rate laser systems.

DOI: [10.1103/PhysRevE.102.053216](https://doi.org/10.1103/PhysRevE.102.053216)

I. INTRODUCTION

Laser-wakefield acceleration (LWFA) is a well-established technique for producing high-energy electrons in plasma [1,2]. Over the past few decades, the quality of electron beams accelerated via LWFA has rapidly evolved mainly due to the advances in technology and better understanding of the underlying physics. As of 2020, LWFA has demonstrated (although not simultaneously) the capability to produce electron beams at the multi-GeV energy scale with a relative energy spread of a few percent [3,4], a few fs duration [5–8], and hundreds of pC of charge [9,10]. These achievements make LWFA increasingly attractive for a wide range of multidisciplinary experiments and applications (e.g., radiography [11], radiotherapy [12], and radiolysis [12,13]).

Recently, there has been a growing interest in LWFA driven by high-repetition-rate (\gtrsim kHz) laser systems since they can significantly improve certain characteristics (e.g., stability, signal-to-noise ratio, and average electron current [14]) required by a number of practical applications (e.g., ultrafast electron diffraction [15,16], fs x-ray generation [17,18], and pulsed radiolysis [19]). In order to produce high-quality relativistic LWFA electron sources with present-day kHz lasers, one should use tightly focused, near-single-cycle pulses and thin, near-critical density gas targets [14,20]. Such considerations constitute a great challenge not only from a technical point of view, but also in the sense of the understanding of underlying physical processes (e.g., related to the λ^3 regime [21]).

The LWFA of electrons at kHz using laser pulses with energies <10 mJ has been pursued by several groups [22–24]. The specificities of the corresponding laser-plasma

interaction, particularly the effects of the driver carrier-envelope phase (CEP) on the electron beam dynamics [25], the electron injection [26], and the electron energy spectra [14,27], were investigated. In this paper, we present the results of analytical and numerical study of the wakefield driven by an ultrashort laser pulse in high-density plasma. We show that the wakefield polarity periodically reverses due to the CEP shift of the driving pulse which significantly affects the energies of electrons accelerated via LWFA under the conditions relevant to current high-repetition-rate lasers.

II. DISPERSION AND CARRIER-ENVELOPE PHASE SHIFT EFFECTS

The propagation of a small amplitude electromagnetic wave in collisionless plasma is governed by the dispersion equation $\omega^2 = 1 + k^2$. The frequency, ω , and wave number, k , of the electromagnetic wave are measured in the units of ω_p and ω_p/c , respectively, where $\omega_p = \sqrt{4\pi n_0 e^2/m_e}$ is the Langmuir frequency, c is the speed of light in vacuum, n_0 is the ambient electron number density, e is the elementary charge, and m_e is the electron mass. The phase and group velocities of the electromagnetic wave (in the units of c) are equal to $\beta_{ph} = \sqrt{1 + k^2}/k$ and $\beta_g = k/\sqrt{1 + k^2}$, respectively. As one may see, $\beta_{ph}\beta_g = 1$.

In dispersive media, the phase and group velocities are not equal to each other, $\beta_{ph} \neq \beta_g$, which causes the evolution of the driver CEP. The characteristic time scale of the CEP shift effects can be expressed by a typical dispersion time, t_{disp} , defined as the time span needed to acquire the CEP shift of the driver equal to π ,

$$t_{disp} = \pi/\omega(\beta_{ph} - \beta_g) = \pi\beta_g/\omega(1 - \beta_g^2). \quad (1)$$

The driver field during the time interval $<t_{disp}$ can be in one-dimensional (1D) geometry approximated by the vector

*petr.valenta@eli-beams.eu

potential of the following form:

$$a = a_0 \frac{\sin [\Delta k(x - \beta_g t)]}{\Delta k(x - \beta_g t)} \cos [k_c(x - \beta_{\text{ph}} t) + \varphi]. \quad (2)$$

Here, a_0 is the peak vacuum amplitude of the driver normalized by $m_e c^2/e$ and φ is the phase of the carrier wave. The driver wave numbers are assumed to lie within a finite band $k_c - \Delta k < k < k_c + \Delta k$, with $\Delta k \ll k_c$. The spatial coordinate, x , and time, t , are measured in units of c/ω_p and ω_p^{-1} , respectively.

While propagating in plasma, the driver excites a wakefield that can be described by the following system of equations [2]:

$$\partial_t p + v \partial_x p = -E + F, \quad (3)$$

$$\partial_t E + v \partial_x E = v. \quad (4)$$

Here p is the x component of the electron momentum normalized by $m_e c$, E is the x component of the electric field normalized by $E_p = m_e \omega_p c/e$, and $v = p/\gamma$ with γ being the electron Lorentz factor. This yields

$$F = -(1/2\gamma) \partial_x a^2 \quad (5)$$

for the driving force (in the units of $m_e \omega_p c$) with $a(x, t)$ given by Eq. (2). The transverse component of the generalized momentum is conserved (i.e., $p_\perp - a = \text{const}$) and, therefore, $\gamma = \sqrt{1 + a^2 + p^2}$. In the following, we assume that $\gamma = 1$ (i.e., the laser-plasma interaction regime is well below the wake wave breaking threshold). The nonlinear case is addressed by numerical simulation in the second part of the paper.

The system of Eqs. (3) and (4) can be solved, e.g., using Lagrange coordinates, x_0 and τ . The relation between the Euler and Langrange coordinates is defined as $t = \tau$ and $x = x_0 + \xi(x_0, \tau)$, where x_0 is the initial coordinate of the fluid element (at $t = 0$) and ξ is a displacement of the fluid element from its initial position, x_0 , to the point x during the time t ; thus $\partial_\tau \xi = v$. Assuming that $\xi \ll x_0$, the solution in quadratures reads

$$p + iE = \int_0^\tau \frac{a_0^2 k_c}{2} e^{i(\tau-\tau')} \left(\frac{\sin [\Delta k(x_0 - \beta_g \tau')]}{\Delta k(x_0 - \beta_g \tau')} \right)^2 \times \sin [2k_c(x_0 - \beta_g^{-1} \tau') + 2\varphi] d\tau'. \quad (6)$$

In the ultrashort driver pulse limit, the solution (being transformed back to the Euler coordinates) becomes

$$p = -\frac{a_0^2}{2\beta_g} \frac{k_c}{\Delta k} \cos \left(\frac{x - \beta_g t}{\beta_g} \right) \sin \left(2k_c \frac{1 - \beta_g^2}{\beta_g^2} x - 2\varphi \right), \quad (7)$$

$$E = \frac{a_0^2}{2\beta_g} \frac{k_c}{\Delta k} \sin \left(\frac{x - \beta_g t}{\beta_g} \right) \sin \left(2k_c \frac{1 - \beta_g^2}{\beta_g^2} x - 2\varphi \right), \quad (8)$$

where $0 < x \leq \beta_g t$ and $t \geq 0$.

As can be seen from Eqs. (7) and (8), the ultrashort driver pulse in plasma excites the wakefield of a wavelength $\lambda_w = 2\pi\beta_g$ propagating with the phase velocity, β_w , equal to the group velocity of the driver, $\beta_w = \beta_g$. In addition to the standard model, the wakefield contains a sinusoidal modulation of the amplitude due to the slippage of the driver CEP. The

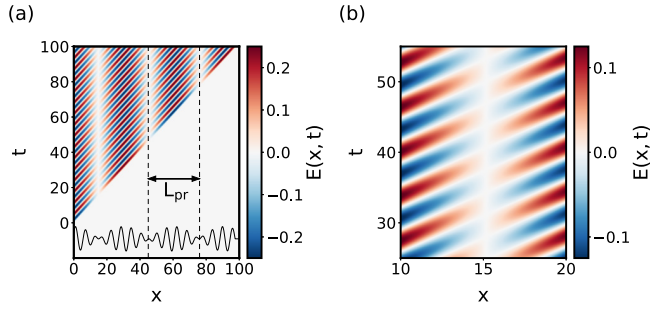


FIG. 1. Wakefield, $E(x, t)$, distribution in the (x, t) plane according to Eq. (8). The parameters of the driver are $\beta_g = 0.975$, $a_0 = 0.5$, $k_c = 1$, $\Delta k = 0.5$, and $\varphi = 3\pi/4$ and the plasma is homogeneous with $n_0 = 0.5n_c$. Panel (a) shows the periodic reversal of the wakefield polarity with $L_{\text{pr}} \simeq 30.24$ (marked by dashed lines); the detail of the wakefield polarity reversal is shown in (b). The solid line at the bottom of (a) shows the line-out of the wakefield along the axis $t = 100$.

modulation wavelength, given by $\lambda_{\text{mod}} = \pi \beta_g^2/k_c(1 - \beta_g^2)$, corresponds to the propagation length of the driver required to shift its CEP by the factor of π [compare with Eq. (1)]. As a consequence, the wakefield polarity periodically reverses. The range between two adjacent longitudinal coordinates at which the wakefield polarity reversal occurs is expressed by the polarity reversal length,

$$L_{\text{pr}} = \lambda_{\text{mod}}/2 = \pi \beta_g^2/2k_c(1 - \beta_g^2). \quad (9)$$

Figure 1 shows the wakefield distribution in the (x, t) plane according to Eq. (8). The parameters of the driver are $\beta_g = 0.975$, $a_0 = 0.5$, $k_c = 1$, $\Delta k = 0.5$, and $\varphi = 3\pi/4$ and the plasma is homogeneous with $n_0 = 0.5n_c$, where $n_c = n_0 \omega^2$ stands for the critical plasma density. In panel (a), one may see the periodic reversal of the wakefield polarity with $L_{\text{pr}} \simeq 30.24$. Panel (b) shows the detail of the wakefield polarity reversal.

III. ELECTRON ACCELERATION BY MODULATED WAKEFIELD

As is well known, the energy of the LWFA accelerated electron is limited by the value determined by the dephasing length,

$$L_d = \pi \beta_g/(1 - \beta_g). \quad (10)$$

Following from the model, the polarity reversal length is (in underdense plasma) always shorter than the dephasing length, $L_{\text{pr}} < L_d$. A comparison between L_{pr} and L_d defined by Eqs. (9) and (10), respectively, is shown in Fig. 2.

The wakefield polarity reversal in its turn affects the energy of the accelerated electron. For illustration, let us consider a relativistic electron traversing the wakefield with velocity approaching the speed of light. The net change of the kinetic energy of the electron moving along the path from $x_0 = 0$ to

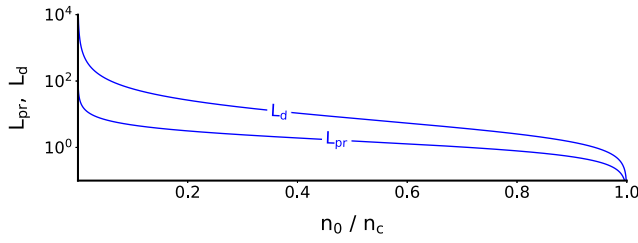


FIG. 2. Comparison between the polarity reversal length, L_{pr} , and the dephasing length, L_d , defined by Eqs. (9) and (10), respectively, in the whole range of underdense plasma.

$x_1 = x$ (in the units of $m_e c^2$) is given by

$$\begin{aligned} \Delta\mathcal{E}(x) &= \int_0^x E(x', t = x') dx' \\ &= \frac{a_0^2}{4\beta_g} \frac{k_c}{\Delta k} \frac{\cos(\alpha^- x + 2\varphi) \sin(\alpha^- x)}{\alpha^-} \\ &\quad - \frac{a_0^2}{4\beta_g} \frac{k_c}{\Delta k} \frac{\cos(\alpha^+ x - 2\varphi) \sin(\alpha^+ x)}{\alpha^+}, \end{aligned} \quad (11)$$

with the coefficients α^+ and α^- equal to

$$\alpha^\pm = \frac{\pi}{2} \left(\frac{1}{L_d} \pm \frac{1}{L_{\text{pr}}} \right). \quad (12)$$

The energy change of the electron described by Eq. (11) is shown in Fig. 3. The electron is traversing the wakefield given by Eq. (8) for the same parameters of the driver and plasma as in Fig. 1 (solid line). As can be seen, the electron either gains or loses energy over the distance of $L_{\text{pr}} \simeq 30.24$ due to the periodic reversal of the wakefield polarity. The energy balance of the electron over $L_d \simeq 122.52$ is $\Delta\mathcal{E} \simeq -1.29$. Using the standard model (i.e., neglecting the wakefield polarity reversal), the electron would theoretically gain the energy of $\Delta\mathcal{E} \simeq 20$ over the same distance. Since $L_{\text{pr}} \ll L_d$, the electron energy gain under the considered conditions is always lower than the maximum value determined by the standard model.

It follows from Eq. (11) that the energy gain depends on the initial phase of the driver, φ . Therefore, one may find (by examining the function extrema) an optimal phase of the driver, φ_{opt} , for which the net energy acquired by the electron over given distance is maximal. Provided that the electron injection is localized at $x = 0$ and the acceleration takes place

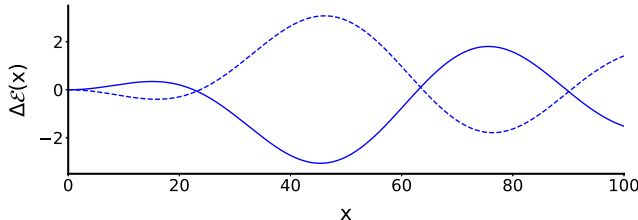


FIG. 3. Energy change of the relativistic electron, $\Delta\mathcal{E}(x)$, according to Eq. (11). The solid line shows the energy change of electron traversing the wakefield described by Eq. (8) for the same parameters of the driver and plasma as in Fig. 1. The dashed line shows the energy change of electron for $\varphi = \varphi_{\text{opt}}$.

over L_d ,

$$\varphi_{\text{opt}}^n = \frac{\pi}{4} \left(1 + \frac{L_d}{L_{\text{pr}}} \right) + n\pi, \quad n \in \mathbb{Z}. \quad (13)$$

The energy change of the electron for $\varphi = \varphi_{\text{opt}}$ is shown in Fig. 3 by the dashed line.

IV. PARTICLE-IN-CELL SIMULATION

A. Simulation setup

Now we explore the self-consistent evolution of the ultra-short laser pulse and near-critical density plasma numerically by means of particle-in-cell (PIC) simulation in a three-dimensional (3D) Cartesian geometry. The simulation is carried out using the PIC code EPOCH [28]. The driver laser pulse is characterized with the frequency $\omega_0 = 2\pi c/\lambda_0$, where λ_0 is its vacuum wavelength. The driver is Gaussian in both spatial and temporal profiles. Its peak normalized amplitude is $a_0 = 1.4$. It contains a single optical cycle, i.e., its full width at half maximum duration is $\tau_0 = 1 T_0$, where $T_0 = \lambda_0/c$ is the cycle period of the driver. The beam waist, $w_0 = 4\lambda_0$, is chosen such that the Rayleigh length of the driver is sufficiently long, and thus enables one to capture the periodic nature of the wakefield polarity reversal.

The driver, being linearly polarized along the z axis, propagates along the x axis in a preionized homogeneous slab of a hydrogen plasma with electron and proton densities $n_{e,p} = 0.1n_c$. The number of quasiparticles per cell is 4 for both particle species. The impact of the wakefield polarity reversal on the electron acceleration is studied using a beam of test electrons introduced through the left simulation boundary. The test electrons are initially monoenergetic with the Lorentz factor $\gamma_e = \sqrt{10}$, so that their velocity is comparable to the wake wave phase velocity (to fulfill the injection conditions).

The size of the simulation domain is $120\lambda_0$ in the laser propagation direction and $40\lambda_0$ in the transverse directions. The Cartesian grid is uniform with the resolution of 40 and 20 cells per λ_0 along the laser propagation direction and the transverse directions, respectively. The group velocity of the driving pulse in plasma can be roughly estimated as $v_g \simeq c\sqrt{1 - \omega_p^2/\omega_0^2} \simeq 0.95c$ and the wave number equals $k_c = \sqrt{\omega_0^2 - \omega_p^2}/c \simeq 5.96\lambda_0^{-1}$. This yields $L_{\text{pr}} \simeq 2.37\lambda_0$ and $L_d \simeq 29.24\lambda_0$ for the polarity reversal and dephasing lengths defined by Eqs. (9) and (10), respectively.

B. Simulation results

Figure 4 shows the temporal evolution of the wakefield on the laser propagation axis, where one may clearly see that the wakefield polarity periodically reverses [panel (a)] as well as the detail of the wakefield polarity reversal [panel (b)]. The results of the PIC simulation qualitatively correspond to the analytical model derived above (compare with Fig. 1). Figure 5 shows the spatial distribution of the wakefield at time $t = 100T_0$, where one may see that the polarity reversal of the wakefield occurs only in the vicinity of the laser propagation axis.

The polarity reversal length, determined by measuring the range between two longitudinal coordinates at which

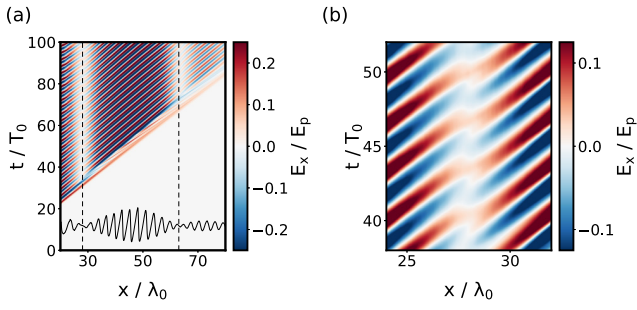


FIG. 4. Temporal evolution of the wakefield, E_x , on the laser propagation axis obtained from the 3D PIC simulation. Panel (a) shows the periodic reversal of the wakefield polarity with $L_{pr} \approx 35\lambda_0$ (marked by dashed lines); the detail of the wakefield polarity reversal is shown in (b). The solid line at the bottom of (a) shows the line-out of the wakefield along the axis $t = 100T_0$.

the wakefield polarity reverses, is $L_{pr} \approx 35\lambda_0$. We note that the value of L_{pr} as observed in the simulation differs from the analytical prediction. This could be due to several reasons: (i) the analytical model is 1D; (ii) the driver pulse amplitude is larger than unity and thus the interaction is not in the linear regime; (iii) although the driver pulse initially consists of a single optical cycle, it is not infinitely short. Moreover, it rapidly evolves into multiple cycles during the propagation in plasma due to the dispersion.

In Fig. 6, one can see the phase space of the test electrons, the on-axis wakefield, and the on-axis driver electric field at four successive instants of time. After traversing the plane of the wakefield polarity reversal, the electrons initially located in the accelerating phase of the wakefield start to decelerate (and vice versa). This leads to significant changes in the electron energies. As can be seen from the corresponding energy spectra, the energy of electrons initially located on the top of the phase space separatrix increases by $\approx 15\%$.

The presented simulation indicates that, in the nonlinear regime, there may exist a case for which $L_{pr} \approx L_d$. In such a case, the dephasing limit is overcome and the electrons are accelerated until the energy of the driver pulse fully depletes.

V. CONCLUSION

In conclusion, we reveal the properties of the wakefield driven by an ultrashort laser pulse in high-density plasma. The analytical model and PIC simulation show that the wakefield under the considered conditions periodically reverses its po-

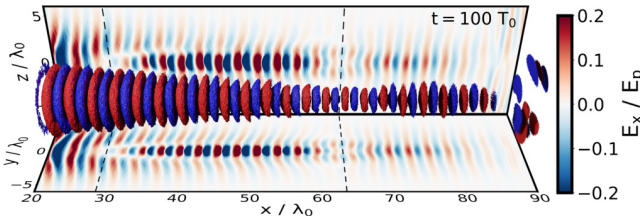


FIG. 5. Spatial distribution of the wakefield, E_x , at time $t = 100T_0$ obtained from the 3D PIC simulation. The dashed lines indicate the periodic reversal of the wakefield polarity with $L_{pr} \approx 35\lambda_0$.

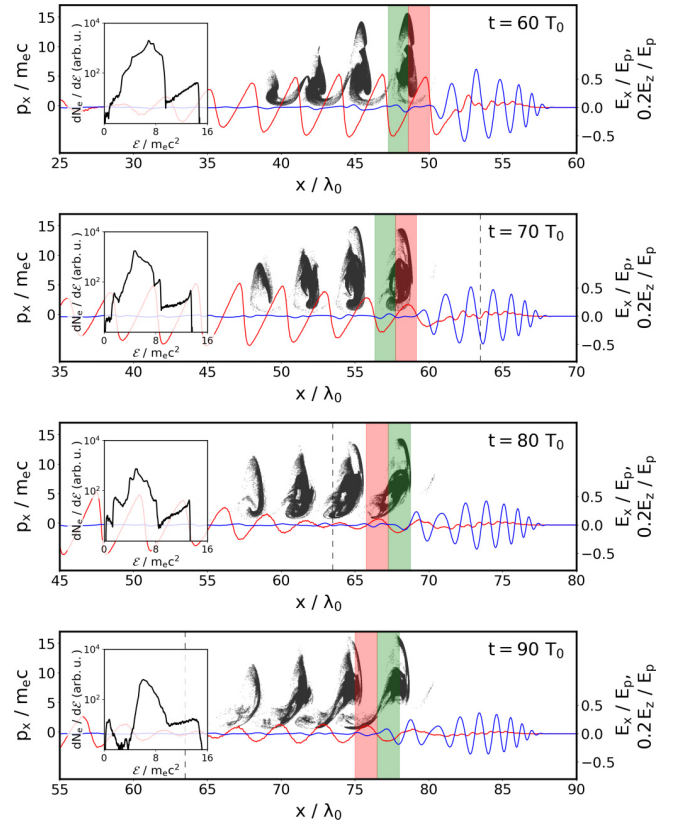


FIG. 6. (x, p_x) phase space of the test electrons (black), the on-axis wakefield, E_x (red), and the on-axis driver electric field, E_p (blue), at four successive time instants of the 3D PIC simulation. The corresponding inset shows the energy spectrum of electrons located in the first wake wave bucket behind the driver pulse, where N_e stands for the number of test electron quasiparticles. For the first wake wave bucket, the accelerating and decelerating phases of the wakefield are highlighted by green and red stripes, respectively. The longitudinal coordinate at which the wakefield polarity reversal occurs is marked by the dashed line.

larity. This phenomenon is caused by the effects of dispersion and the CEP shift of the driver which are otherwise negligible in the case of a long pulse and relatively low-density plasma. The wakefield polarity reversal occurs on spatial scales shorter than the dephasing length and, therefore, significantly affects the energies of accelerated electrons. The study presented in this work is important for the LWFA under the conditions relevant to present-day high-repetition-rate lasers, where the results obtained are useful for better controlling of the parameters of accelerated electron beams (e.g., by adjusting the initial phase of the driver or by controlling the phase of the electron injection). We note that the described wake wave structure in high-density plasma could be observed in experiments by a new generation of laboratory diagnostics [29–31].

ACKNOWLEDGMENTS

We appreciate discussions with Prof. H. Milchberg. This work was supported by the projects “High Field Initiative” (Grant No. CZ.02.1.01/0.0/0.0/15_003/0000449)

from the European Regional Development Fund and “IT4Innovations National Supercomputing Center” (Grant No. LM2015070) from the Ministry of Education, Youth and Sports of the Czech Republic. The EPOCH code

was in part funded by the UK Engineering and Physical Sciences Research Council (EPSRC) Grants No. EP/G054950/1, No. EP/G056803/1, No. EP/G055165/1, and No. EP/M022463/1.

-
- [1] T. Tajima and J. M. Dawson, *Phys. Rev. Lett.* **43**, 267 (1979).
 - [2] E. Esarey, C. B. Schroeder, and W. P. Leemans, *Rev. Mod. Phys.* **81**, 1229 (2009).
 - [3] H. T. Kim, K. H. Pae, H. J. Cha, I. J. Kim, T. J. Yu, J. H. Sung, S. K. Lee, T. M. Jeong, and J. Lee, *Phys. Rev. Lett.* **111**, 165002 (2013).
 - [4] A. J. Gonsalves, K. Nakamura, J. Daniels, C. Benedetti, C. Pieronek, T. C. H. de Raadt, S. Steinke, J. H. Bin, S. S. Bulanov, J. van Tilborg, C. G. R. Geddes, C. B. Schroeder, C. Tóth, E. Esarey, K. Swanson, L. Fan-Chiang, G. Bagdasarov, N. Bobrova, V. Gasilov, G. Korn, P. Sasorov, and W. P. Leemans, *Phys. Rev. Lett.* **122**, 084801 (2019).
 - [5] J. van Tilborg, C. B. Schroeder, C. V. Filip, C. Tóth, C. G. R. Geddes, G. Fubiani, R. Huber, R. A. Kaindl, E. Esarey, and W. P. Leemans, *Phys. Rev. Lett.* **96**, 014801 (2006).
 - [6] T. Ohkubo, A. Maekawa, R. Tsujii, T. Hosokai, K. Kinoshita, K. Kobayashi, M. Uesaka, A. Zhidkov, K. Nemoto, Y. Kondo, and Y. Shibata, *Phys. Rev. ST Accel. Beams* **10**, 031301 (2007).
 - [7] A. D. Debus, M. Bussmann, U. Schramm, R. Sauerbrey, C. D. Murphy, Z. Major, R. Hörlein, L. Veisz, K. Schmid, J. Schreiber, K. Witte, S. P. Jamison, J. G. Gallacher, D. A. Jaroszynski, M. C. Kaluza, B. Hidding, S. Kiselev, R. Heathcote, P. S. Foster, D. Neely, E. J. Divall, C. J. Hooker, J. M. Smith, K. Ertel, A. J. Langley, P. Norreys, J. L. Collier, and S. Karsch, *Phys. Rev. Lett.* **104**, 084802 (2010).
 - [8] O. Lundh, J. Lim, C. Rechatin, L. Ammoura, A. Ben-Ismaïl, X. Davoine, G. Gallot, J. P. Goddet, E. Lefebvre, V. Malka, and J. Faure, *Nat. Phys.* **7**, 219 (2011).
 - [9] Y. F. Li, D. Z. Li, K. Huang, M. Z. Tao, M. H. Li, J. R. Zhao, Y. Ma, X. Guo, J. G. Wang, M. Chen, N. Hafz, J. Zhang, and L. M. Chen, *Phys. Plasmas* **24**, 023108 (2017).
 - [10] J. P. Couperus, R. Pausch, A. Köhler, O. Zarini, J. M. Krämer, M. Garten, A. Huebl, R. Gebhardt, U. Helbig, S. Bock, K. Zeil, A. Debus, M. Bussmann, U. Schramm, and A. Irman, *Nat. Commun.* **8**, 487 (2017).
 - [11] Y. Glinec, J. Faure, L. Le Dain, S. Darbon, T. Hosokai, J. J. Santos, E. Lefebvre, J. P. Rousseau, F. Burgy, B. Mercier, and V. Malka, *Phys. Rev. Lett.* **94**, 025003 (2005).
 - [12] V. Malka, J. Faure, and Y. A. Gauduel, *Mutat. Res. - Reviews Mutat. Res.* **704**, 142 (2010).
 - [13] Y. A. Gauduel, Y. Glinec, J. P. Rousseau, F. Burgy, and V. Malka, *Eur. Phys. J. D* **60**, 121 (2010).
 - [14] J. Faure, D. Gustas, D. Guénot, A. Vernier, F. Böhle, M. Ouillé, S. Haessler, R. Lopez-Martens, and A. Lifschitz, *Plasma Phys. Controlled Fusion* **61**, 014012 (2019).
 - [15] G. Sciaiani and R. J. Miller, *Rep. Prog. Phys.* **74**, 096101 (2011).
 - [16] R. J. Miller, *Science* **343**, 1108 (2014).
 - [17] K. Ta Phuoc, S. Corde, C. Thaury, V. Malka, A. Tafzi, J. P. Goddet, R. C. Shah, S. Sebban, and A. Rousse, *Nat. Photon.* **6**, 308 (2012).
 - [18] S. Corde, K. Ta Phuoc, G. Lambert, R. Fitour, V. Malka, A. Rousse, A. Beck, and E. Lefebvre, *Rev. Mod. Phys.* **85**, 1 (2013).
 - [19] Y. Muroya, M. Lin, Z. Han, Y. Kumagai, A. Sakumi, T. Ueda, and Y. Katsumura, *Radiat. Phys. Chem.* **77**, 1176 (2008).
 - [20] F. Salehi, A. J. Goers, L. Feder, B. Miao, D. Woodbury, and H. M. Milchberg, *Rev. Sci. Instrum.* **90**, 103001 (2019).
 - [21] G. Mourou, Z. Chang, A. Maksimchuk, J. Nees, S. V. Bulanov, V. Y. Bychenkov, T. Z. Esirkepov, N. M. Naumova, F. Pegoraro, and H. Ruhl, *Plasma Phys. Rep.* **28**, 12 (2002).
 - [22] Z. H. He, B. Hou, J. A. Nees, J. H. Easter, J. Faure, K. Krushelnick, and A. G. Thomas, *New J. Phys.* **15**, 053016 (2013).
 - [23] F. Salehi, A. J. Goers, G. A. Hine, L. Feder, D. Kuk, B. Miao, D. Woodbury, K. Y. Kim, and H. M. Milchberg, *Opt. Lett.* **42**, 215 (2017).
 - [24] D. Guénot, D. Gustas, A. Vernier, B. Beaurepaire, F. Böhle, M. Bocoum, M. Lozano, A. Jullien, R. Lopez-Martens, A. Lifschitz, and J. Faure, *Nat. Photon.* **11**, 293 (2017).
 - [25] E. N. Nerush and I. Y. Kostyukov, *Phys. Rev. Lett.* **103**, 035001 (2009).
 - [26] A. F. Lifschitz and V. Malka, *New J. Phys.* **14**, 053045 (2012).
 - [27] M. Ouillé, A. Vernier, F. Böhle, M. Bocoum, A. Jullien, M. Lozano, J. P. Rousseau, Z. Cheng, D. Gustas, A. Blumenstein, P. Simon, S. Haessler, J. Faure, T. Nagy, and R. Lopez-Martens, *Light: Sci. Appl.* **9**, 47 (2020).
 - [28] T. D. Arber, K. Bennett, C. S. Brady, A. Lawrence-Douglas, M. G. Ramsay, N. J. Sircombe, P. Gillies, R. G. Evans, H. Schmitz, A. R. Bell, and C. P. Ridgers, *Plasma Phys. Controlled Fusion* **57**, 113001 (2015).
 - [29] N. H. Matlis, S. Reed, S. S. Bulanov, V. Chvykov, G. Kalintchenko, T. Matsuoka, P. Rousseau, V. Yanovsky, A. Maksimchuk, S. Kalmykov, G. Shvets, and M. C. Downer, *Nat. Phys.* **2**, 749 (2006).
 - [30] M. C. Downer, R. Zgadzaj, A. Debus, U. Schramm, and M. C. Kaluza, *Rev. Mod. Phys.* **90**, 035002 (2018).
 - [31] T. Z. Esirkepov, J. Mu, Y. Gu, T. M. Jeong, P. Valenta, O. Klimo, J. Koga, M. Kando, D. Neely, G. Korn, S. V. Bulanov, and A. S. Pirozhkov, *Phys. Plasmas* **27**, 052103 (2020).

B.3 Recoil effects on reflection from relativistic mirrors in laser plasmas

The following article is reproduced from Valenta, P., Esirkepov, T. Z., Koga, J. K., Pirozhkov, A. S., Kando, M., Kawachi, T., Liu, Y. K., Fang, P., Chen, P., Mu, J., Korn, G., Klimo, O., and Bulanov, S. V. (2020). [Recoil effects on reflection from relativistic mirrors in laser plasmas](#), *Physics of Plasmas*, **27**(3):032109, with the permission of AIP Publishing.

Copyright © 2020 American Institute of Physics.

Recoil effects on reflection from relativistic mirrors in laser plasmas

Cite as: Phys. Plasmas **27**, 032109 (2020); doi: 10.1063/1.5142084

Submitted: 10 December 2019 · Accepted: 21 February 2020 ·

Published Online: 10 March 2020



View Online



Export Citation



CrossMark

P. Valenta,^{1,2,a)} T. Zh. Esirkepov,³ J. K. Koga,³ A. S. Pirozhkov,³ M. Kando,³ T. Kawachi,³ Y.-K. Liu,⁴ P. Fang,⁴ P. Chen,⁴ J. Mu,¹ G. Korn,¹ O. Klimo,^{1,2} and S. V. Bulanov^{1,3,5}

AFFILIATIONS

¹ELI Beamlines, Institute of Physics, Czech Academy of Sciences, Na Slovance 2, 18221 Prague, Czech Republic

²Faculty of Nuclear Sciences and Physical Engineering, Czech Technical University in Prague, Brehova 7, 11519 Prague, Czech Republic

³Kansai Photon Science Institute, National Institutes for Quantum and Radiological Science and Technology, Umemidai 8-1-7, Kizugawa, 619-0215 Kyoto, Japan

⁴Leung Center for Cosmology and Particle Astrophysics, National Taiwan University, No. 1, Sec. 4, Roosevelt Rd., 10617 Taipei, Taiwan

⁵Prokhorov Institute of General Physics, Russian Academy of Sciences, Vavilova 38, 119991 Moscow, Russia

^{a)}Author to whom correspondence should be addressed: petr.valenta@eli-beams.eu

ABSTRACT

Relativistic mirrors can be realized with strongly nonlinear Langmuir waves excited by intense laser pulses in underdense plasma. On reflection from the relativistic mirror, the incident light affects the mirror motion. The corresponding recoil effects are investigated analytically and using particle-in-cell simulations. It is found that if the fluence of the incident electromagnetic wave exceeds a certain threshold, the relativistic mirror undergoes a significant back reaction and splits into multiple electron layers. The reflection coefficient of the relativistic mirror and the factors of electric field amplification and frequency upshift of the electromagnetic wave are obtained.

Published under license by AIP Publishing. <https://doi.org/10.1063/1.5142084>

I. INTRODUCTION

A relativistic mirror may be defined as an object that reflects incoming radiation while moving at relativistic velocity. The theory of light reflection from such an object propagating in vacuum at arbitrary (subluminal) velocity was first formulated by Einstein in 1905.¹ Since then, relativistic mirrors have been studied in many different contexts because of their great potential for both fundamental science and practical applications.

An electromagnetic wave incident on a relativistic mirror undergoes energy and frequency changes due to the double Doppler effect. In a co-propagating configuration in the laboratory frame of reference, the reflected wave is stretched, its amplitude is lowered, and its frequency is downshifted. In contrast, in a counter-propagating configuration, the reflected wave is compressed and amplified and its frequency is upshifted.

Relativistic mirrors can be realized by irradiating plasma targets with intense laser pulses (see Ref. 2 for a review and the literature cited therein). They appear in laser plasma as thin dense electron (or electron-ion) shells accelerated to relativistic velocities. Various schemes that lead to the generation of relativistic mirrors have been described

in theoretical and experimental studies (e.g., double-sided mirrors,^{3–13} oscillating mirrors,^{14–19} sliding mirrors,^{20,21} flying mirrors realized with strongly nonlinear Langmuir waves,^{22–28} or electron density singularities²⁹) and, hence, have already proven the feasibility of this concept.

Nowadays, relativistic mirrors in plasmas are actively studied as a unique tool for fundamental research (e.g., light intensification toward the Schwinger limit,²² investigation of photon–photon and Delbrück scattering^{27,30} analog black hole to investigate Hawking radiation, and the information loss paradox³¹) and for many practical applications in diverse fields; depending on whether the configuration is co-propagating or counter-propagating in the laboratory frame of reference, relativistic mirrors might be used either for the acceleration of ions (e.g., for hadron therapy³²) or for producing coherent high-brightness radiation with wavelengths ranging from x-ray to gamma-ray (e.g., for molecular imaging³³ and attosecond spectroscopy³⁴).

Maximization of the reflected radiation energy requires a more intense incident electromagnetic wave. However, sufficiently strong incident light can significantly affect the motion of the relativistic mirror (i.e., its radiation pressure can stop or destroy the mirror). In the

present paper, we aim at a closer description of the recoil effects on a reflection from the relativistic mirror. We study the interaction of strongly nonlinear Langmuir waves with an incident counter-propagating electromagnetic wave and the properties of the reflected radiation. We discuss the regimes when the relativistic mirror undergoes a significant back reaction. We find the threshold of the onset of the recoil effects.

This paper is organized as follows: in Sec. II, we derive the threshold for the energy of the incident electromagnetic wave; in Sec. III, we discuss the physical realization of relativistic mirrors in laser plasma; and in Sec. IV, we demonstrate the results of one-dimensional (1D) particle-in-cell (PIC) simulations and compare them with the analytical calculations.

II. RECOIL EFFECTS ON REFLECTION FROM RELATIVISTIC MIRRORS

For a relativistic mirror propagating at constant velocity v_M in vacuum, the frequency upshift of a normally incident counter-propagating electromagnetic wave is given by¹

$$\frac{\omega}{\omega_0} = \frac{1 + \beta_M}{1 - \beta_M} = \frac{\gamma_M + \sqrt{\gamma_M^2 - 1}}{\gamma_M - \sqrt{\gamma_M^2 - 1}} \approx 4\gamma_M^2, \quad (1)$$

where ω and ω_0 are the frequencies of the reflected and incident radiation, respectively, $\beta_M = v_M/c$ is the velocity of the relativistic mirror normalized by the speed of light in vacuum c , and $\gamma_M = 1/\sqrt{1 - \beta_M^2}$ is the corresponding relativistic Lorentz factor. The last term in Eq. (1) is obtained using the identity $\gamma_M + \sqrt{\gamma_M^2 - 1} = (\gamma_M - \sqrt{\gamma_M^2 - 1})^{-1}$ and $\gamma_M + \sqrt{\gamma_M^2 - 1} \approx 2\gamma_M$ and is valid in the ultra-relativistic limit, i.e., when $\gamma_M \gg 1$. The factor of the electric field amplification of the reflected wave is given by¹

$$\frac{E}{E_0} = \frac{\omega}{\omega_0} \sqrt{R}, \quad (2)$$

where E and E_0 are the electric fields of the reflected and incident radiation, respectively, and R stands for the reflection coefficient in terms of the photon number.

Eqs. (1) and (2) are derived in the approximation of a weak incident electromagnetic wave. Here, we analytically investigate the recoil effects of a counter-propagating electromagnetic wave normally incident on a relativistic mirror. This problem was briefly discussed in Ref. 21. First, we consider the relativistic mirror in the form of an electron layer. We assume that all the electrons are characterized by the same momentum, the electromagnetic wave is monochromatic, and the reflection coefficient in terms of the photon number is equal to R . The conservation of momentum and energy before and after the interaction can be then written as

$$\mathcal{N}_e p_{e0} - \mathcal{N}_\gamma p_{\gamma0} = \mathcal{N}_e p_e + R \mathcal{N}_\gamma p_\gamma - (1 - R) \mathcal{N}_\gamma p_{\gamma0}, \quad (3)$$

$$\mathcal{N}_e \mathcal{E}_{e0} + \mathcal{N}_\gamma E_{\gamma0} = \mathcal{N}_e \mathcal{E}_e + R \mathcal{N}_\gamma \mathcal{E}_\gamma + (1 - R) \mathcal{N}_\gamma \mathcal{E}_{\gamma0}. \quad (4)$$

Here, \mathcal{N}_e and \mathcal{N}_γ are the numbers of interacting electrons and photons, respectively. The subscript “0” denotes the quantities before the interaction, and the “−” sign in Eq. (3) denotes counter-propagating photons. The electron and photon momenta and energies can be expressed as

$$p_e = m_e c \sqrt{\gamma_e^2 - 1}, \quad p_\gamma = \hbar \omega / c, \quad (5)$$

$$\mathcal{E}_e = m_e c^2 \gamma_e, \quad \mathcal{E}_\gamma = \hbar \omega, \quad (6)$$

where the symbols \hbar , γ_e and m_e denote the reduced Planck constant, the relativistic Lorentz factor of electrons, and the electron rest mass, respectively.

By combining Eqs. (3)–(6), we obtain the following formula:

$$\begin{aligned} \hbar \omega &= \hbar \omega_0 \frac{\mathcal{N}_e (\mathcal{E}_{e0} + p_{e0} c)}{\mathcal{N}_e (\mathcal{E}_{e0} - p_{e0} c) + 2R \mathcal{N}_\gamma \hbar \omega_0} \\ &= \hbar \omega_0 \frac{\mathcal{N}_e m_e c^2 (\gamma_{e0} + \sqrt{\gamma_{e0}^2 - 1})}{\mathcal{N}_e m_e c^2 (\gamma_{e0} - \sqrt{\gamma_{e0}^2 - 1}) + 2R \mathcal{N}_\gamma \hbar \omega_0}. \end{aligned} \quad (7)$$

In the ultrarelativistic limit, i.e., when $\gamma_{e0} \gg 1$, Eq. (7) can be simplified as

$$\frac{\omega}{\omega_0} \approx 4\gamma_{e0}^2 \frac{\frac{\mathcal{N}_e m_e c^2}{4\gamma_{e0}}}{\frac{\mathcal{N}_e m_e c^2}{4\gamma_{e0}} + R \mathcal{N}_\gamma \hbar \omega_0}. \quad (8)$$

The two terms in the denominator of Eq. (8) correspond to the energy of the electron layer and interacting photons, respectively. The resulting frequency upshift of the reflected radiation is determined by the relationship between both terms

$$\omega/\omega_0 \approx 4\gamma_{e0}^2 \quad \text{for} \quad R \mathcal{N}_\gamma \hbar \omega_0 \ll \frac{\mathcal{N}_e m_e c^2}{4\gamma_{e0}}, \quad (9a)$$

$$\omega/\omega_0 \approx \frac{\mathcal{N}_e m_e c^2 \gamma_{e0}}{R \mathcal{N}_\gamma \hbar \omega_0} \quad \text{for} \quad R \mathcal{N}_\gamma \hbar \omega_0 \gg \frac{\mathcal{N}_e m_e c^2}{4\gamma_{e0}}. \quad (9b)$$

The limit (9a) corresponds to the approximation of a weak incident electromagnetic wave and produces the classical frequency upshift factor corresponding to the double Doppler effect [see Eq. (1)]. In the opposite limit (9b), the incident radiation significantly affects the motion of relativistic mirror, so that the frequency of the reflected electromagnetic wave is in fact downshifted by the factor of $\mathcal{N}_e m_e c^2 \gamma_{e0} / (R \mathcal{N}_\gamma \hbar \omega_0) \ll 1$.

We define the threshold characterizing the recoil importance in this interaction as a midpoint between the limits given by Eqs. (9a) and (9b), when the energy of the interacting photons is comparable to that of the electron layer,

$$R \mathcal{N}_\gamma \hbar \omega_0 = \varkappa \frac{\mathcal{N}_e m_e c^2}{4\gamma_{e0}}, \quad (10)$$

where $\varkappa < 1$ is a small factor. Obviously, much less energy than the kinetic energy of the mirror can affect the reflection process.

III. RELATIVISTIC MIRROR REALIZED WITH A LANGMUIR WAVE

A sufficiently short and intense laser pulse excites a strongly nonlinear Langmuir wave in underdense plasma.^{35,36} The electron density modulations of the Langmuir wave in the wake of the laser pulse take the form of thin dense shells separated by cavities of the length corresponding to the Langmuir wave wavelength λ_w . A weak counter-propagating electromagnetic wave is partially reflected from these

shells, undergoing energy and frequency changes in accordance with the double Doppler effect. For this case, Eq. (1) becomes²

$$\begin{aligned}\frac{\omega}{\omega_0} &= \frac{1}{1 - \beta_w^2} \left(1 + \beta_w^2 + 2\beta_w \sqrt{1 - \frac{\omega_{pe}^2}{\omega_0^2}} \right) \\ &= 2\gamma_w^2 + 2\gamma_w \sqrt{\gamma_w^2 - 1} \sqrt{1 - \frac{\omega_{pe}^2}{\omega_0^2}} - 1\end{aligned}\quad (11)$$

so that it includes the difference between the phase and group velocity in plasma. Here, $\omega_{pe} = \sqrt{4\pi n_e e^2 / m_e}$ is the Langmuir frequency corresponding to the background electron density n_e , β_w is the phase velocity of the Langmuir wave normalized by c , and $\gamma_w = 1 / \sqrt{1 - \beta_w^2}$ is the corresponding relativistic Lorentz factor. The symbol e stands for the elementary charge.

If the velocity of the electrons in the vicinity of the electron density spike exceeds the phase velocity of the Langmuir wave, i.e., $\gamma_e > \gamma_w$, the Langmuir wave breaks. This corresponds to the Akhiezer-Polovin limit³⁷ for the longitudinal electric field, E_x , of the Langmuir wave,

$$\frac{\max|E_x|e}{m_e \omega_{pe} c} > \sqrt{2(\gamma_w - 1)}. \quad (12)$$

For the Langmuir wave at the threshold of wave-breaking, its reflection coefficient in terms of the photon number, R , is (see Ref. 2)

$$R \approx \frac{\Gamma^2(2/3)}{2^2 \cdot 3^{4/3}} \left(\frac{\omega_{pe}}{\omega_0} \right)^{8/3} \frac{1}{\gamma_w^{4/3}}, \quad (13)$$

where $\Gamma(x)$ is the Euler gamma function.³⁸

In order to estimate the threshold given by Eq. (10) for the relativistic mirror realized with a breaking Langmuir wave, we represent, for simplicity, the incident laser pulse as an electromagnetic wavepacket with a rectangular profile and intensity I , duration τ , and cross-sectional area S . We assume the normal incidence of this wavepacket on the relativistic mirror. The number of photons in the pulse, \mathcal{N}_γ , is given by the following expression:

$$\mathcal{N}_\gamma = \frac{I\tau S}{\hbar\omega_0}. \quad (14)$$

For a nearly breaking Langmuir wave, for which Eq. (13) holds, approximately half of the plasma electrons are concentrated in the electron density spike in each wave period. Therefore, the number of interacting electrons, \mathcal{N}_e , is

$$\mathcal{N}_e = \frac{n_e}{2} \lambda_w S. \quad (15)$$

Using the reflection coefficient of the Langmuir wave of Eq. (13) and the number of interacting photons and electrons of Eqs. (14) and (15), respectively, we rewrite the threshold of Eq. (10) in terms of the fluence (the product of intensity and duration) of the incident wavepacket,

$$\begin{aligned}I\tau &= \varkappa \frac{m_e c^2}{8} \frac{n_e \lambda_w}{\gamma_w R} \\ &= \varkappa \frac{3^{4/3} m_e c^2}{2\Gamma^2(2/3)} \left(\frac{\omega_0}{\omega_{pe}} \right)^{8/3} \gamma_w^{1/3} n_e \lambda_w.\end{aligned}\quad (16)$$

As can be seen from this formula, even a low intensity electromagnetic wavepacket is able to destroy the mirror, if it is sufficiently long. However, the relativistic mirror realized with the Langmuir wave consists of electrons that are continuously flowing through it. Consequently, the structure of the electron density spike is being refreshed every moment in time. Thus, the applicability of the model given by Eqs. (3)–(6) is better for a short-time interaction and sufficiently large electromagnetic wave intensity. We interpret the threshold of Eq. (16) as a condition for the minimum wavepacket duration required for a recoil effect,

$$\tau_{\min} = \varkappa \frac{3^{4/3} m_e c^2}{2\Gamma^2(2/3)} \left(\frac{\omega_0}{\omega_{pe}} \right)^{8/3} \gamma_w^{1/3} \frac{n_e \lambda_w}{I}. \quad (17)$$

In this interpretation, the incident wavepacket intensity becomes the main critical parameter for the recoil effects. Below, we investigate the applicability of the model and, in particular, Eq. (17) by PIC simulations.

IV. PARTICLE-IN-CELL SIMULATIONS

The properties of relativistic mirrors realized with strongly nonlinear Langmuir waves in underdense plasmas are studied numerically by means of PIC simulations in a 1D Cartesian geometry. The 1D configuration is sufficient for the investigation of the Langmuir wave interaction with a counter-propagating laser pulse and beneficial in view of the necessity of resolving frequency upshifted electromagnetic radiation according to Eq. (11). The results can be extrapolated to higher dimensions considering laser pulses with a wide focal spot. The simulations are performed using the fully relativistic electromagnetic PIC EPOCH code.³⁹

A. Simulation setup

The laser pulse that drives the Langmuir wave (from here on referred to as the “driver”) enters the simulation domain from the left boundary and propagates in the $+x$ direction. The laser pulse that undergoes the reflection from the Langmuir wave (from here on referred to as the “source”) enters from the right and propagates in the opposite (i.e., $-x$) direction. In the following, we use the superscripts “ d ”, “ s ”, and “ r ” to denote the quantities, which characterize the driver, the source, and the reflected pulse, respectively.

The driver is characterized by a wavelength in vacuum $\lambda_0^d = 2\pi c / \omega_0^d$, where ω_0^d is its angular frequency, and by the normalized amplitude $a_0^d = 10$ defined as $a_0^d = eE_0^d / (m_e \omega_0^d c)$, where E_0^d is the amplitude of the electric field in vacuum. Its temporal profile is Gaussian with a full-width-at-half-maximum duration $\tau_0^d = 10 T_0^d$, where $T_0^d = \lambda_0^d / c$ is the driver pulse cycle period. The values of a_0^d and τ_0^d are set so that they are optimal for the Langmuir wave generation;^{35,36} the driver amplitude a_0^d is set to be sufficiently high in order to excite a large amplitude nonlinear wave, which breaks in a controlled way and the driver duration τ_0^d is chosen such that the wave is excited resonantly (i.e., $c\tau_0^d \approx \lambda_w/2$). The driver is linearly polarized with the electric field directed along the y -axis.

The wavelength of the source pulse is $\lambda_0^s = 5 \lambda_0^d$. By this choice, we keep λ_0^s sufficiently short so that the effects of plasma dispersion on the source are not significant but long enough to substantially reduce the computational demands of the simulations. The source has a semi-infinite flat-top temporal profile, which allows us to analyze the

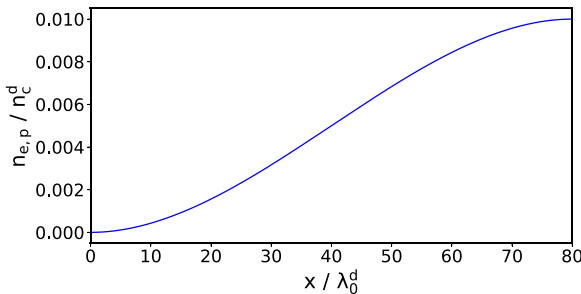


FIG. 1. Plot of the electron and proton density ramp profile used in the simulations.

simulation results more clearly. The normalized amplitude of the source, a_0^s , is varied in the simulations in order to thoroughly describe its impact on the reflection from the Langmuir wave. The source is linearly polarized in the direction perpendicular to the driver polarization (i.e., along the z -axis), and, thus, its electromagnetic field can be clearly distinguished.

Both laser pulses, the driver and the source, propagate in a pre-ionized uniform hydrogen plasma with electron and proton densities $n_{e,p}^0 = 10^{-2} n_c^d$, where $n_c^d = m_e(\omega_0^d)^2/(4\pi e^2)$ is the critical plasma density with respect to the driver pulse. A smooth ramp is added to the left side of the target in order to reduce the effect of wave-breaking from a sharp rising plasma edge.⁴⁰ The ramp is defined by the function $n_{e,p}(x) = n_{e,p}^0 (3 - 2(x - x_1)/(x_2 - x_1))((x - x_1)/(x_2 - x_1))^2$, where $x \in [x_1, x_2]$. The values $x_1 = 0$ and $x_2 = 80 \lambda_0^d$ have proven to provide a sufficiently smooth transition [one can see the plot of the density ramp $n_{e,p}(x)$ in Fig. 1]. The plasma is cold and collisionless. The electrons and protons are represented by quasi-particles with a triangular shape function. The number of quasi-particles per cell is 10 for both particle species. The smooth ramp in the plasma density profile is constructed by varying the weight of the quasi-particles (i.e., the number of real particles represented by each quasi-particle).

The simulations utilize a moving window technique,⁴¹ which allows us to substantially decrease the length of the simulation domain. For this, the EPOCH code was modified in order to continuously introduce source pulse at the right boundary of the moving widow. The length of the simulation window is $80 \lambda_0^d$, and it moves along the

driver propagation direction at a velocity equal to c . The resolution of the Cartesian grid is 30 cells per theoretically estimated wavelength of the reflected radiation λ' . The value of λ' is calculated using Eq. (1), where we estimate $\gamma_M \approx \omega_0^d/\omega_{pe}$. The simulation domain thus contains 1.92×10^5 cells in total, and the simulation time is set to $450 T_0^d$. The electromagnetic fields are calculated using the standard second-order Yee solver⁴² with the CFL number⁴³ equal to 0.99. Absorbing boundary conditions are applied on each of the simulation domain sides for both the electromagnetic field and particles.

B. Simulation results

First, we present the results of the simulation where the normalized amplitude of the source is relatively low, $a_0^s = 10^{-4}$, in order to avoid recoil effects and significant distortions of the Langmuir wave. The driver pulse starts to excite the Langmuir wave as soon as it enters the plasma. When the driver reaches the uniform plasma density region, the Langmuir wave takes the form of sharp electron density spikes separated by cavities. We consider the properties of the first electron density spike of the Langmuir wave formed behind the driver, which serves as a relativistic mirror. The first important parameter of the density spike in our study is its phase velocity because it determines the magnitudes of the carrier frequency upshift and electric field amplification of the reflected wave [see Eqs. (1) and (2)].

Figure 2(a) shows the evolution of the first electron density spike of the Langmuir wave behind the driver in the $x - t$ plane, (b) its normalized phase velocity β_w , and (c) the corresponding relativistic Lorentz factor γ_w . The moment of wave-breaking, $t \approx 190 T_0^d$, in Fig. 2 is denoted by black dashed lines. It corresponds to the limit given by Eq. (12). At this moment, the electron density spike is centered around the point $x \approx 150 \lambda_0^d$. The reflectivity of the Langmuir wave becomes significant when the wave is closer to breaking.² After the wave-breaking, it is determined not only by the properties of the regular Langmuir wave but also by the properties of the injected electrons. From Fig. 2, it can be clearly seen that the Langmuir wave decelerates in uniform plasma, which is partially caused due to non-linear energy depletion of the driver⁴⁵ and due to the wave-breaking. The simulation results are analyzed from $t_0 = 150 T_0^d$, when the first density spike of the Langmuir wave can be clearly localized, until $t_1 = 450 T_0^d$. As can be seen from Fig. 2(c), $\gamma_w \approx 1$ for $t \geq t_1$, and therefore, further reflection is not very interesting in the context of

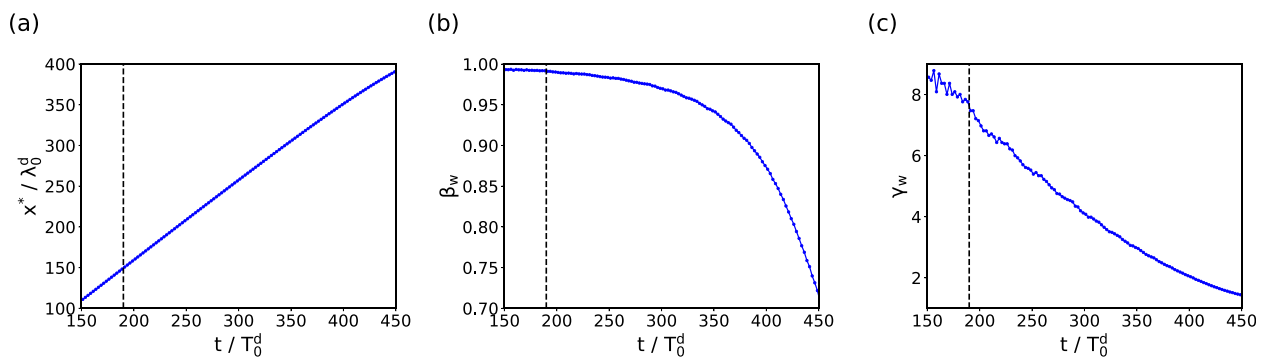


FIG. 2. The evolution of parameters of the first electron density spike of the Langmuir wave behind the driver in time. (a) The motion of the spike in the $x - t$ plane, (b) the normalized phase velocity of the spike β_w , and (c) the corresponding relativistic Lorentz factor γ_w . The black dashed line marks the instant, when the Langmuir wave breaks.

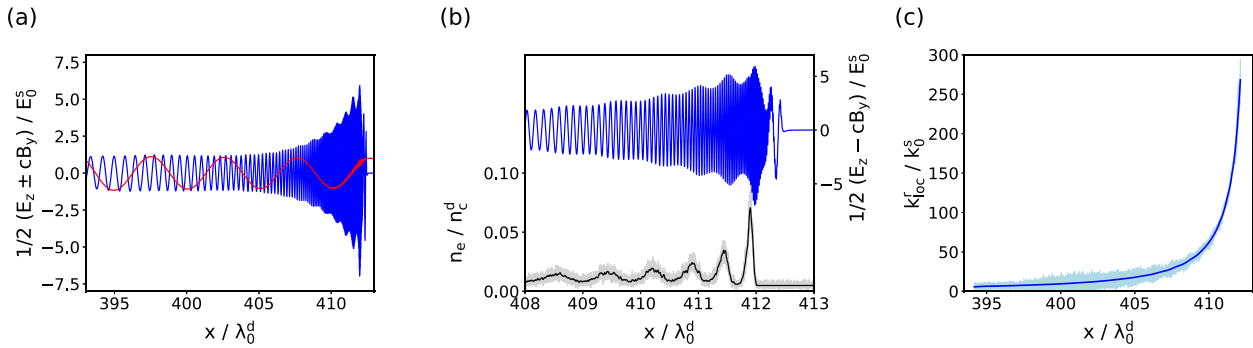


FIG. 3. (a) Electromagnetic radiation incident at (red) and reflected from (blue) the first electron density spike of the Langmuir wave behind the driver, (b) details of the reflected electromagnetic wave (blue) with modulations correlated with the electron density (black), and (c) the evolution of the local carrier wavenumber of the reflected electromagnetic wave showing a negative chirp due to the Langmuir wave deceleration. The simulation data are observed at $t = 450 T_0^d$. In (b) and (c), the simulation data (light gray and light blue) are smoothed using the Savitzky–Golay filter⁴⁴ (black and blue).

the generation of coherent short-wavelength radiation [see Eq. (11)]. We also note that since the density spikes lag behind the fronts of light reflected from them, at $t = t_1$, the front of light reflected from the second density spike catches up with the first density spike,

$$c \int_{t_0}^{t_1} (1 - \beta_w(t)) dt \approx \lambda_w, \quad (18)$$

and thus, the radiation continuously reflected from the second density spike starts to interfere with the radiation reflected from the first density spike.

The spatial profile of the electromagnetic radiation reflected from the first density spike observed at $t = 450 T_0^d$ is shown in Fig. 3(a). As can be clearly seen, its envelope is modulated. The modulations are caused by the electrons injected into the accelerating phase of the wake-field after the wave-breaking, which is shown in Fig. 3(b). Figure 3(c) displays the local carrier wavenumber of the reflected pulse. To obtain the local carrier wavenumber at any point in a reflected wavepacket, we first find the analytic signal from the original signal using the Hilbert transform.⁴⁶ The local carrier wavenumber is then obtained by differentiating the local phase (which corresponds to the phase angle of the analytic signal) with respect to x . It can be clearly seen that the reflected signal has a negative chirp, which corresponds to the mirror deceleration.

The wavelength of the reflected signal λ^r ranges from $\approx 0.17 \lambda_0^s$ to $\approx 3.3 \times 10^{-3} \lambda_0^s$, and hence, the upshift factor with respect to ω_0^s ranges from 6 to 298. Due to the effects of plasma dispersion, however, the wavelength of the source pulse interacting with the electron density spike is slightly larger than the vacuum wavelength, $\lambda^s \approx 1.04 \lambda_0^s$. Thus, the maximum factor of the frequency upshift with respect to ω^s is about 310. From this frequency upshift factor using Eq. (11), we can estimate the relativistic Lorentz factor of the electron density spike as $\gamma_w \approx 9.2$, which corresponds to the instant of time $t \approx 140 T_0^d$.

Using the dependence of the local carrier wavenumber of the reflected pulse on the electron density spike coordinate $k_{loc}^r(x)$ and the dependence of the spike coordinate on time $x^*(t)$, we obtain the time dependence of the frequency upshift factor of the reflected pulse,

$$\frac{\omega^r}{\omega_0^s} = \frac{k_0^s}{k_{loc}^r(x^*(t))}. \quad (19)$$

As seen in Fig. 4(a), the frequency upshift factor obtained in this way agrees very well with the calculation using Eq. (11) and the relativistic Lorentz factor of the electron density spike γ_w shown in Fig. 2(c).

Using the dependence of the reflected pulse electric field envelope amplitude on the spike coordinate $E_{env}^r(x^*(t))$, we obtain the time dependence of the electric field amplification factor

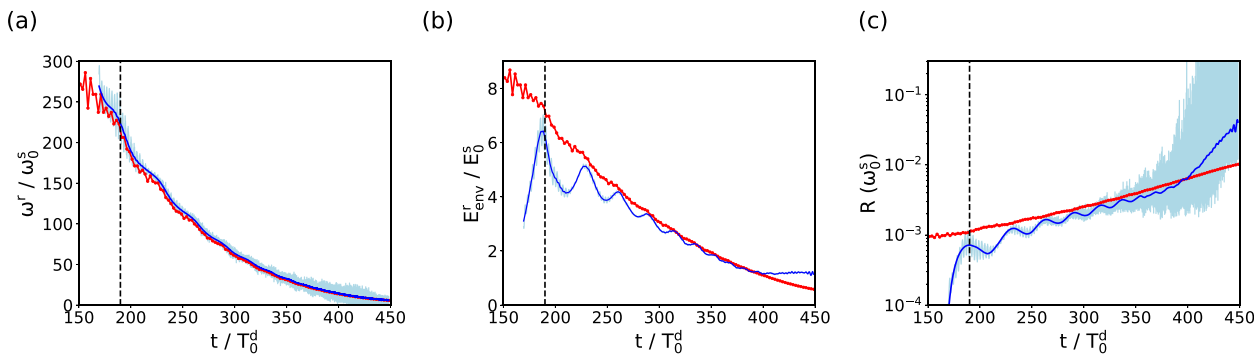


FIG. 4. The properties of the reflection from the first electron density spike of the Langmuir wave behind the driver. (a) The frequency upshift factor, (b) the electric field amplification factor, and (c) the instantaneous reflection coefficient in terms of the photon number. The simulation data (light blue) are smoothed using the Savitzky–Golay filter⁴⁴ (blue) and compared to analytical estimates (red). The black dashed line marks the instant, when the Langmuir wave breaks.

$$\frac{E_{env}^r}{E_0^s} = \frac{E_{env}^r(x^*(t))}{E_0^s}. \quad (20)$$

As seen in Fig. 4(b), the electric field amplification factor obtained in this way shows again fairly good conformity with the calculation using Eqs. (11) and (13) and the relativistic Lorentz factor of the electron density spike γ_w shown in Fig. 2(c). We find that the electric field amplification factor reaches its maximum at the moment of wave-breaking, with the electric field of the reflected pulse being amplified more than six times. Contrary to the analytical calculation, the amplification factor obtained from the simulation comprises visible oscillations. As discussed above, this feature corresponds to the modulations of the envelope of the reflected pulse caused by the electrons injected into the accelerating phase of the wakefield [see Fig. 3(b)].

Using the factors of the frequency upshift and the electric field amplification of the reflected pulse shown in Figs. 4(a) and 4(b), we reconstruct the instantaneous reflection coefficient of the electron

density spike in time, Fig. 4(c). For comparison, in Fig. 4(c), we also plot the instantaneous reflection coefficient computed using Eq. (13) and the relativistic Lorentz factor γ_w shown in Fig. 2(c). We find that the reflection coefficient in terms of the photon number grows from $\approx 10^{-3}$ at the moment of wave-breaking up to $\approx 5 \times 10^{-2}$ at the end of the interaction.

In order to investigate the recoil effects and explore the regimes around the threshold given by Eq. (16), we increase the amplitude of the source. Now, the source pulse encounters the electron density spike at the moment of wave-breaking ($t = 190 T_0^d$). Its normalized amplitude a_0^s is varied from 0.01 to 1. The reflected radiation for the simulated cases can be seen in Fig. 5(a). In the case of $a_0^s = 0.01$, the interaction corresponds to the weak incident pulse approximation, and the impact of the source pulse is compensated by the electron flow that refreshes the structure of the density spike. For much larger amplitude, $a_0^s = 1$, only one cycle of the reflected wave is formed

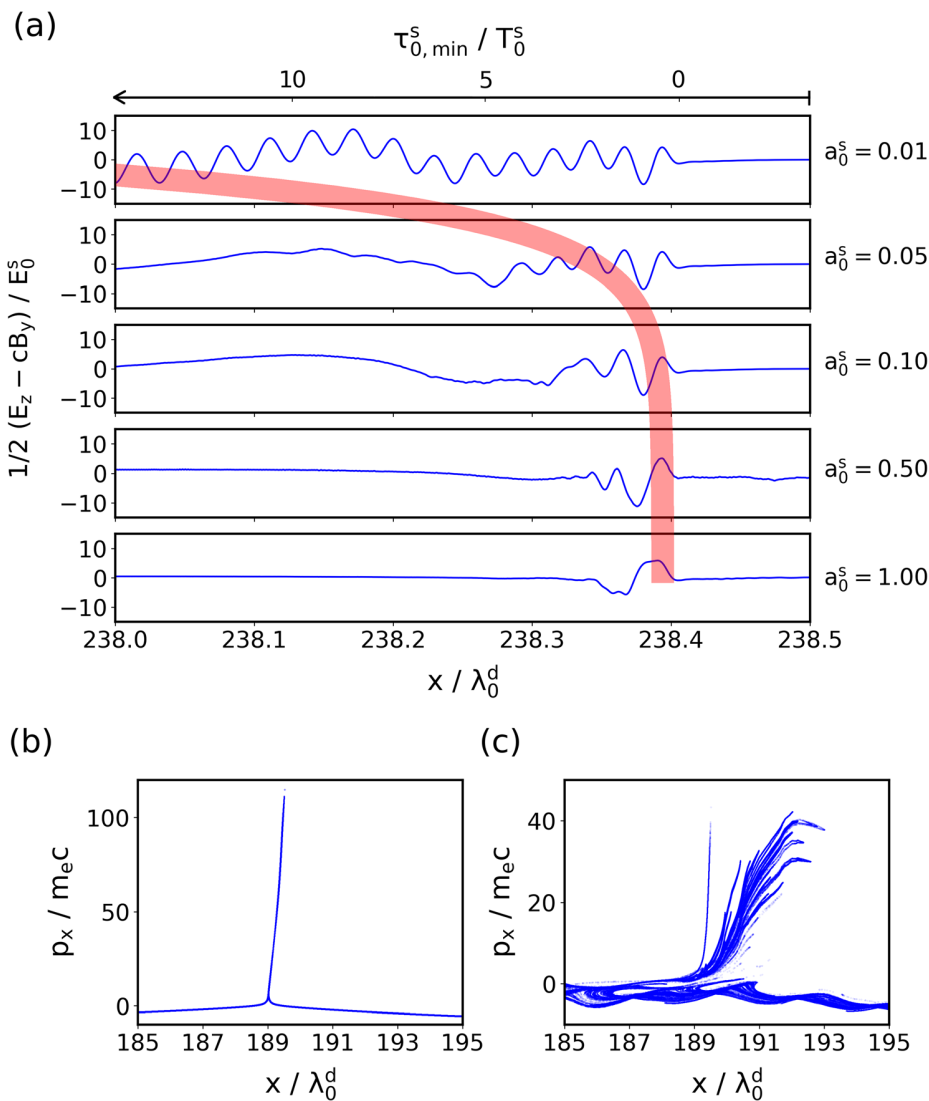


FIG. 5. Dependence of the reflected radiation on the amplitude of the source pulse. (a) Spatial profiles of the reflected wave for different source amplitudes. The thick red curve across the frames is the minimum source duration required for the recoil effect, $\tau_{0,min}^s$, according to Eq. (17) for $\varkappa = 1.5 \times 10^{-4}$. The phase space of electrons at $t = 230 T_0^d$ for (b) $a_0^s = 0.01$ and (c) $a_0^s = 1.0$.

before the relativistic mirror is destroyed. Moreover, the radiation pressure of the source pulse in this case pushes the mirror back, which results in lower factors of the frequency upshift and the electric field amplification.

The threshold (17) gives the minimal duration of the incident electromagnetic wave necessary to cause a significant recoil on the relativistic mirror. In terms of normalized quantities, this duration can be rewritten as

$$\tau_{0,\min}^s = \frac{\varkappa}{4} \frac{n_e \lambda_w \lambda_0^s}{\gamma_w R(a_0^s)^2}, \quad (21)$$

where $\tau_{0,\min}^s$ is normalized by T_0^s , λ_0^s , and λ_w by λ_0^d and n_e by n_c^d . This quantity is shown in Fig. 5(a), for different source pulse amplitudes and $\varkappa = 1.5 \times 10^{-4}$. The value of the coefficient \varkappa is obtained from the comparison of the spatial profiles of the reflected wave for different incident wavepacket amplitudes. We assume that the duration $\tau_{0,\min}^s$ roughly corresponds to the time period where the reflected wave coincides with the weak-source approximation. We see that for $a_0^s = 0.01$, the reflected wave corresponds to the weak-source approximation and classical double Doppler effect. Here, $\tau_{0,\min}^s$ is very large. For $a_0^s = 1$, the recoil effects are well pronounced; the spatial profile of the reflected wave deviates from the weak-source approximation almost immediately. In this case, $\tau_{0,\min}^s$ is almost zero. Between $a_0^s = 0.01$ and $a_0^s = 1$, the properties of the spatial profile of the reflected wave correlate with the minimum source duration causing recoil effects given by Eq. (21), derived from the models (3)–(6).

A time span needed for a density spike to be fully refreshed by the electron flow can be roughly estimated as $t_{ref} \approx \lambda_w/v_g^d \approx 20.53 T_0^d$, where v_g^d is the group velocity of the driver pulse. During this time span, the density spike interacts approximately with 7.62 cycles of the source pulse. Therefore, if $\tau_{0,\min}^s > 7.62 T_0^s$, the impact of the source pulse on the density spike is compensated by the flow of electrons, and the interaction corresponds to the weak-source approximation. Using Eq. (21) with $\varkappa = 1.5 \times 10^{-4}$, this condition is equivalent to $a_0^s < 0.026$.

In Figs. 5(b) and 5(c), one can see the phase space of electrons located in the density spike illustrating the importance of the recoil effects of the relativistic mirror for two different amplitudes of the source pulse. For relatively small amplitudes, the structure of the electron density spike and the injected electrons (appearing after wave-breaking) are not affected, Fig. 5(b). When the intensity of the source pulse becomes sufficient to alter the motion of the electrons in the density spike, the spike splits into several layers, Fig. 5(c). The disappearance of the periodic structure of the reflected electromagnetic wave seen in Fig. 5(a) for $a_0^s \geq 0.05$ is partially due to the destructive interference of waves reflected from the multi-layered structure of the split electron density spike and due to the recoil effects.

V. CONCLUSION

We study the recoil effects of relativistic mirrors in the form of strongly nonlinear Langmuir waves driven by short intense laser pulses in underdense plasmas. This is important for the question of the feasibility of relativistic mirrors for the development of compact and tunable sources of coherent short-wavelength radiation. Using analytical calculations and PIC simulations, we investigate the properties of the Langmuir wave and the reflected pulse. We also find the threshold for the energy of the laser pulse incident on the electron

density spike above which the relativistic mirror undergoes significant recoil.

We show that the Langmuir wave driven by a short intense laser pulse in uniform plasma decelerates, and therefore, the reflected radiation has a negative chirp. We find that the electric field amplification factor of the reflected radiation reaches its maximum at the moment of wave-breaking. In addition, our results show that for a given intensity of the source pulse, there exists an optimal duration of the source pulse; longer-than-optimal pulses have a lower reflected-to-incident energy ratio. Moreover, for a given Langmuir wave excited by the driver pulse, there exists an optimal intensity of the source pulse, which provides the most intense reflected wave with almost the same frequency upshift factor as in the weak-source approximation.

The sources of coherent high-brightness radiation with wavelengths ranging from x-rays to gamma-rays are of great demand for many practical applications in diverse fields. Relativistic mirrors in laser plasmas can give a promising alternative for the development of radiation sources with tunable parameters at a significantly reduced size and cost in comparison with conventional devices.

ACKNOWLEDGMENTS

This work was supported by the projects “High Field Initiative” (CZ.02.1.01/0.0/0.0/15_003/0000449) from the European Regional Development Fund, “IT4Innovations National Supercomputing Center” (LM2015070) from The Ministry of Education, Youth and Sports of the Czech Republic, JSPS Kakenhi No. JP19H00669 and QST President’s Strategic Grant (Creative Research #20). The EPOCH code was in part funded by the UK EPSRC Grant Nos. EP/G054950/1, EP/G056803/1, EP/G055165/1, and EP/M022463/1.

REFERENCES

- ¹A. Einstein, *Ann. Phys.* **322**, 891 (1905).
- ²S. V. Bulanov, T. Z. Esirkepov, M. Kando, A. S. Pirozhkov, and N. N. Rosanov, *Phys.-Usp.* **56**, 429 (2013).
- ³V. V. Kulagin, V. A. Cherepenin, M. S. Hur, and H. Suk, *Phys. Plasmas* **14**, 113101 (2007).
- ⁴V. V. Kulagin, V. A. Cherepenin, M. S. Hur, and H. Suk, *Phys. Rev. Lett.* **99**, 124801 (2007).
- ⁵T. Z. Esirkepov, S. V. Bulanov, M. Kando, A. S. Pirozhkov, and A. G. Zhidkov, *Phys. Rev. Lett.* **103**, 25002 (2009).
- ⁶J. Meyer-Ter-Vehn and H. C. Wu, *Eur. Phys. J. D* **55**, 433 (2009).
- ⁷S. S. Bulanov, A. Maksimchuk, K. Krushelnick, K. I. Popov, V. Y. Bychenkov, and W. Rozmus, *Phys. Lett., Sect. A* **374**, 476 (2010).
- ⁸H. C. Wu, J. Meyer-Ter-Vehn, J. Fernández, and B. M. Hegelich, *Phys. Rev. Lett.* **104**, 234801 (2010).
- ⁹H. C. Wu, J. Meyer-Ter-Vehn, B. M. Hegelich, and J. C. Fernández, *Phys. Rev. Spec. Top.—Accel. Beams* **14**, 170702 (2011).
- ¹⁰H.-C. Wu and J. Meyer-ter Vehn, *Nat. Photonics* **6**, 304 (2012).
- ¹¹A. Andreev, K. Platonov, and S. Sadykova, *Appl. Sci.* **3**, 94 (2013).
- ¹²D. Kiefer, M. Yeung, T. Dzelzainis, P. S. Foster, S. G. Rykovanov, C. L. Lewis, R. S. Marjoribanks, H. Ruhl, D. Habs, J. Schreiber, M. Zepf, and B. Dromey, *Nat. Commun.* **4**, 1763 (2013).
- ¹³W. J. Ma, J. H. Bin, H. Y. Wang, M. Yeung, C. Kreuzer, M. Streeter, P. S. Foster, S. Cousens, D. Kiefer, B. Dromey, X. Q. Yan, J. Meyer-Ter-Vehn, M. Zepf, and J. Schreiber, *Phys. Rev. Lett.* **113**, 235002 (2014).
- ¹⁴S. V. Bulanov, N. M. Naumova, and F. Pegoraro, *Phys. Plasmas* **1**, 745 (1994).
- ¹⁵R. Lichters, J. Meyer-ter Vehn, and A. Pukhov, *Phys. Plasmas* **3**, 3425 (1996).

- ¹⁶N. M. Naumova, J. A. Nees, I. V. Sokolov, B. Hou, and G. A. Mourou, *Phys. Rev. Lett.* **92**, 63902 (2004).
- ¹⁷T. Baeva, S. Gordienko, and A. Pukhov, *Phys. Rev. E* **74**, 46404 (2006).
- ¹⁸J. Wheeler, A. Borot, A. Malvache, A. Ricci, A. Jullien, R. Lopez-Martens, S. Monchocé, H. Vincenti, and F. Quéré, *Nat. Photonics* **6**, 829 (2012).
- ¹⁹H. Vincenti, *Phys. Rev. Lett.* **123**, 105001 (2019).
- ²⁰A. S. Pirozhkov, S. V. Bulanov, T. Z. Esirkepov, M. Mori, A. Sagisaka, and H. Daido, *Phys. Plasmas* **13**(1), 013107 (2006).
- ²¹A. S. Pirozhkov, S. V. Bulanov, T. Z. Esirkepov, A. Sagisaka, T. Tajima, and H. Daido, “Intensity scalings of attosecond pulse generation by the relativistic-irradiance laser pulses,” in *Ultrafast Optics*, Springer Series in Optical Sciences Vol. 132, edited by S. Watanabe and K. Midorikawa (Springer, New York, 2007), pp. 265–272.
- ²²S. V. Bulanov, T. Esirkepov, and T. Tajima, *Phys. Rev. Lett.* **91**, 85001 (2003).
- ²³M. Kando, Y. Fukuda, A. S. Pirozhkov, J. Ma, I. Daito, L. M. Chen, T. Z. Esirkepov, K. Ogura, T. Homma, Y. Hayashi, H. Kotaki, A. Sagisaka, M. Mori, J. K. Koga, H. Daido, S. V. Bulanov, T. Kimura, Y. Kato, and T. Tajima, *Phys. Rev. Lett.* **99**, 135001 (2007).
- ²⁴A. S. Pirozhkov, J. Ma, M. Kando, T. Z. Esirkepov, Y. Fukuda, L. M. Chen, I. Daito, K. Ogura, T. Homma, Y. Hayashi, H. Kotaki, A. Sagisaka, M. Mori, J. K. Koga, T. Kawachi, H. Daido, S. V. Bulanov, T. Kimura, Y. Kato, and T. Tajima, *Phys. Plasmas* **14**, 123106 (2007).
- ²⁵M. Kando, A. S. Pirozhkov, K. Kawase, T. Z. Esirkepov, Y. Fukuda, H. Kiriyama, H. Okada, I. Daito, T. Kameshima, Y. Hayashi, H. Kotaki, M. Mori, J. K. Koga, H. Daido, A. Y. Faenov, T. Pikuz, J. Ma, L. M. Chen, E. N. Ragozin, T. Kawachi, Y. Kato, T. Tajima, and S. V. Bulanov, *Phys. Rev. Lett.* **103**, 235003 (2009).
- ²⁶M. Lobet, M. Kando, J. K. Koga, T. Z. Esirkepov, T. Nakamura, A. S. Pirozhkov, and S. V. Bulanov, *Phys. Lett., Sect. A* **377**, 1114 (2013).
- ²⁷J. K. Koga, S. V. Bulanov, T. Z. Esirkepov, M. Kando, S. S. Bulanov, and A. S. Pirozhkov, *Plasma Phys. Controlled Fusion* **60**, 074007 (2018).
- ²⁸H. Moghadasin, A. R. Niknam, D. Komaizi, and M. Banjafar, *Phys. Plasmas* **26**, 093105 (2019).
- ²⁹J. Mu, T. Z. Esirkepov, P. Valenta, T. M. Jeong, Y. Gu, J. K. Koga, A. S. Pirozhkov, M. Kando, G. Korn, and S. V. Bulanov, *Phys. Wave Phenom.* **27**, 247 (2019).
- ³⁰J. K. Koga, S. V. Bulanov, T. Z. Esirkepov, A. S. Pirozhkov, M. Kando, and N. N. Rosanov, *Phys. Rev. A* **86**, 53823 (2012).
- ³¹P. Chen and G. Mourou, *Phys. Rev. Lett.* **118**, 45001 (2017).
- ³²S. V. Bulanov, T. Esirkepov, V. S. Khoroshkov, A. V. Kuznetsov, and F. Pegoraro, *Phys. Lett., Sect. A* **299**, 240 (2002).
- ³³R. Neutze, R. Wouts, D. Van Der Spoel, E. Weckert, and J. Hajdu, *Nature* **406**, 752 (2000).
- ³⁴F. Krausz and M. Ivanov, *Rev. Mod. Phys.* **81**, 163 (2009).
- ³⁵S. V. Bulanov, T. Z. Esirkepov, Y. Hayashi, H. Kiriyama, J. K. Koga, H. Kotaki, M. Mori, and M. Kando, *J. Plasma Phys.* **82**, 905820308 (2016).
- ³⁶E. Esarey, C. B. Schroeder, and W. P. Leemans, *Rev. Mod. Phys.* **81**, 1229 (2009).
- ³⁷A. Akhiezer and R. Polovin, Sov. Phys. JETP **3**, 696 (1956).
- ³⁸*Handbook of Mathematical Functions*, edited by M. Abramowitz and I. A. Stegun, Applied Mathematical Series, Vol. 55 (National Bureau of Standards, Washington, 1964).
- ³⁹T. D. Arber, K. Bennett, C. S. Brady, A. Lawrence-Douglas, M. G. Ramsay, N. J. Sircombe, P. Gillies, R. G. Evans, H. Schmitz, A. R. Bell, and C. P. Ridgers, *Plasma Phys. Controlled Fusion* **57**, 113001 (2015).
- ⁴⁰S. V. Bulanov, I. N. Inovenkov, N. M. Naumova, and A. S. Sakharov, Sov. J. Plasma Phys. **16**, 444 (1990).
- ⁴¹B. Fidel, E. Heyman, R. Kastner, and R. W. Ziolkowski, *J. Comput. Phys.* **138**, 480 (1997).
- ⁴²K. S. Yee, *IEEE Trans. Antennas Propag.* **14**, 302 (1966).
- ⁴³R. Courant, K. Friedrichs, and H. Lewy, *Math. Ann.* **100**, 32 (1928).
- ⁴⁴A. Savitzky and M. J. Golay, *Anal. Chem.* **36**, 1627 (1964).
- ⁴⁵S. V. Bulanov, I. N. Inovenkov, V. I. Kirsanov, N. M. Naumova, and A. S. Sakharov, *Phys. Fluids B* **4**, 1935 (1992).
- ⁴⁶F. W. King, *Hilbert Transforms*, Encyclopedia of Mathematics and its Applications Vol. 2 (Cambridge University Press, 2009).

B.4 Relativistic flying forcibly oscillating reflective diffraction grating

The following article is reproduced from Mu, J., Esirkepov, T. Z., Valenta, P., Gu, Y., Jeong, T. M., Pirozhkov, A. S., Koga, J. K., Kando, M., Korn, G., and Bulanov, S. V. (2020). [Relativistic flying forcibly oscillating reflective diffraction grating](#). *Physical Review E*, **102**(5):053202, with the permission of APS.

Copyright © 2020 American Physical Society.

Relativistic flying forcibly oscillating reflective diffraction grating

Jie Mu,¹ Timur Zh. Esirkepov^{1,2,*} Petr Valenta^{1,3} Yanjun Gu,¹ Tae Moon Jeong^{1,4} Alexander S. Pirozhkov^{1,5}
James K. Koga^{1,6} Masaki Kando^{1,2} Georg Korn,¹ and Sergei V. Bulanov^{1,2}

¹ELI Beamlines Project, Institute of Physics of the ASCR, Na Slovance 2, 18221 Prague, Czech Republic

²Kansai Photon Science Institute, National Institutes for Quantum and Radiological Science and Technology, 8-1-7 Umemidai, Kizugawa, Kyoto 619-0215, Japan

³Faculty of Nuclear Sciences and Physical Engineering, Czech Technical University in Prague, Brehova 7, 11519 Prague, Czech Republic



(Received 30 June 2020; accepted 8 October 2020; published 2 November 2020)

Relativistic flying forcibly oscillating reflective diffraction gratings are formed by an intense laser pulse (driver) in plasma. The mirror surface is an electron density singularity near the joining area of the wake wave cavity and the bow wave; it moves together with the driver laser pulse and undergoes forced oscillations induced by the field. A counterpropagating weak laser pulse (source) is incident at grazing angles, being efficiently reflected and enriched by harmonics. The reflected spectrum consists of the source pulse base frequency and its harmonics, multiplied by a large factor due to the double Doppler effect.

DOI: [10.1103/PhysRevE.102.053202](https://doi.org/10.1103/PhysRevE.102.053202)

I. INTRODUCTION

Bright sources of electromagnetic radiation with the spectral range from extreme ultraviolet to x rays have attracted a great deal of attention because of their great potential for both fundamental science and practical applications (e.g., in biology, medicine, and materials science) [1,2]. One of the ways toward developing ultrashort intense electromagnetic pulse sources is a simultaneous frequency upshift and pulse compression. This occurs in the reflection of an electromagnetic wave from a fast approaching mirror, which is a manifestation of the double Doppler effect. According to the Einstein prediction [3], in the head-on wave-mirror collision, the reflected electromagnetic pulse is compressed and its frequency is upshifted by the same factor $(c + v_M)/(c - v_M) \approx 4\gamma_M^2$, where v_M is the mirror velocity, c is the speed of light in vacuum, and $\gamma_M = (1 - v_M^2/c^2)^{-1/2}$ is the mirror Lorentz factor.

There are a few physical realizations of this concept. Perhaps the earliest are the electromagnetic wave reflection at a moving relativistic electron slab [4] and at moving ionization fronts [5–7].

A potentially high repetition generation of frequency-upshifted high-intensity quasimonochromatic electromagnetic pulses [8–11] uses a laser-driven breaking wake wave in underdense plasma as the relativistic flying mirrors (RFMs) which reflect, compress, and focus a counterpropagating laser pulse (for details see the reviews in [12,13] and references therein). An increase of the intensity of counterpropagating laser pulses modifies this scheme, adding generation of high-order harmonics at the mirror [14]; the spectrum of the reflected light consists of harmonics of the incident pulse base frequency, all multiplied by approximately $4\gamma_M^2$.

The flying mirror can be a laser-accelerated thin electron layer ejected by an intense laser pulse from a thin foil [15]. An ensemble of flying mirrors producing high-intensity attosecond pulses is realized by electron layers consequently ejected at every period of the intense incident laser [16]. Due to multiple reflections on many semitransparent electron layers, the conversion efficiency can be as high as $4\gamma_M^2 \gg 1$, where energy is gained via the momentum transfer from the flying electron layers to the reflected radiation [16].

The relativistic oscillating mirrors (ROMs) are formed at the surface of an overdense plasma, when a strong laser field both induces the nonlinearly oscillating electron density modulations and gets reflected off them, producing high-order harmonics [17–19]. When a dense plasma slab is accelerated by a high-contrast ultraintense laser pulse in the regime of radiation pressure dominant acceleration, it gains energy as a receding mirror and acts as an approaching mirror for a counterpropagating intense laser pulse [20]; in addition, it acts as a relativistic oscillating mirror in the comoving reference frame so that the reflected radiation contains high-order harmonics, upshifted due to the double Doppler effect.

Here we present a physical realization of the relativistic mirror, the relativistic flying forcibly oscillating mirror (RFFOM). It appears as a surface of high electron density corresponding to a folding singularity created by an intense laser pulse propagating in plasma. Being modulated by the laser field, this surface acts as a reflective diffraction grating for a counterpropagating electromagnetic wave.

The paper is organized as follows. In Sec. II the mechanism of the RFFOM concept is introduced. Section III gives a simplified theory based on the assumption of an inclined ideal flat mirror. Section IV introduces the simulation setup and the basic parameters. In Secs. V and VI we analyze the properties of the reflected wave and its spectrum using a three-dimensional (3D) simulation and high-resolution 2D simulations, respectively. In Sec. VII the influence of thermal

*timur.esirkepov@qst.go.jp

effects on the RFFOM is investigated. Section VIII summarizes the results and discusses possible applications of the concept.

II. RFFOM MECHANISM

An intense laser pulse propagating in underdense plasma excites wake waves [21–23]. The laser field pushes electrons not only along the laser axis, but also aside, creating a cavity void of electrons. Depending on the relation between the kinetic energy of transversely pushed electrons $\mathcal{E}_{e\perp}$ and the electrostatic potential of the cavity φ , one can see three patterns of the first wake wave period. When $\mathcal{E}_{e\perp} \ll e\varphi$, the cavity rear has a smooth surface, which can be used as a RFM [8]. Here e is the electron charge. For $\mathcal{E}_{e\perp} \gtrsim e\varphi$, electrons forming the cavity wall overshoot the axis at the cavity rear, which causes the transverse wake wave breaking [24], playing an important role in the electron injection into the acceleration phase of the wake wave. A tightly focused laser pulse can push electrons so that $\mathcal{E}_{e\perp} \gg e\varphi$ and electrons form a bow wave [25], which detaches from the cavity wall in the head of the laser pulse. A propagation of transversely pushed electrons through unperturbed electrons is a multistream flow. In the approximation of a continuous electron fluid, such flows have density singularities whose existence, universality, and structural stability are explained by catastrophe theory [26]. The fold singularity corresponds to the electron density jumps at the cavity wall and bow wave boundary. At their joining, the electron density is even higher and corresponds to the cusp singularity. The fold singularity is indeed a fold of the phase distribution of initially unperturbed electrons, projected into a space to form the density distribution [27–29].

The cusp and the adjacent folds act as a pair of mirrors joined at some angle (cusped mirror), which undergoes forced oscillations induced by the laser field (Fig. 1). It partially reflects a counterpropagating electromagnetic wave (source). The reflected radiation is enriched by high-order harmonics, because the cusped mirror is oscillating, like ROMs [17], and all of the reflected spectrum is upshifted because the cusped mirror moves with a high speed, like RFMs [8]. Moreover, the source can have a grazing incidence on the mirror surfaces, because at the point of the bow wave detachment from the cavity wall, the surfaces of the highest electron density can make a relatively small angle with respect to the laser axis. These angles can be controlled by the laser focal spot size and initial plasma density, in accordance with the condition of the bow wave formation [25]. As is known, the smaller the grazing incidence angle, the higher the reflection efficiency. In our case, however, the increase of the reflection efficiency is accompanied by a decrease of the frequency upshift factors.

The cusped mirror is a RFFOM, combining the properties of a RFM and a ROM. The surface of the cusped mirror is periodically modulated by the laser field; therefore, the cusped mirror has the properties of a reflective diffraction grating.

A source laser pulse is reflected from the cusped mirror; high-order harmonics are generated due to the mirror oscillations as in ROMs and the whole reflected spectrum is upshifted as in RFMs. The reflected radiation goes at discrete angles corresponding to the diffraction orders of a relativistic flying reflective diffraction grating. The feasibility of the

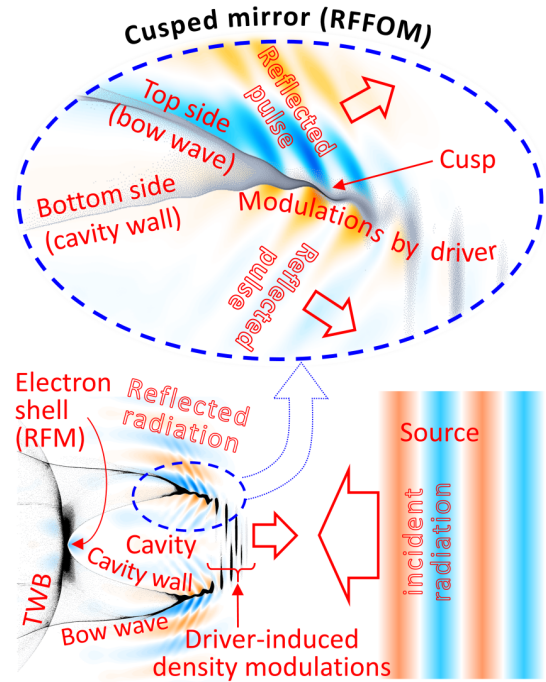


FIG. 1. The RFFOM scheme. On the bottom the driver pulse (not shown but revealed via density modulations) creates a cavity and bow wave in underdense plasma (2D PIC simulation of Sec. VI). Over-shooting electrons cause transverse wave breaking (TWB). Shown on top is a close-up of the area near the cusp. A counterpropagating source pulse is reflected off the sides of the cusped mirror, forcibly oscillating under the action of the driver. The blue-red color scale is for the electric field and grayscale is for the electron density.

above-described RFFOM is demonstrated using 2D and 3D particle-in-cell (PIC) simulations.

We note that the cusp and the portions of adjacent folds have their own self-emission [27–30] when only the driver pulse is present. In particular, the cusp emits high-frequency electromagnetic radiation in a cone around the vector of the average velocity of the cusp. The constructive interference is gained only for wavelengths which are emitted by the regions having size shorter than the wavelength in the radiation propagation direction. This condition is always satisfied for the cusp singularity. In analogy with the moving oscillating charge, the cusp emits the high-order harmonics observed in experiments [27–29]. Here we do not consider this self-emission. In the simulations shown below, the source pulse and consequently the reflected pulse have different polarization with respect to the driver and the reflected radiation disappears in the absence of the source.

III. MODEL

In order to analyze the base frequency and direction angle of electromagnetic radiation reflected from the cusped mirror, we use a simplified model, neglecting oscillations of the mirror surface (Fig. 2). We consider a moving ideal flat mirror in a 2D space (x, y), where the mirror velocity vector is $\{\beta c, 0\}$, with $\beta = v_M/c$. The mirror is inclined with respect to its velocity; the normal vector to its surface

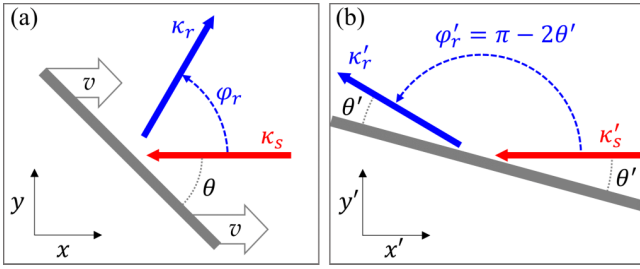


FIG. 2. Positional relationship of the moving inclined mirror, and incident and reflected waves in the (a) laboratory and (b) comoving reference frames.

is $\{\sin \theta, \cos \theta\}$. A counterpropagating electromagnetic wave with frequency ω_s is incident on the mirror; its wave number vector is $\kappa_s = \{-\omega_s/c, 0\}$. The reflected electromagnetic wave has a frequency of ω_r and a wave number vector of $\kappa_r = (\omega_r/c)\{\cos \phi_r, \sin \phi_r\}$.

The parameters of the reflected wave are obtained by changing to the reference frame of the mirror, considering specular reflection, and changing back to the laboratory reference frame

$$\omega_r = \omega_s \frac{1 + \beta}{1 - \beta \cos \phi_r}, \quad (1)$$

$$\cos \phi_r = \frac{(1 + \beta)^2 \tan^2(\theta) - 1}{(1 + \beta)^2 \tan^2(\theta) + 1}. \quad (2)$$

For large values of $\gamma = (1 - \beta^2)^{-1/2} \rightarrow \infty$ and fixed angle $0 \leq \theta \leq \pi/2$, we have

$$\omega_r = \omega_s \frac{5 - 3 \cos 2\theta}{1 + \cos 2\theta} - O\left(\frac{1}{\gamma^2}\right), \quad (3)$$

$$\cos \phi_r = \frac{3 - 5 \cos 2\theta}{5 - 3 \cos 2\theta} + O\left(\frac{1}{\gamma^2}\right). \quad (4)$$

We note that the expansion of Eq. (3) diverges for $\theta \rightarrow \pi/2$ (i.e., for near-normal incidence). Nevertheless, the larger the γ , the greater the well-approximated threshold for θ ; for example, for $\gamma = 10$, the approximation is good for $0 \leq \theta \leq \pi/4$ with the maximum (overestimation) error of 2%. In Eq. (4) the expansion is valid for the whole interval of $0 \leq \theta \leq \pi/2$; for example, for $\gamma = 10$, the maximum (overestimation) error is 0.25%. In the limit of the glancing angle $\theta \rightarrow 0$, reflection does not occur: $\omega_r \rightarrow \omega_s$ and $\cos \phi_r = -1$.

According to Eqs. (3) and (4), for large γ , the mirror inclined at $\theta = \arccos(\frac{3}{5})/2 \approx 26.6^\circ$ reflects radiation at 90° with frequency $\omega_r \approx 2\omega_s$. If the driver pulse is sufficiently intense and tightly focused (e.g., due to relativistic self-focusing), the transversely pushed electrons move with relativistic velocity. Since the driver velocity is also relativistic, the bow wave outer boundary makes an angle of $\theta \approx 45^\circ$ with the laser axis [25]. In this case, from the expansions in Eqs. (3) and (4) we obtain $\omega_r \approx 5\omega_s$ and $\phi_r \approx \arccos(\frac{3}{5}) \approx 53^\circ$, independent of the mirror velocity for sufficiently large γ .

Equation (1) represents an ellipse in polar coordinates (ω_s, ϕ_r) [9]. In the coordinates (k_x, k_y) , which are the components of the reflected wave number vector $\kappa_r = \{k_x, k_y\}$, we have $\omega_r = c(k_x^2 + k_y^2)^{1/2}$ and $\phi_r = \arctan(k_y/k_x)$, so the

leftmost focus of the ellipse is at $(0,0)$ and the major axis coincides with the x axis; the leftmost point of the ellipse is $\omega_r|_{\phi_r=\pi} = \omega_s$, which means transmitted radiation; the rightmost point of the ellipse is $\omega_r|_{\phi_r=0} = \omega_s(1 + \beta)/(1 - \beta) \approx 4\gamma^2\omega_s$, which means exactly backward reflection. If there exist harmonics of the base frequency, each harmonic order sits on its own ellipse with the same leftmost focus.

If the source pulse has sufficiently low frequency, its wavelength inside the plasma is significantly longer than in vacuum, $\tilde{\lambda}_s = \lambda_s(1 - \omega_{pe}^2/\omega_s^2)^{-1/2}$, where $\omega_{pe} = \sqrt{4\pi e^2 n_e/m_e}$ is the Langmuir frequency. Here n_e is the electron density and m_e is the electron mass. In this situation, Eq. (1) becomes [12]

$$\omega_r = \frac{\psi_s + \beta \cos(\phi_r) \sqrt{\psi_s^2 - \omega_{pe}^2(1 - \beta^2 \cos^2 \phi_r)}}{1 - \beta^2 \cos^2 \phi_r}, \quad (5)$$

$$\psi_s = \omega_s + \beta \sqrt{\omega_s^2 - \omega_{pe}^2} \quad (6)$$

and the reflection angle is determined by the relation

$$\frac{\sin \phi_r}{\cos(\phi_r) - \beta \beta_{s,ph}} = \frac{2\gamma^2 \tan \theta}{\tan^2(\theta) - \gamma^2}, \quad (7)$$

where $\beta_{s,ph} = v_{s,ph}/c > 1$ is the normalized phase velocity of the source pulse,

$$\begin{aligned} \beta_{s,ph} &= \omega_r / \sqrt{\omega_r^2 - \omega_{pe}^2} \\ &= \frac{\psi_s + \beta \cos(\phi_r) \sqrt{\psi_s^2 - \omega_{pe}^2(1 - \beta^2 \cos^2 \phi_r)}}{\psi_s \beta \cos(\phi_r) + \sqrt{\psi_s^2 - \omega_{pe}^2(1 - \beta^2 \cos^2 \phi_r)}}. \end{aligned} \quad (8)$$

In the limit $\omega_{pe} \rightarrow 0$ and $\psi_s \rightarrow (1 + \beta)\omega_s$, Eq. (5) reduces to Eq. (1). According to Eq. (5), the maximum frequency upshift (at $\phi_r = 0$) in plasma is slightly less than that in vacuum,

$$\begin{aligned} \omega_r|_{\phi_r=0} &= \gamma^2 (\psi_s + \beta \sqrt{\psi_s^2 - \omega_{pe}^2/\gamma^2}) \\ &< \gamma^2 (1 + \beta) \psi_s. \end{aligned} \quad (9)$$

IV. SIMULATION SETUP

To study the laser plasma interaction under the conditions when the bow wave is formed, we carry out 2D and 3D PIC simulations using the EPOCH code [31] and REMP code [32]. The plasma is fully ionized and homogeneous. The ion response is neglected due to a large ion-to-electron mass ratio, relatively low electron density, and a short time of the considered interaction. The electron density is $n_e = 1.14 \times 10^{19} \text{ cm}^{-3} \times (1 \text{ } \mu\text{m}/\lambda_d)^2 = 0.01 n_c$, where $n_c = \pi/r_e \lambda_d^2 = 1.115 \times 10^{21} \text{ cm}^{-3} \times (1 \text{ } \mu\text{m}/\lambda_d)^2$ is the critical density, $r_e = e^2/m_e c^2$ is the classical electron radius, and $\lambda_d = 2\pi c/\omega_d$ is the wavelength, with ω_d the frequency of the driver laser and c the speed of light in vacuum.

The driver laser pulse is linearly polarized with its electric field vector along the y axis and its dimensionless amplitude is $a_d = eE_d/m_e \omega_d c = 6.62$, corresponding to an intensity of $I_d = 6 \times 10^{19} \times (1 \text{ } \mu\text{m}/\lambda_d)^2 \text{ W/cm}^2$, where E_d is the maximum electric field of the driver. Its full width at half maximum is $5\lambda_d \times 5\lambda_d$ (along the x and y axes) in 2D simulations and $10\lambda_d \times 4\lambda_d \times 4\lambda_d$ (along the x , y , and z axes) in the 3D

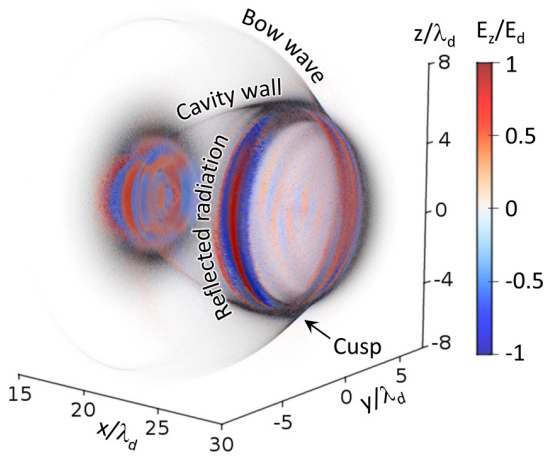


FIG. 3. Wake wave cavity, bow wave, and cusp seen in the electron density distribution (in grayscale). The reflected electric field normalized to that of the driver E_d is shown by the blue-red color scale.

simulation. The driver focus is at the left boundary of the simulation box. In the 3D simulation, the transverse sizes of the driver and source laser pulses are less than in 2D simulations due to the limited computational resources.

The source laser pulse has perpendicular polarization; its electric field vector is along the z axis. This helps to distinguish the driver, the source, and the reflected radiation, as was done in previous publications [8]. Moreover, it helps to distinguish the reflected signal from the cusp self-emission. The source has a longer wavelength $\lambda_s = 8\lambda_d$. This helps to more easily resolve and analyze the strongly upshifted reflected radiation enriched with high-order harmonics with limited computing resources. The source pulse dimensionless amplitude is $a_s = 0.05$, corresponding to an intensity of $I_s = 5.35 \times 10^{13} \text{ W/cm}^2$. It is sufficiently weak in order not to affect the motion and structure of the cusped mirror [33]. Its full width at half maximum is $8\lambda_d \times 20\lambda_d$ in 2D simulations and $8\lambda_d \times 10\lambda_d \times 10\lambda_d$ in the 3D simulation. Its transverse size is large enough to see reflection from bow waves.

The simulation results are shown in Figs. 7(a), where Figs. 3 and 4 represent 3D simulation while Figs. 5–9 show 2D simulations with similar parameters. In the following $T_d = \lambda_d/c$ is the period of the driver laser cycle.

V. 3D SIMULATION

An excitation of the wake wave and bow wave by the driver pulse, the formation of the cavity, and the reflection of the source pulse from the cusped mirror can be seen in the 3D PIC simulation (Fig. 3). Here the simulation box has a size of $30\lambda_d \times 30\lambda_d \times 30\lambda_d$. The spatial grid mesh is $\Delta x/\lambda_d = \frac{1}{30}$, $\Delta y/\lambda_d = \frac{1}{30}$, and $\Delta z/\lambda_d = \frac{1}{30}$. Plasma uniformly fills the cube with coordinates of $0\lambda_d \leq x \leq 30\lambda_d$, $-15\lambda_d \leq y \leq 15\lambda_d$, and $-15\lambda_d \leq z \leq 15\lambda_d$. The total number of quasiparticles is 5.7×10^8 .

The reflected radiation in Fig. 3 is computed as follows. First, the difference is taken between the electromagnetic fields in two separate simulations, one with the source pulse and another without it. The electromagnetic field obtained in

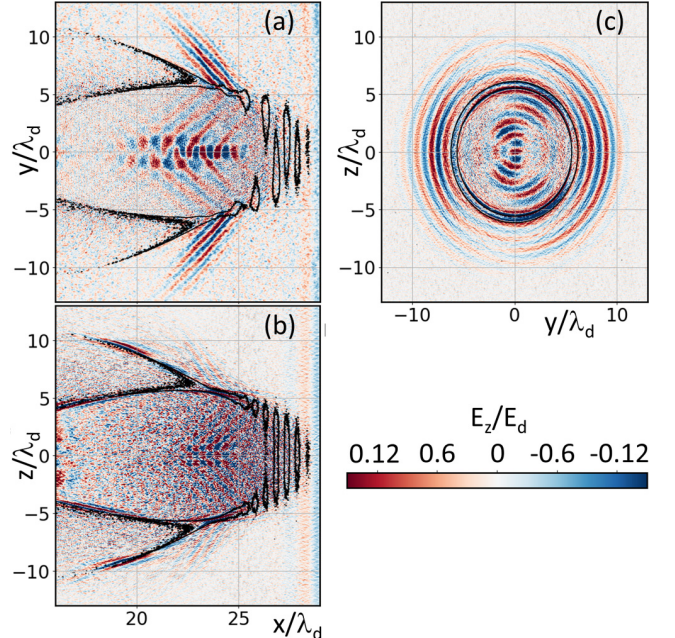


FIG. 4. Cross sections of the box shown in Fig. 3 along the planes (a) $(x, y, z = 0)$, (b) $(x, y = 0, z)$, and (c) $(x = 22.5, y, z)$. The blue-red color scale for the electric field normalized to that of the driver E_d contours for electron density.

this way represents the incident source pulse together with the reflected radiation [10]. Second, the low-frequency component is filtered out, thus the field representing the source pulse is removed so that the remaining component corresponds to the reflected radiation.

As can be seen in Figs. 3 and 4(a), reflection occurs in the regions of high electron density. Reflection starts at the cusp, a location where the cavity wall joins the outline of the bow wave. Then it happens at the rear of the cavity. The latter is a realization of the RFM by the breaking wake wave, as described in Ref. [8].

Here we focus on the reflection at the cusp. As can be seen in Figs. 4(a) and 4(c), the reflected radiation goes at some angle off axis, from both sides of the cusped mirror near the cusp, in the form of two short-wavelength pulses: An outer pulse initially goes outside the cavity and an inner pulse initially goes inside the cavity. As expected, the reflected radiation wavefronts correspond to a conical mirror; in particular, the cross section in the plane of the driver axis and polarization demonstrates a nearly flat wave front cross section [Fig. 4(a)], in agreement with the model assumption in Sec. III. These fronts certainly become almost spherical when the reflected pulses propagate at a distance much greater than their width.

The frequency upshift of the reflected radiation is obvious: The reflected pulse wavelength is significantly shorter than the electron density modulation induced by the driver, which in turn is much shorter than the source pulse wavelength ($\omega_s = \omega_d/8$). We note that the outer pulse has a shorter wavelength than the inner pulse, in accordance with their propagation direction, which corresponds to reflection from different sides of

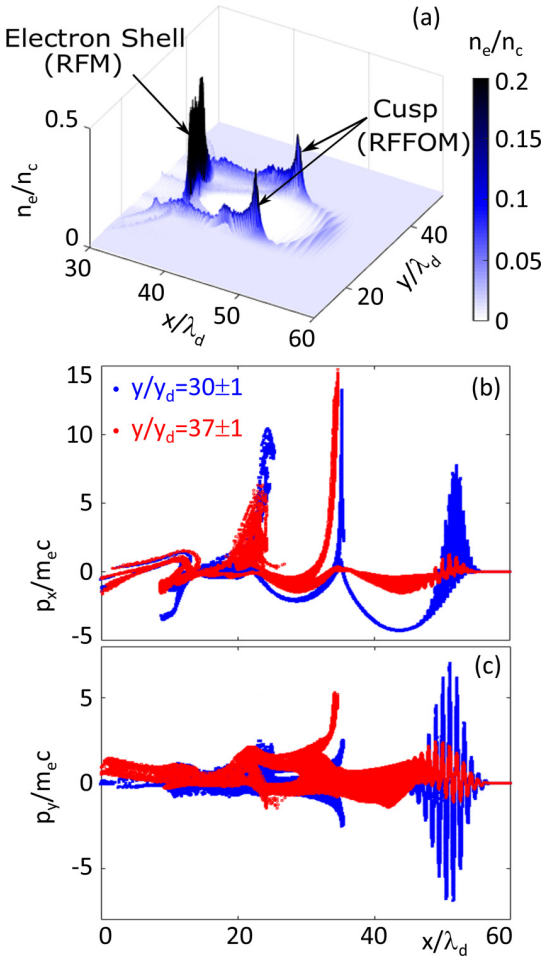


FIG. 5. (a) Electron density distribution in the (x, y) plane at $t = 54T_d$. (b) Longitudinal p_x and (c) transverse p_y electron momenta vs the x coordinate, for electrons in the strip near the axis $29\lambda_d \leq y \leq 31\lambda_d$ (blue) and in the strip containing the cusp $36\lambda_d \leq y \leq 38\lambda_d$ (red).

the cusped mirror with different inclination angle with respect to the driver axis.

Near the cusp, the electron density is comparable to that at the cavity rear, at the breaking point of the wake wave. Both the cusped mirror and the electron shell at the cavity rear provide efficient reflection due to strong localization of electrons. In addition, grazing incidence enhances the cusped mirror reflectivity, although at the expense of the greater off-axis reflection angle and correspondingly the lower frequency upshift factor, as follows from the model in Sec. III.

VI. HIGH-RESOLUTION 2D SIMULATIONS

In order to see the spectral properties of the reflected radiation, we performed 2D PIC simulations in the moving window with higher resolution, for a grid mesh size of $\Delta x/\lambda_d = 1/1024$ and $\Delta y/\lambda_d = 1/256$. The conical cusped mirror seen in the 3D simulation appears in 2D simulation as two cusped mirrors [Fig. 5(a)], analogously to the cross section in Fig. 4(a). We note that the cusp maintains a stable structure for more than 150 driver laser cycles. The cusped

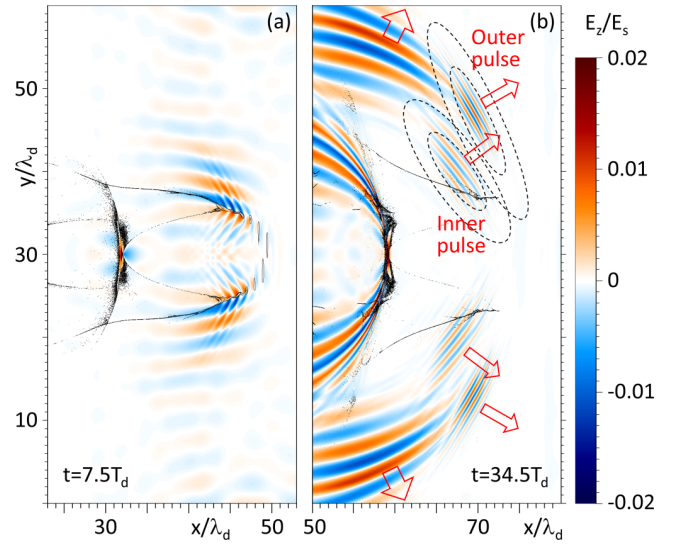


FIG. 6. Electric field E_z after the high-pass filter, for $\omega \geq 2\omega_s$, at (a) $7.5T_d$ and (b) $34.5T_d$. The black thin curves correspond to electron densities of $0.03n_c$, $0.04n_c$, and $0.05n_c$. Arrows show the propagation direction. Dashed ellipses show the reflected outer and inner pulses selected for spectrum analysis by the Gaussian spatial filters: The filter value is 0.999 for small ellipses and 10^{-6} for larger ones.

mirror is a phase object; at each moment of time, it consists of different electrons, continuously flowing through it [29].

Figures 5(b) and 5(c) display the longitudinal p_x and transverse p_y momenta, respectively, for the electrons in different regions. The electrons located near the driver axis in a strip bounded as $29\lambda_d \leq y \leq 31\lambda_d$ (shown in blue) demonstrate well-known patterns of the wake wave behind an intense short laser pulse. Characteristic modulations induced by the driver field indicate the location of the driver pulse. Longitudinal wave breaking is seen at $x \approx 22\lambda_d$ and $x \approx 35\lambda_d$ in Fig. 5(b); transverse wave breaking is seen at $x \approx 33.5\lambda_d$ in Fig. 5(c).

The momentum distributions of electrons at the periphery, in the strip containing the cusp ($36\lambda_d \leq y \leq 38\lambda_d$), are shown in red in Figs. 5(b) and 5(c). For electrons near the cusp, the longitudinal momentum p_x is negative [Fig. 5(b)], which means that these electrons move backward with respect to the x axis, in striking contrast to the motion of the cusp in the forward direction. The transverse momentum p_y of electrons near the cusp fills a relatively wide strip stretching from negative to positive values [Fig. 5(c)], which indicates a multistream flow.

Upon reflection from the cusped mirror, the source pulse transforms into several well-separated pulses with different wavelength and propagation direction, as seen in Fig. 6. Reflected pulses are almost bilaterally symmetric with respect to the x axis, which correlates with the approximate reflection symmetry of the cavity, bow waves, and cusps.

The pulses with the longest wavelength (the lowest frequency) are seemingly reflected from the outer side of the cusped mirror (farthest from the driver axis). They have a frequency multiplication factor of approximately 2.6 and propagate at an angle of approximately 75° with respect to the x axis, in accordance with the asymptotes in Eqs. (1) and (2).

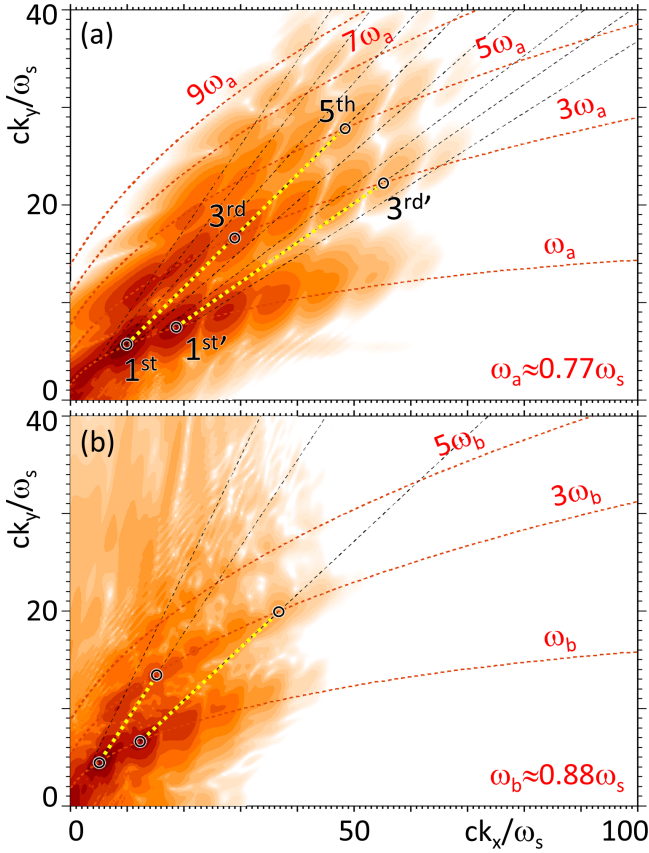


FIG. 7. Frequency spectrum of the (a) outer and (b) inner pulses selected by the Gaussian spatial filter shown in Fig. 6(b). Red dashed curves represent the frequency upshift dependence on the reflection angle $\phi_r = \arctan(k_y/k_x)$ [Eq. (5)], where ω_s is replaced by the odd harmonics of ω_a and ω_b . Radial black dotted lines are for (a) $22^\circ \pm 1.8^\circ$, $30^\circ \pm 3^\circ$, 37° , and 41° and (b) 28.5° , 41.5° , and 50° . Black circles emphasize the peaks in the frequency spectrum corresponding to the harmonics and diffraction orders.

The pulses with the shorter wavelengths (higher frequencies) are reflected from both sides of the cusped mirror. The outer pulse propagates away from the x axis, while the inner pulse initially propagates toward the x axis. In the upper half plane in Fig. 6(b), the outer pulse originates from the top of the cusped mirror at $y > 30\lambda_d$, while the inner pulse originates from top of the cusped mirror at $y < 30\lambda_d$.

The strikingly different wavelength and propagation direction of the reflected well-separated pulses indicate that reflection occurs at a relativistic flying reflective diffraction grating. In addition to a specularly reflected wave, the grating diffracts the incident wave at different angles. Due to the Doppler effect, the frequency upshift factor is greater for smaller diffraction (reflection) angles, according to Eqs. (1) and (5).

The outer and inner pulses contain high-order harmonics due to oscillations of the reflecting facets of the cusped mirror imposed by the driver laser. Their spatial spectra are shown in Fig. 7. The spectra resemble an opened folding fan. The distribution of the electromagnetic energy density is discretized with respect to both the angle and the wave number

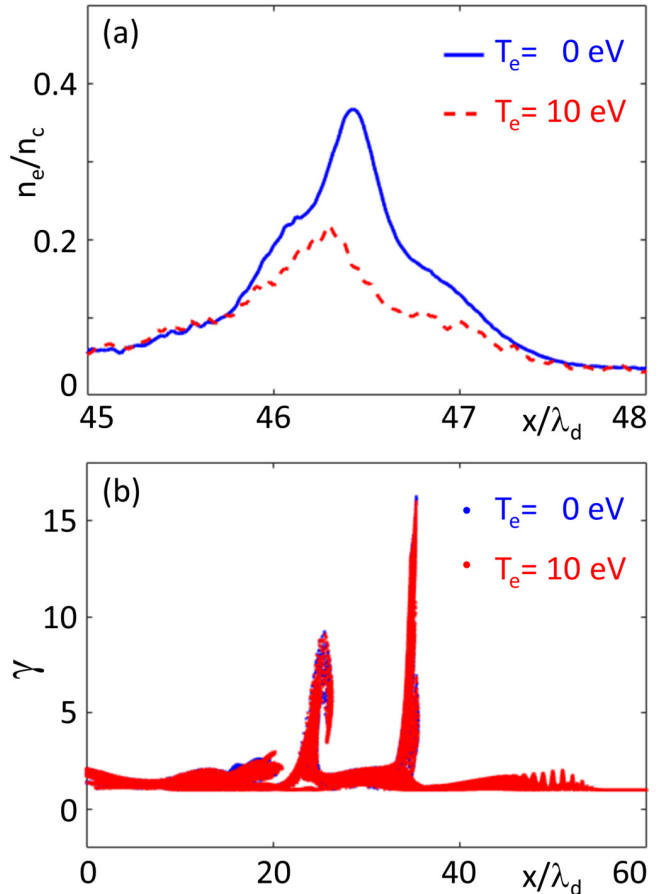


FIG. 8. (a) Cross section of the electron density near the cusp at $y = 36.67\lambda_d$ and (b) the Lorentz factor γ of electrons near the cusp in the strip bounded as $36 \leq y \leq 38\lambda_d$, for two simulations with different initial electron temperature. The result for $T_e = 0$ eV is marked in blue (hardly visible); the result for $T_e = 10$ eV is marked in red.

(or frequency). The discretization with respect to the angle corresponds to the property of the cusped mirror to act as a reflective diffraction grating. The discretization with respect to the wave number (or frequency) reveals high-order harmonic generation due to the cusped mirror oscillations induced by the driver pulse. The well-separated hot spots in Fig. 7 represent diffraction orders along the angle and harmonic orders along the wave number (or frequency).

The cusped mirror moves with the velocity close to the group velocity of the driver pulse, $\beta = \sqrt{1 - \omega_{pe}^2/\omega_d^2} \approx 0.995$; the corresponding Lorentz factor is $\gamma = \omega_d/\omega_{pe} = 10$. The source pulse has a relatively low frequency; therefore, its wavelength inside plasma is longer than in vacuum, $\tilde{\lambda}_s \approx 1.67\lambda_s$. According to Eq. (5), the frequency upshift factor for radiation reflected at 30° with respect to the driver pulse axis is $\omega_r/\omega_s \approx 11.4$. This is in good agreement with the position of the first harmonic (hot spot) emitted at the above-specified angle in Fig. 7(a). The hot spots are arranged along curves close to ellipses defined by Eq. (5). Each curve corresponds to an odd harmonic of somewhat downshifted frequency of the source pulse.

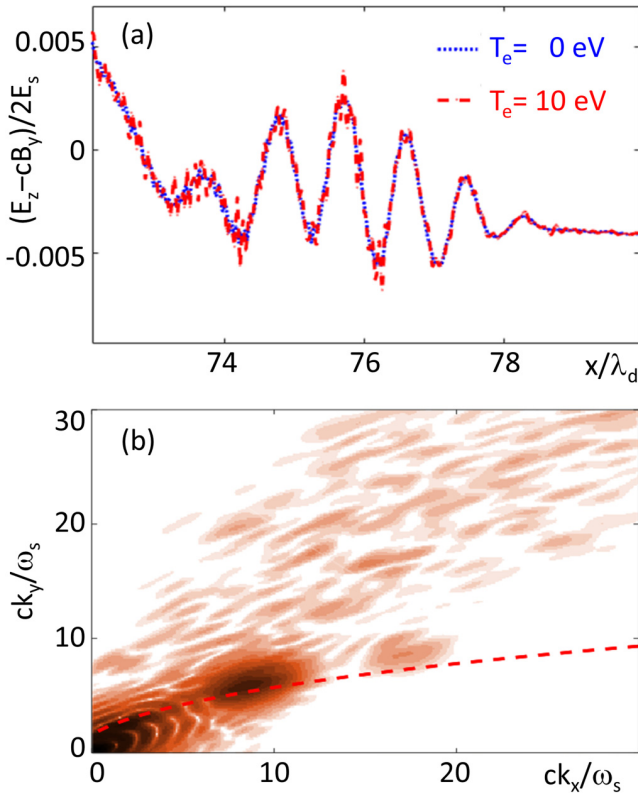


FIG. 9. (a) Combination of the electromagnetic field components $E_z - cB_y$, approximately representing reflected radiation, at $y = 52\lambda_d$. The blue dotted curve shows the initial electron temperature $T_e = 0$ eV (blue) and the red dashed line $T_e = 10$ eV. (b) Frequency spectrum of the outer pulse (color scale) and the ellipse representing the frequency upshift dependence (red dashed curve) as in Fig. 7(a), but for the initial electron temperature $T_e = 10$ eV.

The energy of the outer pulse is estimated as $\mathcal{E}_{\text{OP}} = 2.1 \times 10^{-7}$ J, or 0.53% of the source pulse. The corresponding number of photons is $\mathcal{N}_{\text{OP}} = 6.4 \times 10^{11}$. The reflection efficiency increases with the intensity of the driver pulse. For a driver pulse intensity of $I_d^{\text{PW}} = 5.4 \times 10^{20}$ W/cm², the outer pulse amplitude becomes 1.21×10^{10} V/m, 30.25% of the incident source pulse. The energy and number of photons increase to $\mathcal{E}_{\text{OP}}^{\text{PW}} = 2.05 \times 10^{-6}$ J (1.02% of the source) and $\mathcal{N}_{\text{OP}}^{\text{PW}} = 5.17 \times 10^{12}$, respectively.

The reflectivity of the RFFOM seen in simulations requires further analytical investigation. Neglecting the forced oscillations of the mirror and correspondingly the generation of high-order harmonics, as in the model discussed in Sec. III, one can use the analytical results of Ref. [34] to calculate the reflectivity of various electron density singularities. Here the reflecting singularity consists of the cusp and two folds; the nearly flat fronts of the reflected radiation near the cusped mirror in Figs. 4(a) and 6 indicate that for such fronts the reflecting entity is a fold singularity.

VII. THERMAL EFFECTS

In the description above, the initial electron temperature is assumed to be zero. Thermal effects on the RFM are analyzed

in Refs. [35–37]. An important factor for RFM wave breaking due to thermal effects can be mitigated by using tailored underdense plasma [38].

We note that the electron temperature in the location of an intense femtosecond laser pulse during its propagation in underdense plasma has not been measured in experiments; the estimates mentioned in the literature are based on the time-integrated observations with a typical timescale greater than 100 fs (e.g., Ref. [39]). In contrast, there are experimental measurements inconsistent with the assumption of a significant electron temperature at the location of a femtosecond laser pulse. They are represented by (i) a direct observation of a subtle structure of the wake wave by frequency-domain holography [40] and a femtosecond probe pulse [41], (ii) the measurements of the reflected spectrum and reflectivity of the RFM [9–11], and (iii) the detection of harmonics well resolved up to an order of a few hundredths from the laser self-focusing position [27,28,42] and the observation of a submicrometer pointlike sources of these harmonics [29].

In order to see how the electron temperature in the wake field modifies our scheme, we performed an additional 2D PIC simulation with an initial electron temperature of $T_e = 10$ eV along the y-axis direction. As can be seen in Fig. 8(a), the maximum electron density corresponding to the cusp decreases by approximately 43%. The Lorentz factor of the electrons near the cusp for the initial electron temperature $T_e = 10$ eV in Fig. 8(b) has almost the same pattern as in the case of zero initial temperature.

The outer pulse magnitude remains almost the same, as shown in Fig. 9(a), and at least the third harmonic of the upshifted base frequency can be seen. This means that the constructive interference condition for the formation of an optically coherent reflected radiation is still satisfied due to a strong localization of electrons in the cusped mirror. We note that an efficient reflection occurs also in regions where a singularity is present in the derivative of the electron density, as in the case of the wake wave breaking in thermal plasma [35,36].

VIII. CONCLUSION

With the help of numerical simulations, we have found a physical realization of the relativistic mirror, the relativistic flying forcibly oscillating mirror. It combines the properties of the relativistic flying mirror [8] and relativistic oscillating mirror [17]. In addition, due to strong periodic modulations of the mirror surface, it acts as a reflective diffraction grating.

The RFFOM appears as a cusped mirror, the low-dimensional region of highest electron density at the joining of the electron cavity wall and the bow wave excited by the intense laser pulse (driver) propagating in plasma. It corresponds to an arrangement of universal and structurally stable density singularities, explained by catastrophe theory. The cusped mirror undergoes forced oscillations imposed by the driver pulse and moves with the group velocity of the driver. It efficiently reflects a counterpropagating relatively weak laser pulse (source). The reflected radiation spectrum exhibits well-pronounced diffractive orders and harmonic orders. These

characteristic features reveal that the cusped mirror is a relativistic flying and oscillating reflective diffraction grating. The base frequency of the reflected radiation and correspondingly all harmonic orders are strongly upshifted with respect to the base frequency of the incident source pulse, due to the double Doppler effect. In the wave number space, the harmonic orders are arranged along ellipsoids with one focus corresponding to the zero wave number.

The described scheme can be used for the generation of bright sources of high-frequency radiation. Its realization is easier than the RFM based on the reflection from the longitudinally breaking wake wave described in Refs. [8–11], where one should maintain a sufficiently slow approach to longitudinal wave breaking. While relativistic self-focusing may cause rapid longitudinal wave breaking destroying the RFM, it helps the discussed RFFOM realization.

Moreover, the described scheme provides an additional tool in laser plasma diagnostics, helping to analyze the dynamics of nonlinear physical processes in relativistic plasmas. The peculiar spectrum of the reflected radiation in the RFFOM scheme, using the head-on collision of the driver and source, substantially extends the capabilities of the scheme for probing relativistic plasma singularities by a transverse source pulse, suggested in Ref. [43]. By probing the cusped mirror by a weak counterpropagating short laser pulse, one can deduce or characterize the parameters of the laser-plasma interaction, including the geometrical properties of the first period of the wake wave (cavity and bow wave), driver pulse frequency and magnitude at the location of the cusped mirror, the velocity of the wake wave, the electron temperature or the electron

momentum distribution at the position of the cusped mirror, etc.

One of the immediate applications of such a diagnostic is control and tuning of burst intensification by singularity emitting radiation (BISER) [27–29,42], which occurs with the same parameters for the driver laser and plasma as required by the RFFOM, so that off-axis radiation from the RFFOM can be observed simultaneously with near- or on-axis BISER. In addition to the fundamental physics concerning intense laser-plasma interactions, plasma diagnostics with the described scheme may help to substantially improve the quality of the laser pulse, our main instrument, by revealing what laser parameters are the most critical. Such investigations, in the example of the laser pulse quality effects on the BISER realization, were conducted recently [44]. That work revealed some critical parameters of the laser pulse which must be improved to obtain good results and scalings predicted by theory.

ACKNOWLEDGMENTS

We appreciate discussions with M. Matys. The work was supported by the project High Field Initiative (Grant No. CZ.02.1.01/0.0/0.0/15_003/0000449) from the European Regional Development Fund, and the project “IT4Innovations National Supercomputing Center LM2015070” from the Ministry of Education, Youth and Sports in Czech Republic. We acknowledge support from JSPS KAKENHI Grants No. JP16K05639 and No. JP19H00669 and Strategic Grant by the QST President: Creative Research No. 20.

-
- [1] F. Krausz and M. Ivanov, *Rev. Mod. Phys.* **81**, 163 (2009).
 - [2] G. A. Mourou, T. Tajima, and S. V. Bulanov, *Rev. Mod. Phys.* **78**, 309 (2006).
 - [3] A. Einstein, *Ann. Phys. (Leipzig)* **322**, 891 (1905).
 - [4] K. Landecker, *Phys. Rev.* **86**, 852 (1952).
 - [5] V. I. Semenova, *Sov. Radiophys. Quantum Electron.* **10**, 599 (1967).
 - [6] R. L. Savage, Jr., C. Joshi, and W. B. Mori, *Phys. Rev. Lett.* **68**, 946 (1992).
 - [7] A. Zhidkov, T. Esirkepov, T. Fujii, K. Nemoto, J. Koga, and S. V. Bulanov, *Phys. Rev. Lett.* **103**, 215003 (2009).
 - [8] S. V. Bulanov, T. Esirkepov, and T. Tajima, *Phys. Rev. Lett.* **91**, 085001 (2003).
 - [9] M. Kando, Y. Fukuda, A. S. Pirozhkov, J. Ma, I. Daito, L. M. Chen, T. Z. Esirkepov, K. Ogura, T. Homma, Y. Hayashi, H. Kotaki, A. Sagisaka, M. Mori, J. K. Koga, H. Daido, S. V. Bulanov, T. Kimura, Y. Kato, and T. Tajima, *Phys. Rev. Lett.* **99**, 135001 (2007).
 - [10] A. S. Pirozhkov, J. Ma, M. Kando, T. Z. Esirkepov, Y. Fukuda, L.-M. Chen, I. Daito, K. Ogura, T. Homma, Y. Hayashi *et al.*, *Phys. Plasmas* **14**, 123106 (2007).
 - [11] M. Kando, A. S. Pirozhkov, K. Kawase, T. Z. Esirkepov, Y. Fukuda, H. Kiriyama, H. Okada, I. Daito, T. Kameshima, Y. Hayashi *et al.*, *Phys. Rev. Lett.* **103**, 235003 (2009).
 - [12] S. V. Bulanov, T. Z. Esirkepov, M. Kando, A. S. Pirozhkov, and N. N. Rosanov, *Phys. Usp.* **56**, 429 (2013).
 - [13] M. Kando, T. Z. Esirkepov, J. K. Koga, A. S. Pirozhkov, and S. V. Bulanov, *Quantum Beam Sci.* **2**, 9 (2018).
 - [14] J. K. Koga, S. V. Bulanov, T. Z. Esirkepov, M. Kando, S. S. Bulanov, and A. S. Pirozhkov, *Plasma Phys. Contr. Fusion* **60**, 074007 (2018).
 - [15] V. V. Kulagin, V. A. Cherepenin, M. S. Hur, and H. Suk, *Phys. Plasmas* **14**, 113101 (2007).
 - [16] S. S. Bulanov, A. Maksimchuk, K. Krushelnick, K. I. Popov, V. Y. Bychenkov, and W. Rozmus, *Phys. Lett. A* **374**, 476 (2010).
 - [17] S. V. Bulanov, N. M. Naumova, and F. Pegoraro, *Phys. Plasmas* **1**, 745 (1994).
 - [18] N. M. Naumova, J. A. Nees, I. V. Sokolov, B. Hou, and G. A. Mourou, *Phys. Rev. Lett.* **92**, 063902 (2004).
 - [19] U. Teubner and P. Gibbon, *Rev. Mod. Phys.* **81**, 445 (2009).
 - [20] T. Z. Esirkepov, S. V. Bulanov, M. Kando, A. S. Pirozhkov, and A. G. Zhidkov, *Phys. Rev. Lett.* **103**, 025002 (2009).
 - [21] T. Tajima and J. M. Dawson, *Phys. Rev. Lett.* **43**, 267 (1979).
 - [22] A. Pukhov and J. Meyer-Ter-Vehn, *Appl. Phys. B* **74**, 355 (2002).
 - [23] E. Esarey, C. B. Schroeder, and W. P. Leemans, *Rev. Mod. Phys.* **81**, 1229 (2009).
 - [24] S. V. Bulanov, F. Pegoraro, A. M. Pukhov, and A. S. Sakharov, *Phys. Rev. Lett.* **78**, 4205 (1997).
 - [25] T. Z. Esirkepov, Y. Kato, and S. V. Bulanov, *Phys. Rev. Lett.* **101**, 265001 (2008).

- [26] T. Poston and I. Stewart, *Catastrophe Theory and Its Applications* (Dover, New York, 1996).
- [27] A. S. Pirozhkov, M. Kando, T. Z. Esirkepov, P. Gallegos, H. Ahmed, E. N. Ragozin, A. Y. Faenov, T. A. Pikuz, T. Kawachi, A. Sagisaka *et al.*, *Phys. Rev. Lett.* **108**, 135004 (2012).
- [28] A. S. Pirozhkov, M. Kando, T. Z. Esirkepov, P. Gallegos, H. Ahmed, E. N. Ragozin, A. Y. Faenov, T. A. Pikuz, T. Kawachi, A. Sagisaka *et al.*, *New J. Phys.* **16**, 093003 (2014).
- [29] A. S. Pirozhkov, T. Z. Esirkepov, T. A. Pikuz, A. Y. Faenov, K. Ogura, Y. Hayashi, H. Kotaki, E. N. Ragozin, D. Neely, H. Kiriyma *et al.*, *Sci. Rep.* **7**, 17968 (2017).
- [30] D. F. Gordon, B. Hafizi, D. Kaganovich, and A. Ting, *Phys. Rev. Lett.* **101**, 045004 (2008).
- [31] T. D. Arber, K. Bennett, C. S. Brady, A. L. Douglas, M. G. Ramsay, N. J. Sirccombe, P. Gillies, R. G. Evans, H. Schmitz, A. R. Bell *et al.*, *Plasma Phys. Contr. Fusion* **57**, 113001 (2015).
- [32] T. Esirkepov, *Comput. Phys. Commun.* **135**, 144 (2001).
- [33] P. Valenta, T. Z. Esirkepov, J. Koga, A. S. Pirozhkov, M. Kando, T. Kawachi, Y.-K. Liu, P. Fang, P. Chen, J. Mu *et al.*, *Phys. Plasmas* **27**, 032109 (2020).
- [34] A. V. Panchenko, T. Z. Esirkepov, A. S. Pirozhkov, M. Kando, F. F. Kamenets, and S. V. Bulanov, *Phys. Rev. E* **78**, 056402 (2008).
- [35] S. V. Bulanov, T. Z. Esirkepov, M. Kando, J. Koga, A. S. Pirozhkov, T. Nakamura, S. S. Bulanov, C. B. Schroeder, E. Esarey, F. Califano *et al.*, *Phys. Plasmas* **19**, 113102 (2012).
- [36] S. V. Bulanov, T. Z. Esirkepov, M. Kando, J. Koga, A. S. Pirozhkov, T. Nakamura, S. S. Bulanov, C. B. Schroeder, E. Esarey, F. Califano *et al.*, *Phys. Plasmas* **19**, 113103 (2012).
- [37] A. A. Solodov, V. M. Malkin, and N. J. Fisch, *Phys. Plasmas* **13**, 093102 (2006).
- [38] J. Mu, F. Y. Li, M. Zeng, M. Chen, Z. M. Sheng, and J. Zhang, *Appl. Phys. Lett.* **103**, 261114 (2013).
- [39] C. Zhang, C. K. Huang, K. A. Marsh, C. E. Clayton, W. B. Mori, and C. Joshi, *Sci. Adv.* **5**, eaax4545 (2019).
- [40] N. H. Matlis, S. Reed, S. S. Bulanov, V. Chvykov, G. Kalintchenko, T. Matsuoka, P. Rousseau, V. Yanovsky, A. Maksimchuk, S. Kalmykov *et al.*, *Nat. Phys.* **2**, 749 (2006).
- [41] A. Savert, S. P. D. Mangles, M. Schnell, E. Siminos, J. M. Cole, M. Leier, M. Reuter, M. B. Schwab, M. Möller, K. Poder, O. Jackel, G. G. Paulus, C. Spielmann, S. Skupin, Z. Najmudin, and M. C. Kaluza, *Phys. Rev. Lett.* **115**, 055002 (2015).
- [42] A. Sagisaka, K. Ogura, T. Z. Esirkepov, D. Neely, T. A. Pikuz *et al.*, *High Energy Density Phys.* **36**, 100751 (2020).
- [43] T. Z. Esirkepov, J. Mu, Y. Gu, T. M. Jeong, P. Valenta, O. Klimo, J. K. Koga, M. Kando, D. Neely, G. Korn, S. V. Bulanov, and A. S. Pirozhkov, *Phys. Plasmas* **27**, 052103 (2020).
- [44] A. S. Pirozhkov, T. Z. Esirkepov, T. A. Pikuz, A. Y. Faenov, A. Sagisaka *et al.*, *Quantum Beam Sci.* **2**, 7 (2018).